



Suivi topo-morphologique du Sillon de Talbert pour l'année 2024

Pierre Stéphan, Serge Suanez, Jérôme Ammann, Isabel Tardieu, Julien Houron

► To cite this version:

Pierre Stéphan, Serge Suanez, Jérôme Ammann, Isabel Tardieu, Julien Houron. Suivi topo-morphologique du Sillon de Talbert pour l'année 2024. CNRS; Université de Bretagne Occidentale (UBO). 2025, pp.75. hal-04948050

HAL Id: hal-04948050

<https://hal.science/hal-04948050v1>

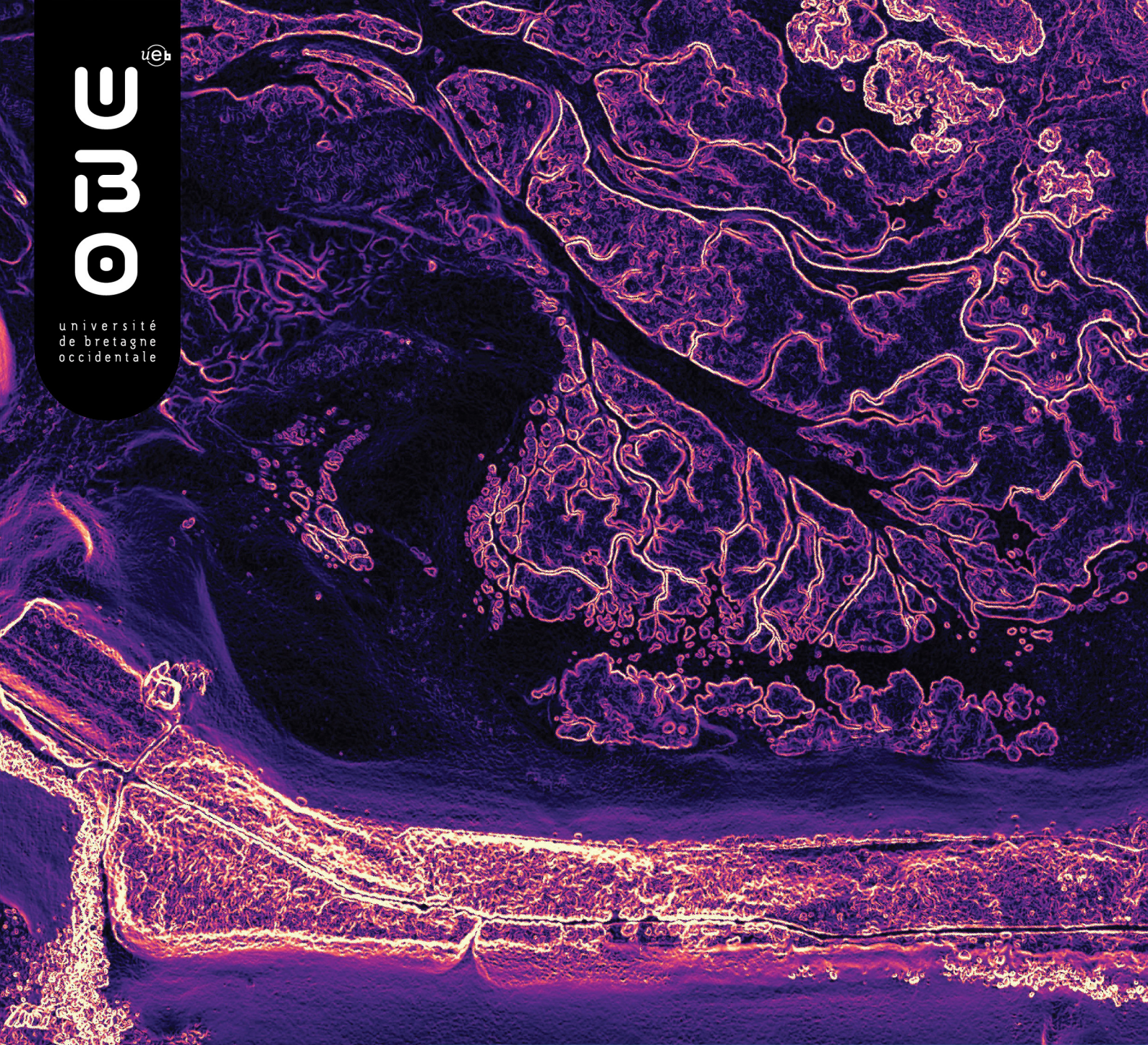
Submitted on 14 Feb 2025

HAL is a multi-disciplinary open access archive for the deposit and dissemination of scientific research documents, whether they are published or not. The documents may come from teaching and research institutions in France or abroad, or from public or private research centers.

L'archive ouverte pluridisciplinaire **HAL**, est destinée au dépôt et à la diffusion de documents scientifiques de niveau recherche, publiés ou non, émanant des établissements d'enseignement et de recherche français ou étrangers, des laboratoires publics ou privés.



Distributed under a Creative Commons Attribution 4.0 International License



Pierre STÉPHAN
Serge SUANEZ
Jérôme AMMANN
Isabel TARDIEU
Julien HOURON

Suivi topo-morphologique du Sillon de Talbert pour l'année 2024

Février 2025





Suivi topo-morphologique du Sillon de Talbert pour l'année 2024

Février 2025



Littoral
Environnement
Télédétection
Géomatique
UMR 6554 CNRS

Pierre STÉPHAN
Serge SUANEZ
Jérôme AMMANN
Isabel TARDIEU
Julien HOURON

Maître d'œuvre

Laboratoire LETG (UMR 6554 CNRS),
Institut Universitaire Européen de la Mer,
Place Nicolas Copernic, 29280 Plouzané

Direction scientifique

Pierre Stéphan (pierre.stephan@univ-brest.fr)
Serge Suanez (serge.suanez@univ-brest.fr)



1-Introduction

La présente étude s'inscrit dans la continuité du suivi topo-morphologique du Sillon de Talbert initié en 2003 à la demande de la commune de Pleubian et du Conservatoire du Littoral (voir section 6 – références bibliographiques). L'objectif est d'analyser les modalités d'évolution de la flèche de galets, classée en Réserve Naturelle Régionale depuis 2006. Dans le cadre de ce rapport, nous présentons les principaux changements morphologiques survenus entre les levés topographiques effectués aux mois de septembre 2023 et de septembre 2024 à l'échelle du Sillon dans un premier temps, puis dans le secteur de la brèche dans un second temps. Enfin, nous présenterons les résultats obtenus sur la période à partir des levés réalisés par Julien Houron le long des profils transversaux au cordon.

A l'échelle du Sillon, la méthode que nous avons employée pour reconstituer la topographie de l'estran reste inchangée par rapport à l'année précédente. Elle s'appuie sur un traitement photogrammétrique d'images aériennes acquises au drone. Ces vues aériennes ont été réalisées le 18 septembre 2024 à partir d'un drone Mavik 3 Pro survolant le Sillon à une altitude moyenne de 110 m. Un total de 2171 images a été obtenu durant les survols, couvrant une superficie de 1,76 km². A partir de ces prises de vue, la topographie a été reconstituée selon le principe de la stéréo-photogrammétrie sous le logiciel Agisoft Metashape. Le procédé employé suppose que les prises de vue se recoupent entre elles. Lors de nos survols, un taux de recouvrement de 80% entre les images a été prédéfini. La différence d'inclinaison des différents clichés a été utilisée par le logiciel pour générer un nuage de points topographiques de très forte densité.

Avant les survols, 42 cibles ont été positionnées au sol et leur position a été relevée au DGPS. Les mesures au DGPS ont été réalisées à partir d'une station fixe installée sur un repère d'arpentage implanté au sommet du rocher de Roc'h Gwen. Ce repère a été géoréférencé à partir d'une borne IGN située sur le sémaphore de Crac'h Maout, dont les coordonnées géodésiques sont accessibles sur le site de l'IGN ([www.ign.fr/rubrique Géodésie](http://www.ign.fr/rubrique_Géodésie)). L'altitude de cette borne a été revue à partir d'un procédé de post-traitement des données GPS et se situe à 42,81 m NGF. Ainsi, l'ensemble des cibles a été positionnée dans le système de référence Lambert 93 (EPSG:2154) et raccordé au niveau altitudinal NGF.

Les coordonnées de ces cibles ont été utilisées pour géoréférencer les prises de vue et les nuages de points topographiques produits. Cette méthode a permis de produire trois principaux jeux de données : (i) une orthophotographie de la zone survolée ; (ii) un nuage de points de très forte densité comptant plus de 510 millions de points (soit 309 points/m²) ; (iii) un Modèle Numérique de Terrain d'une résolution de 10x10 cm (fig. 1). Les calculs ont été réalisés sur le supercalculateur de la TGIR HUMANUM du CNRS.

Il faut noter qu'en dépit de leur très haute résolution, les MNT reconstruits à partir des survols au drone peuvent parfois présenter des erreurs significatives en raison d'un mauvais recouplement des photographies aériennes et/ou d'une mauvaise qualité des images. Pour limiter ces erreurs, une procédure de vérification de la qualité des images a été réalisée sous le logiciel Agisoft Metashape et un filtrage des points servant à reconstruire la topographie a permis d'éliminer le maximum de bruit. En définitive, les erreurs de positionnement sont estimées à 1,6 cm en X et Y, et à 3 cm en Z. Cette incertitude est très faible puisqu'elle correspond à la taille du pixel en X-Y et à l'erreur de la mesure au DGPS en Z. Notons enfin que le couvert végétal et les laisses de mer peuvent aussi poser problème localement. En effet, cette méthode considère la végétation et le goémon comme une surface

topographique (on parle alors de « sursol »), tandis que la topographie du sol n'est pas reconstruite. Dans notre cas, cela concerne les zones végétalisées de la racine et de la partie proximale du Sillon dont l'élévation a pu être surestimée, en particulier là où se développent de belles touffes d'oyat. Par chance, les laisses de mer présentes sur la plage lors de nos survols étaient peu volumineuses et ne sont pas en mesure de bâiller nos estimations de bilans sédimentaires.

Une partie de ce rapport porte également sur le suivi topo-morphologique de la brèche ouverte en mars 2018 dans la partie proximale du Sillon, à l'emplacement de l'ancienne zone appelée « taille de guêpe ». Depuis le mois de mars 2018, ce secteur fait l'objet de relevés à une fréquence plus importante (environ un levé topographique tous les 2-3 mois) afin de suivre au plus près les changements. Là encore, la méthode utilisée pour réaliser ces relevés s'appuie sur des survols au drone et l'acquisition d'images aériennes dont le traitement photogrammétrique est réalisé à l'aide du logiciel Agisoft Metashape. Le détail des différentes missions réalisées entre septembre 2023 et septembre 2024 est donné dans le tableau 1. L'annexe 1 présente les rapports issus des traitements photogrammétriques réalisés.

| Date | Technologie | materiel utilisé | Précision horizontale | Précision verticale | Superficie couverte (km ²) | Nombre de points topographiques acquis sur le terrain | Nombre de points topographiques utilisés pour générer le MNT | Résolution du MNT (m) |
|------------|-------------|------------------|-----------------------|---------------------|--|---|--|-----------------------|
| 28/09/2023 | drone | Mavik 3 Pro | +/- 0.0226 | +/- 0.0109 | 1.69 | > 10 ⁸ | > 10 ⁸ | 0.1 |
| 18/12/2023 | drone | Mavik 3 Pro | +/- 0.0079 | +/- 0.0214 | 0.274 | > 10 ⁸ | > 10 ⁸ | 0.034 |
| 20/02/2024 | drone | Mavik 3 Pro | +/- 0.0094 | +/- 0.0139 | 0.293 | > 10 ⁸ | > 10 ⁸ | 0.033 |
| 18/09/2024 | drone | Mavik 3 Pro | +/- 0.0158 | +/- 0.0304 | 1.76 | > 10 ⁸ | > 10 ⁸ | 0,1 |

Tableau 1 : Inventaire des campagnes de mesures topo-morphologiques réalisées dans le secteur de la brèche entre septembre 2023 et septembre 2024.

Enfin, le travail mené depuis 2012 sur les dynamiques hydro-morphologiques a été poursuivis sur la période. Les conditions météo-marines ont été analysées à partir de mesures de pressions réalisées à l'aide du capteur OSSI installé sur l'estran. En parallèle, les suivis topographiques ont été réalisés par Julien Houron durant l'année le long des différents profils. Ces données prolongent le suivi des conditions de vagues au plus près du Sillon.

L'année 2024 a également été consacrée à la valorisation des résultats obtenus dans le cadre de l'étude d'incidence de la brèche. Un article scientifique a été publié dans la revue internationale *Geomorphology*. Cet article est livré en Annexe 2 du présent rapport.

2 - Evolutions morphologiques du Sillon dans son ensemble, entre septembre 2023 et septembre 2024

2.1. Vue d'ensemble

Les changements morphologiques mesurés sur le Sillon de Talbert entre septembre 2023 et septembre 2024 sont de faible ampleur et reflètent des conditions météo-marines peu morphogènes sur l'ensemble de la période. Ce constat est assez similaire à celui que nous avions dressé dans nos deux précédents rapports (Stéphan *et al.*, 2023, 2024) portant sur la période allant de septembre 2021 à

septembre 2023. Aucune tempête significative ou épisode de fortes vagues n'a été enregistré durant cette période. Le Sillon n'a pas connu de larges franchissements susceptibles de le faire reculer. Par conséquent, les valeurs de recul sont très faibles (fig. 8) et reflètent soit des franchissements de tempête très localisés (zones n°3 et 4, fig. 8), soit un remodelage du revers par les vagues de nord-est (zone n°2, fig. 8). La période a donc été dominée par les transits longitudinaux dirigés vers le NE sur la face exposée du Sillon et vers le SW sur le revers. La période a également été dominée par une remontée des sédiments vers la crête et l'engrassement de bermes en haut de plage. Dans la partie médiane du sillon, la crête s'est exhaussée de 22 cm en moyenne (entre les profils P065 et P100, figs. 4 et 6), avec une valeur maximale de +43 cm au niveau du profil P070. Cela suggère un ou plusieurs événements constructifs associant de fortes vagues à une marée de vive-eau moyenne. Comme en 2022 et 2023, le secteur qui a enregistré le plus d'érosion est la plage de la partie proximale (fig. 3). A l'inverse, le secteur qui a bénéficié le plus d'apports sédimentaires est la crête et le revers de la spatule.

2.2. Vue de détails

Les principales modifications morphologiques sont synthétisées dans la figure 3 et sont décrites comme suit :

(1, fig. 3) : un léger excès sédimentaire sur la plage du Chouck

La plage du Chouck a enregistré de faibles évolutions morphologiques sur la période. Toutefois, elle présente un bilan sédimentaire excédentaire d'environ +400 m³ entre septembre 2023 et septembre 2024. Les volumes érodés représentent -230 m³ et correspondent à un léger creusement de la partie basse de la plage, tandis que les volumes déposés sont de +660 m³ et ont bénéficié à la partie haute de la plage et au pied de dune. Notons que la partie sud de la plage du Chouck n'a pas pu être survolée le 18/09/2024. Ce bilan volumique est donc partiel.

(2, fig. 3) : une érosion limitée de la brèche

Dans son ensemble, le secteur environnant la brèche a connu une érosion limitée sur la période. Aucun élargissement significatif de la brèche n'a été mesuré (figures 9 à 12). La rive ouest a perdu -340 m³ de sédiment environ, tandis que la rive orientale a bénéficié d'un apport de +880 m³. Cet apport s'est accompagné d'un déplacement de la rive vers le sud et d'un recul limité du revers inférieur à 2 m (n°1, fig. 8). Le fond de la brèche ne s'est pas incisé davantage. L'altitude la plus basse relevée dans le fond de la brèche est de 7,2 m Cote Marine. Cette cote n'a quasiment pas changé depuis septembre 2022 et traduit une situation d'équilibre. Dans le marais de Mer Melen, les sédiments qui forment le delta de flot ont été remaniés et étalés davantage vers le sud. Près de 1000 m³ de sable ont été transportés jusqu'au chenal de marée principal qui draine le marais. Ces volumes ont probablement été exportés vers l'aval. Enfin, plaquée contre l'enrochement, la petite plage du Chouck n'a pas connu de changements importants.

(3, fig. 3) : l'érosion de la plage dans la partie proximale

Dans la partie proximale, la plage de la face exposée du Sillon montre un bilan sédimentaire déficitaire de -8750 m³ au total. Une partie de ce matériel a été déplacé vers la brèche et a permis l'engrassement de la rive orientale de la brèche. Une autre partie a été transportée au sommet du cordon sous l'effet du vent où les buttes d'oyat ont piégé près de 920 m³ de sable. Une autre partie a été transférée sur le revers lors d'un ou de plusieurs épisodes de franchissement. Dans ce secteur, les dunes embryonnaires sont individualisées par une série de dépressions inter-dunaires parallèles entre elles qui canalisent les

flux d'eau et de sédiment lors des franchissements. Ce transfert sédimentaire se traduit par la formation de petits lobes d'overwash à leur débouché sur le revers.

(4, fig. 3) le redressement du profil par overtopping dans les parties médiane et distale

Durant la période, les conditions météo-marines relativement clémentes ont favorisé l'exhaussement de la crête du Sillon, l'action des vagues ayant été portée à un niveau suffisamment haut lors de grands coefficients de marée. Plusieurs épisodes météo-marins ont été constructifs pour le Sillon, permettant un exhaussement de la crête de 20 à 50 cm par endroits (figs. 4 et 6). D'une façon générale, c'est toute la crête des partie médiane et distale qui a bénéficié d'apports sédimentaires estimés à +7.000 m³. Cet engrassement du sommet s'est effectué au dépend de la plage dont le profil s'est creusé et où les bermes de haut de cordon ont migré vers le haut.

(5, fig. 3) transit par la dérive sédimentaire

D'après les bilans présentés plus haut, on peut estimer qu'environ 2500 m³ de sédiments ont été déplacés le long de la plage vers la pointe. Ce transit est légèrement inférieur au volume moyen mis en mouvement le long du Sillon depuis 2002.

(6, fig. 3) : lobe de jusant et pointe du Sillon

Sur le lobe de jusant, les changements morphologiques sont caractéristiques d'une période de calme morphogénique. Les déplacements sédimentaires ont été principalement contrôlés par les courants de marée. Les courants de jusant ont repoussé près de 1500 m³ de sédiment vers le nord-ouest. A la pointe du Sillon, environ 3500 m³ de galets ont été déplacés sur le revers de la spatule.

(7, fig. 3) : le revers de la spatule

Le revers de la spatule est le secteur où s'accumulent tous les sédiments que la dérive de plage a mis en mouvement sur la face exposée du Sillon. Sur la période, ce secteur a bénéficié d'un apport d'environ +2500 m³ de sédiments. Une partie de ce matériel a permis un exhaussement de la crête de quelques décimètres.

(8, fig. 3) : transits sédimentaires sur le revers de la partie médiane

Sur le revers de la partie médiane, c'est environ 1000 m³ de galets qui ont été mis en mouvement le long du revers et déplacés vers le sud-ouest. Ce transit sédimentaire, dont le sens est inverse par rapport à celui observé sur la face exposée sur Sillon, s'opère par le biais de rides. Il se traduit par l'accentuation des sinuosités où se juxtaposent des secteurs en érosion et des secteurs en accrétion. A nouveau, ce type d'évolution morphologique est caractéristique d'une période faible activité morphogène que l'on mesure depuis septembre 2021.

(9 et 10, fig. 3) : transferts sur le revers par débordement (overwash)

Enfin, sur le revers de la partie proximale, le Sillon a été franchi par les vagues de tempêtes là où la crête est la plus basse. Un recul de 4 m en moyenne a été mesuré le long du revers entre les profils P030 et P032 (n°3, fig. 8). Entre les points de mesure P052 et P057, le recul atteint 2 m. Les volumes totaux déversés sur le revers à ces deux endroits sont estimés à +2.700 m³.

3- Bilan du suivi de la brèche : évolutions topo-morphologiques entre septembre 2017 et septembre 2024

Les figures 9 à 12 présentent les résultats du suivi mis en place à l'issue de l'ouverture de la brèche dans la partie proximale du Sillon de Talbert. Les résultats sont les suivants :

| Périodes | Commentaires |
|-------------------------------------|---|
| Septembre 2017 – 7 mars 2018 | Entre les mois de septembre 2017 et mars 2018, les relevés montrent tout d'abord l'impact de la tempête Eleanor des 2-3 janvier 2018 qui entraîne une érosion importante de la face exposée du cordon et un dépôt de sédiment sur le revers (dynamique de <i>rollover</i>). Le second événement qui marque cette période est l'ouverture de la brèche (deux jours avant le relevé du mois de mars 2018) qui s'élargit très rapidement. L'érosion provoquée par les courants de marée empruntant la brèche conduit à la formation d'un delta de jusant en bas de plage. |
| 7 mars 2018 – 22 mars 2018 | Durant cette courte période de temps (15 jours), les évolutions morphologiques sont peu marquées. Le delta de jusant est repris par les vagues et déplacé vers l'est. Ce stock tend à remonter vers le sommet du cordon. |
| 22 mars 2018 – 17 avril 2018 | Cette période (28 jours) est marquée par une marée de vive-eau (coefficients supérieurs à 100 du 31 mars au 02 avril 2018) qui génère de forts courants de flot et de jusant dans la brèche. Les courants de jusant semblent prédominer. La présence de l'enrochement résiduel oblige les courants de jusant à s'orienter vers l'ouest au débouché de la brèche sur la plage. Leur vitesse est donc renforcée sur la rive concave (rive ouest) de la brèche et entraîne une érosion de la dune basse dans ce secteur. Le front de dune est taillé en micro-falaise et recule de 6 m par endroits. L'ancien lobe de jusant qui s'était constitué en mars 2018 poursuit sa remontée vers le haut de la plage et vers la dune sommitale. |
| 17 avril 2018 – 17 juillet 2018 | Cette période (91 jours) est à nouveau marquée par plusieurs marées de vive-eau en (fin avril, mi-mai, mi-juin 2018). La rive ouest de la brèche subit une érosion importante. Le front de dune recul de 3,5 m. Un nouveau lobe de jusant s'édifie à l'extrémité de l'enrochement résiduel, sur le bas de la plage. |
| 17 juillet 2018 – 13 septembre 2018 | Cette période (58 jours) reste dominée par les dynamiques érosives liées aux courants de jusant qui érodent la rive occidentale de la brèche (recul du front de dune de 8,5 m) et entraîne l'accumulation de sable à l'exutoire de la brèche, sur le bas de plage. Deux marées de vive-eau (mi-août et début septembre) sont responsables de ces changements. A l'est de la brèche, le haut de plage poursuit son engrangissement. |
| 13 septembre 2018 | Durant cette période, l'érosion de la rive ouest de la brèche se |

| | |
|--|---|
| – 21 novembre 2018 | poursuit (recul de 3 m du front de dune). Le delta de jusant est également érodé. Le matériel est redistribué sur le bas de plage, vers l'est. Les données sont quelque peu biaisées par la présence de grandes quantités d'algues de rive échouées sur la plage. Sur le revers, des changements morphologiques sont également observés sous l'effet d'une reprise du transit longitudinal causé par le renforcement des houles à l'approche de la période hivernale. |
| 21 novembre 2018 – 05 février 2019 | La comparaison du relevé du 05 février 2019 avec les levés précédents est à nouveau partiellement biaisée par les accumulations d'algues d'échouage sur la face exposée du cordon. On note néanmoins une érosion modérée de la plage, le déplacement du delta de jusant vers le nord-est par la dérive littorale, une érosion de la rive occidentale de la brèche (avec un recul du front de dune de 3,8 m). Enfin, on observe pour la première fois l'accumulation de sédiments dans la partie interne de la brèche et l'amorce de formation d'un delta de flot. |
| 05 février 2019 – 08 mars 2019 | Durant cette période hivernale (31 jours), le chenal de marée qui emprunte désormais la brèche est remanié par les courants de flot et de jusant qui déplace les bancs de sables sur le fond. La rive ouest de la brèche recule de 2,8 m. Sur le sillon, on assiste à un engrangement de la face exposée du cordon. A l'emplacement précédent du delta de jusant, le bas de plage enregistre une érosion liée à un déplacement du stock sédimentaire vers le nord-est. |
| 08 mars 2019 – 21 mai 2019 | Les deux rives de la brèche sont érodées. Le matériel s'accumule en partie sur le delta de flot, et en partie sur le delta de jusant. Sur le Sillon, la partie basse de la plage subit également une érosion. |
| 21 mai 2019 – 18 septembre 2019 | Durant cette période (120 jours), les principaux changements morphologiques sont observés au niveau de la brèche. Les bancs tidaux sont déplacés vers les parties internes (delta de flot) et externe (delta de jusant) de la brèche. |
| 18 septembre 2019 – 17 décembre 2019 | Cette période (90 jours) est caractérisée par plusieurs épisodes tempétueux marqués par de fortes houles. Les changements morphologiques sont importants : une très forte érosion de la rive occidentale de la brèche (recul du front de dune de 4,5 m), une accumulation de matériel sur la rive orientale |
| 17 décembre 2019 – 23 janvier 2020 | Durant cette courte période (37 jours), les conditions météo-marines sont restées relativement clémentes et les changements morphologiques ont été de faible ampleur. On note une érosion modérée de la rive occidentale de la brèche. Taillée en micro-falaise, la dune enregistre un recul vers l'ouest de 1 m en moyenne. A l'inverse, la rive orientale connaît un apport de sédiments, provoquant une légère migration latérale du chenal de marée dans le fond de la brèche. |

| | |
|--------------------------------------|--|
| 23 janvier 2020 – 26 mai 2020 | Cette période est marquée par les tempêtes <i>Ciara</i> et <i>Inès</i> , entre le 09 et le 13 février 2020. Ces deux épisodes correspondent aux événements les plus morphogènes enregistrés depuis le début de ce suivi. Sur la rive orientale, les vagues de tempête font reculer d'environ 5 m la micro-falaise d'érosion. Sur la rive occidentale, l'ensemble du sillon recule vers le sud sur une distance de 10 à 15 m (fig. 12). Dans les bilans sédimentaires, ce recul par <i>rollover</i> se traduit par un transfert des sédiments depuis le haut de la plage exposée vers le revers. Le fond de la brèche s'élargit également, principalement au dépend de la rive occidentale. Le matériel est en grande partie exporté en direction du marais de Mer Melen où se forme un vaste lobe de flot. |
| 26 mai 2020 – 07 septembre 2020 | Cette période est peu morphogène. Les évolutions morphologiques traduisent une tendance à la reconstruction du sillon. Le haut de plage s'engraisse, ainsi que la rive orientale. |
| 07 septembre 2020 – 17 novembre 2020 | Là encore, sous des conditions morphogène (même limitées), liées à l'épisode de la Toussaint 2020, la rive orientale a bénéficié d'apports sédimentaires, tandis que le franchissement du cordon par les vagues de tempête a entraîné une érosion de la plage et un transfert du matériel sur le revers. Sur la rive occidentale de la brèche, la dune a reculé de 2 m environ. |
| 17 novembre 2020 – 26 mai 2021 | Durant cette période, la rive occidentale de la brèche a été érodée par les courants de marée, mais le front de dune n'a pas reculé. Sur la rive orientale de la brèche, on note que la plage s'est légèrement engrassée et que la pente du revers s'est rééquilibrée (érosion en haut de pente, accrétion en bas de pente). |
| 26 mai 2021 – 22 septembre 2021 | Cette période estivale est marquée par des changements morphologiques de très faible ampleur, en l'absence d'épisodes morphogènes et de marée de vive-eau. |
| 22 septembre 2021 – 15 décembre 2021 | Seule la queue du Sillon a enregistré des changements morphologiques significatifs qui se sont traduits par une érosion de la plage et un dépôt de matériel sédimentaire sur la rive orientale de la brèche. |
| 15 décembre 2021 – 04 mai 2022 | Durant cette période hivernale, la rive orientale de la brèche a été érodée dans sa partie basse et le matériel a été transféré à son débouché sur l'estran pour former un lobe de jusant. |
| 04 mai 2022 – 15 septembre 2022 | Au cours du printemps et de l'été 2022, les changements morphologiques ont été de faible ampleur. Le flanc est de la brèche s'est érodé de façon générale. A l'ouest de la brèche, le sillon a été érodé dans sa partie haute, probablement sous l'effet des courants de jusant, lors des forts coefficients de |

| | |
|--------------------------------------|---|
| | marée d'équinoxe. |
| 15 septembre 2022 – 02 mars 2023 | Durant l'automne 2022 et l'hiver 2023, la rive ouest de la brèche a subi une érosion et le replat dunaire a reculé de plusieurs mètres. Toutefois, ce recul a été contrebalancé par un engrangissement important de la rive orientale. Cela explique que la largeur de la brèche s'est réduite, passant de 52 à 43 m (fig. 11). |
| 02 mars 2023 – 05 mai 2023 | Durant cette période marquée par de forts coefficients de marée, la rive ouest a reculé de façon importante par érosion du replat dunaire. La rive opposée a également été érodée. Les vagues ont franchi le sommet du Sillon comme le montrent les petits lobes d'overwash déposés sur le revers au débouché de petits couloirs situées entre les dunes embryonnaires. |
| 05 mai 2023 – 28 septembre 2023 | Les évolutions morphologiques ont été peu significatives durant cette période marquée par de faibles coefficients de marée et des conditions météo-marines peu énergétiques. |
| 28 septembre 2023 – 18 décembre 2023 | Les changements morphologiques sont relativement importants de part et d'autre de la brèche. Sur la rive occidentale, le talus dunaire a reculé de 2,5 m en moyenne. A l'inverse, la rive orientale s'est engrangée. Cela signe l'action de vagues assez morphogènes. En effet, cette période a été marquée par une série de tempêtes. Toutefois, celles-ci sont survenues par faibles coefficients de marée. C'est le cas de la tempête <i>Ciaran</i> du 2 novembre 2023 qui n'a pas conduit au franchissement massif du Sillon par les vagues, malgré la forte du vent et une hauteur significative de la houle au large comprise entre 10 et 11 m. |
| 18 décembre 2023 – 20 février 2024 | Les changements morphologiques sont faibles. On note la formation d'une accumulation de sable dans le prolongement de l'enrochement (lobe de jusant) et une faible érosion de la rive est de la brèche. Cette période est caractérisée par quelques franchissements sur la section mobile du Sillon comme l'atteste le dépôt de sédiments sur le revers sous la forme de lobe d'overwash. Ces lobes se situent systématiquement au débouché des dépressions inter-dunaires qui ont canalisé les paquets de vagues. Ils sont probablement mis en place lors de la tempête <i>Karlotta</i> du 10-11 février 2024 (voir section 4 de ce rapport). |
| 20 février 2024 – 18 septembre 2024 | Les évolutions morphologiques sont peu significatives durant cette période. Les changements morphologiques les plus importants sont observés sur la partie mobile du Sillon où le haut de plage a connu un engrangissement à la faveur des houles constructives du printemps et de l'automne. Sur la rive ouest de la brèche, le talus dunaire s'est érodé modérément. |

Entre septembre 2023 et septembre 2024, le secteur de la brèche a connu une relative stabilité morphologique. La brèche ne s'est pas élargie et ne s'est pas approfondie. La figure 11 montre que la

morphologie générale de la bète (largeur, profondeur) est relativement stable depuis 2021 et traduit une situation d'équilibre avec les forçages hydrodynamiques. On note que les variations de largeur présentent un comportement saisonnier. En hiver, la brèche tend à se rétrécir. Les vagues sont plus fortes et transportent de plus grandes quantités de sédiments depuis la plage vers la rive orientale de la brèche où ils s'accumulent. En été, en revanche, l'action des courants de jusant prédomine sur celle des vagues et la rive occidentale est érodée, ce qui conduit à l'élargissement de la brèche.

4- Bilan du suivi topo-morphologique à haute fréquence de profils de plage du sillon de Talbert pour l'année 2024

Depuis le mois de septembre 2012, un suivi morphologique à haute fréquence a été mis en place en parallèle du suivi topo-morphologique annuel de l'ensemble du sillon (effectué quant à lui depuis 2006). Ce suivi repose sur (i) des levés topographiques mensuels réalisés le long de trois radiales localisées dans les parties les plus mobiles du sillon (le secteur de la brèche, et les sections proximale et médiane de la flèche), (ii) des mesures des conditions hydrodynamiques (houle et niveau d'eau) à partir d'un capteur de pression installé dans la zone intertidale au droit du profil B (fig. A).



Figure A. Localisation des trois profils de mesures topo-morphologiques et du capteur OSSI de pression de houle et de niveaux d'eau. Ce dernier est installé dans la zone intertidale à -0,461 m NGF. Le fond de carte correspond à l'orthophotographie IGN de 2012, la brèche ouverte au mois de mars 2018 n'est pas présente).

L'objectif de ce suivi à haute fréquence est de mesurer et de quantifier l'impact de tous les épisodes tempétueux agissant à une échelle épisodique et/ou d'évaluer les processus de régénération (en période de temps calme) agissant là encore à des échelles courtes (mensuelle à épisodique). Ainsi, durant l'année 2024, une campagne mensuelle de mesures de profils de plage a été réalisée (fig. B).

Suivi morphologique du Sillon de Talbert – Pleubian – Période 2023-2024

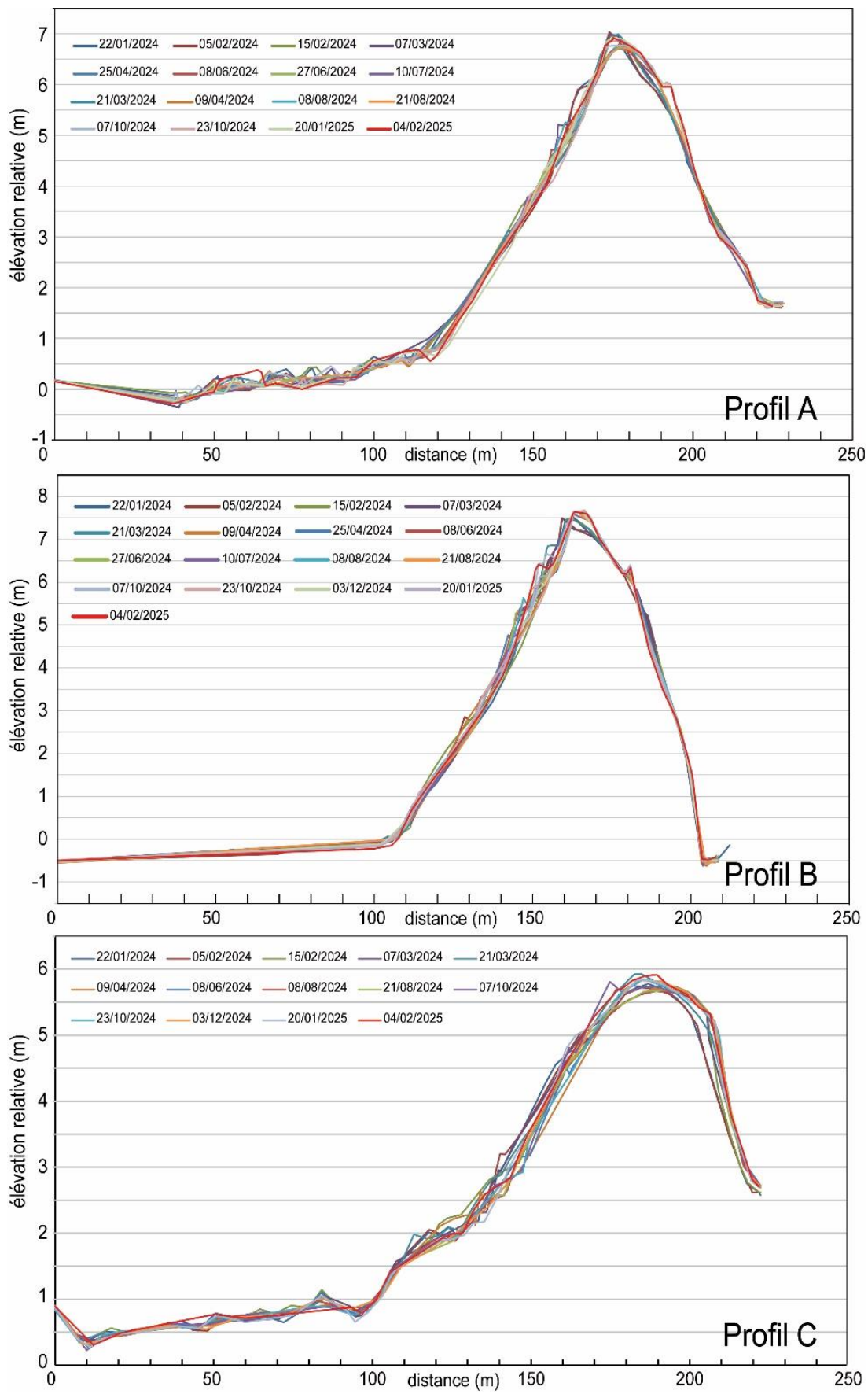


Figure B. Enveloppe de profils topo-morphologiques des profils A, B, et C entre les mois de janvier 2024 et février 2025.

L'analyse de ces données morphologiques sur l'ensemble de l'année 2024, et pour les 3 profils, montre une grande stabilité. Aucun changement majeur n'est observé quelle que soit la section de la flèche. Quelques migrations de gradins sont observées sur la plage avant des profils A et B. Ces changements morphologiques restent toutefois classiques du fonctionnement morphosédimentaire des cordons de galets. Pour le profil C, on observe un petit transfert de sédiment de l'avant vers l'arrière du profil, lié à la migration de cette section de la flèche située dans le secteur de la brèche. Ces dynamiques reflètent les changements morphosédimentaires mesurés par le suivi de la brèche au drone (figs. 9 à 12).

Lors de la tempête Karlotta du 10-11 février 2024, la hauteur de la houle au large Hs était d'environ 5 m pour un coefficient 107 lors de pleine mer de 8h du matin (fig C). Le décalage entre la PM et les plus fortes houles explique l'absence de submersion et de changement morphologique enregistré durant cet épisode tempétueux.

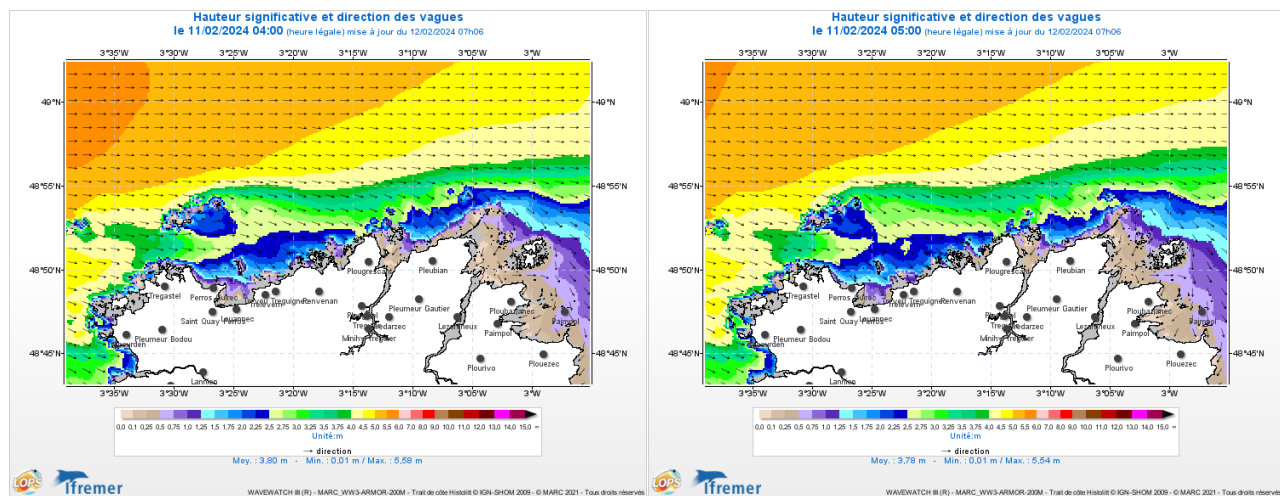


Figure C. Simulations numériques des conditions de houle pour la matinée du 11 février 2024 (tempête Karlotta), entre 4h et 5h du matin à partir du modèle WW3 développé par le LOPS-Ifremer (base de données MARC : Modélisation et Analyse pour la Recherche Côtière).

Lors de la tempête Pierrick du 9 avril 2024, les hauteurs de la houle au large ont atteint 7 m entre 0h et 1h du matin, alors que le coefficient de marée était de 112 lors de la pleine mer du matin à 8h (fig D). Durant la PM du soir (20h), les hauteurs de la houle avaient considérablement baissé (entre 3 et 3,5 m).

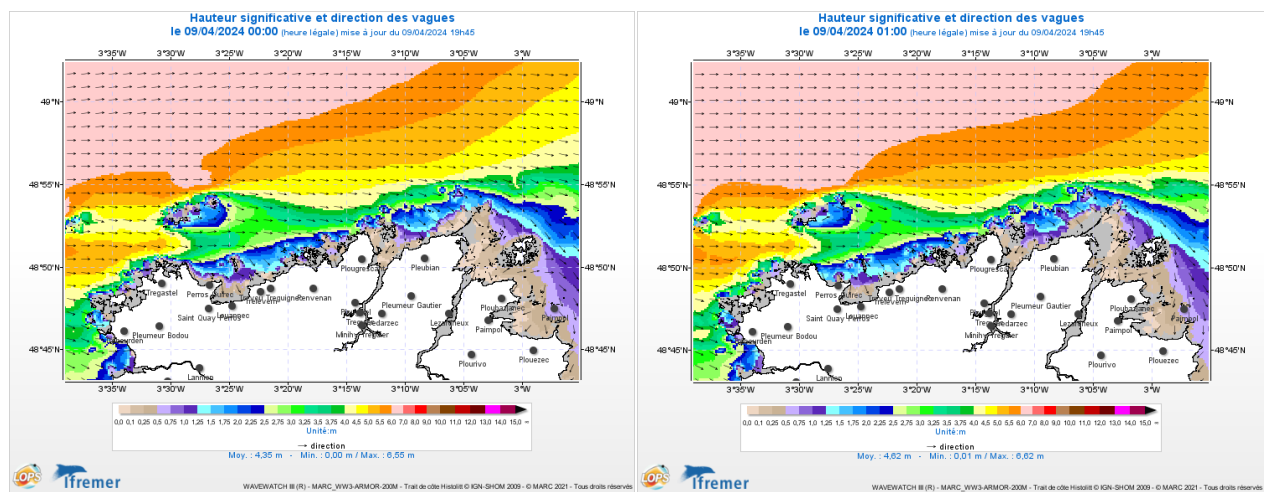


Figure D. Simulations numériques des conditions de houle pour la matinée du 9 avril 2024 (tempête Pierrick), entre 0h et 1h du matin à partir du modèle WW3 développé par le LOPS-Ifremer (base de données MARC : Modélisation et Analyse pour la Recherche Côtière).

En conclusion, les deux tempêtes majeures combinées à des fortes marées survenues en 2024 n'ont généré aucun changement morphologique significatif car la hauteur des houles n'était pas suffisamment importante. La faible énergie de la houle, malgré des coefficients de marée élevés (> 100 à 110) n'a pas été morphogène. A cela s'ajoute le fait que les hauteurs les plus importantes de la houle n'ont pas été atteintes lors des pleines mers. Ainsi, le suivi topo-morphologique à haute fréquence le long des trois profils de plage pour l'année 2024 n'a montré aucun changement morphologique majeur.

5- Références bibliographiques

5.1. Rapports d'étude

Fichaut B., Suanez S., Stéphan P. (2010). *Rapport sur le suivi morphosédimentaire du Sillon de Talbert pour l'année 2010*. Rapport d'étude, Laboratoire LETG-Brest Géomer (UMR 6554 CNRS), Université de Bretagne Occidentale, Institut Universitaire Européen de la Mer, décembre 2010, 16 p.

Fichaut, B., Stéphan P., Suanez, S., Blaise E. (2013). *Suivi topo-morphologique du Sillon de Talbert (Commune de Pleubian - Période 2012-2013)*. Rapport d'étude, Laboratoire LETG-Brest Géomer (UMR 6554 CNRS), Université de Bretagne Occidentale, Institut Universitaire Européen de la Mer, 27 p.

Fichaut B., Stéphan P., Suanez S., Amman J., Grandjean P. (2017). *Rapport sur le suivi morpho-sédimentaire sur le Sillon de Talbert pour l'année 2016*. Rapport d'étude, Laboratoire LETG-Brest Géomer (UMR 6554 CNRS), Université de Bretagne Occidentale, Institut Universitaire Européen de la Mer, avril 2017, 25 p.

Guérin T., Waeles B., Rivier A., Leballeur L., Stéphan P. (2020). *Sillon de Talbert : Etude des conditions hydrodynamiques*. Rapport d'étude, ACTIMAR & Laboratoire LETG (UMR 6554 CNRS), Université de Bretagne Occidentale, Institut Universitaire Européen de la Mer, Juin 2020, 79 p.

Stéphan P., Fichaut, B., Suanez, S. (2007). *Rapport d'activité sur le suivi topo-morphologique du Sillon de Talbert (Commune de Pleubian)*. Rapport d'étude, Laboratoire LETG-Brest Géomer (UMR 6554 CNRS), Université de Bretagne Occidentale, Institut Universitaire Européen de la Mer, 19 p.

Stéphan P., Fichaut, B., Suanez, S. (2008). Deuxième rapport d'activité sur le suivi topo-morphologique du Sillon de Talbert (Commune de Pleubian - Période 2007-2008). Rapport d'étude, Laboratoire LETG-Brest Géomer (UMR 6554 CNRS), Université de Bretagne Occidentale, Institut Universitaire Européen de la Mer, 12 p.

Stéphan P., Fichaut, B., Suanez, S. (2009). Suivi topo-morphologique du Sillon de Talbert (Commune de Pleubian - Période 2008-2009). Rapport d'étude, Laboratoire LETG-Brest Géomer (UMR 6554 CNRS), Université de Bretagne Occidentale, Institut Universitaire Européen de la Mer, 10 p.

Stéphan P., Fichaut, B., Suanez, S., Blaise E. (2011). Suivi topo-morphologique du Sillon de Talbert (Commune de Pleubian - Période 2010-2011). Rapport d'étude, Laboratoire LETG-Brest Géomer (UMR 6554 CNRS), Université de Bretagne Occidentale, Institut Universitaire Européen de la Mer, 10 p.

Stéphan P., Fichaut, B., Suanez, S., Blaise E. (2012). *Suivi topo-morphologique du Sillon de Talbert (Commune de Pleubian - Période 2011-2012)*. Rapport d'étude, Laboratoire LETG-Brest Géomer (UMR 6554 CNRS), Université de Bretagne Occidentale, Institut Universitaire Européen de la Mer, 14 p.

Stéphan P., Fichaut B., Suanez S., Blaise E., Autret R. (2015). *Rapport sur le suivi topo-morphologique du Sillon de Talbert pour l'année 2014*. Rapport d'étude, Laboratoire LETG-Brest Géomer (UMR 6554 CNRS), Université de Bretagne Occidentale, Institut Universitaire Européen de la Mer, mars 2015, 32 p.

Stéphan P., Fichaut B., Suanez S., Autret R., Houron J. (2018). *Rapport sur le suivi morpho-sédimentaire sur le Sillon de Talbert pour l'année 2017*. Rapport d'étude, Laboratoire LETG-Brest Géomer (UMR 6554 CNRS), Université de Bretagne Occidentale, Institut Universitaire Européen de la Mer, mars 2018, 47 p.

Stéphan P., Fichaut B., Suanez S., Ammann J., Tardieu I., James D., Mury A., Houron J. (2019) - *Suivi morphosédimentaire du sillon de Talbert pour l'année 2018*. Rapport scientifique, LETG-Brest UMR 6554 CNRS / UBO, 99 p. (avec annexes).

Stéphan P., Fichaut B., Suanez S., Ammann J., Tardieu I., Houron J. (2020). *Rapport sur le suivi morpho-sédimentaire sur le Sillon de Talbert pour l'année 2019*. Laboratoire LETG-Brest Géomer (UMR 6554 CNRS), Université de Bretagne Occidentale, Institut Universitaire Européen de la Mer, janvier 2020, 65 p. (avec annexes).

Stéphan P., Suanez S., Ammann J., David L., Houron J. (2022). *Rapport sur le suivi morpho-sédimentaire sur le Sillon de Talbert pour l'année 2021*. Laboratoire LETG-Brest Géomer (UMR 6554 CNRS), Université de Bretagne Occidentale, Institut Universitaire Européen de la Mer, février 2022, 61 p.

Stéphan P., Suanez S., Ammann J., David L., Mescoff I., Houron J. (2023). *Rapport sur le suivi morpho-sédimentaire sur le Sillon de Talbert pour l'année 2022*. Laboratoire LETG-Brest Géomer (UMR 6554 CNRS), Université de Bretagne Occidentale, Institut Universitaire Européen de la Mer, janvier 2023, 47 p.

Stéphan P., Suanez S., Ammann J., Fanton C., Houron J. (2024). *Rapport sur le suivi morpho-sédimentaire sur le Sillon de Talbert pour l'année 2023*. Laboratoire LETG-Brest Géomer (UMR 6554 CNRS), Université de Bretagne Occidentale, Institut Universitaire Européen de la Mer, février 2024, 53 p.

5.2. Articles scientifiques

Blaise E., Suanez S., Stéphan P., Fichaut B., David L., Cuq V., Autret R., Houron J., Rouan M., Floc'h F., Ardhuiind F., Cancouët R., Davidson R., Costa S., Delacourt C. (2015). Bilan des tempêtes de l'hiver 2013-2014 sur la dynamique de recul du trait de côte en Bretagne. *Géomorphologie : relief, processus, environnement*, 21 (3), pp. 267-292.

Stéphan P., Suanez S., Fichaut B. (2012b). Long-term morphodynamic evolution of the Sillon de Talbert gravel barrier spit, Brittany, France, *Shore & Beach*, 80, 1, pp. 19-36.

Stéphan P., Suanez S., Fichaut B., Autret R., Blaise E., Houron J., Ammann J., Grandjean P. (2018a). Monitoring the medium-term retreat of a gravel spit barrier and management strategies, Sillon de Talbert (North Brittany, France). *Ocean & Coastal Management*, 158, 64-82.

Stéphan P., Suanez S., Guérin T., Rivier A., Leballeur L., Waeles B., Ammann J., Houron J. (2024). Breaching of the Sillon de Talbert gravel spit (North Brittany, France) and coastal flooding risk assessment. *Geomorphology*, 461, 109302.

Suanez S., Stéphan P., Floc'h F., Autret R., Fichaut B., Blaise E., Houron J., Ammann J., Grandjean P., Accensi M., André G., Ardhuin F. (2018). Fifteen years of hydrodynamic forcing and morphological change leading to breaching of a gravel spit, Sillon de Talbert (Brittany, France). *Géomorphologie : Relief. Processus. Environnement*, 24, 4, 403-428.

Suanez S., Stéphan P., Autret R., Houron J., Floc'h F., David L., Ammann J., Accensi M., André G., Cancouët R., Le Guyader D. (2022). Catastrophic overwash and rapid retreat of a gravel barrier spit during storm events (Sillon de Talbert, North Brittany, France). *Earth, Process, Surface and Landforms*, 47, 8, 2024-2043.

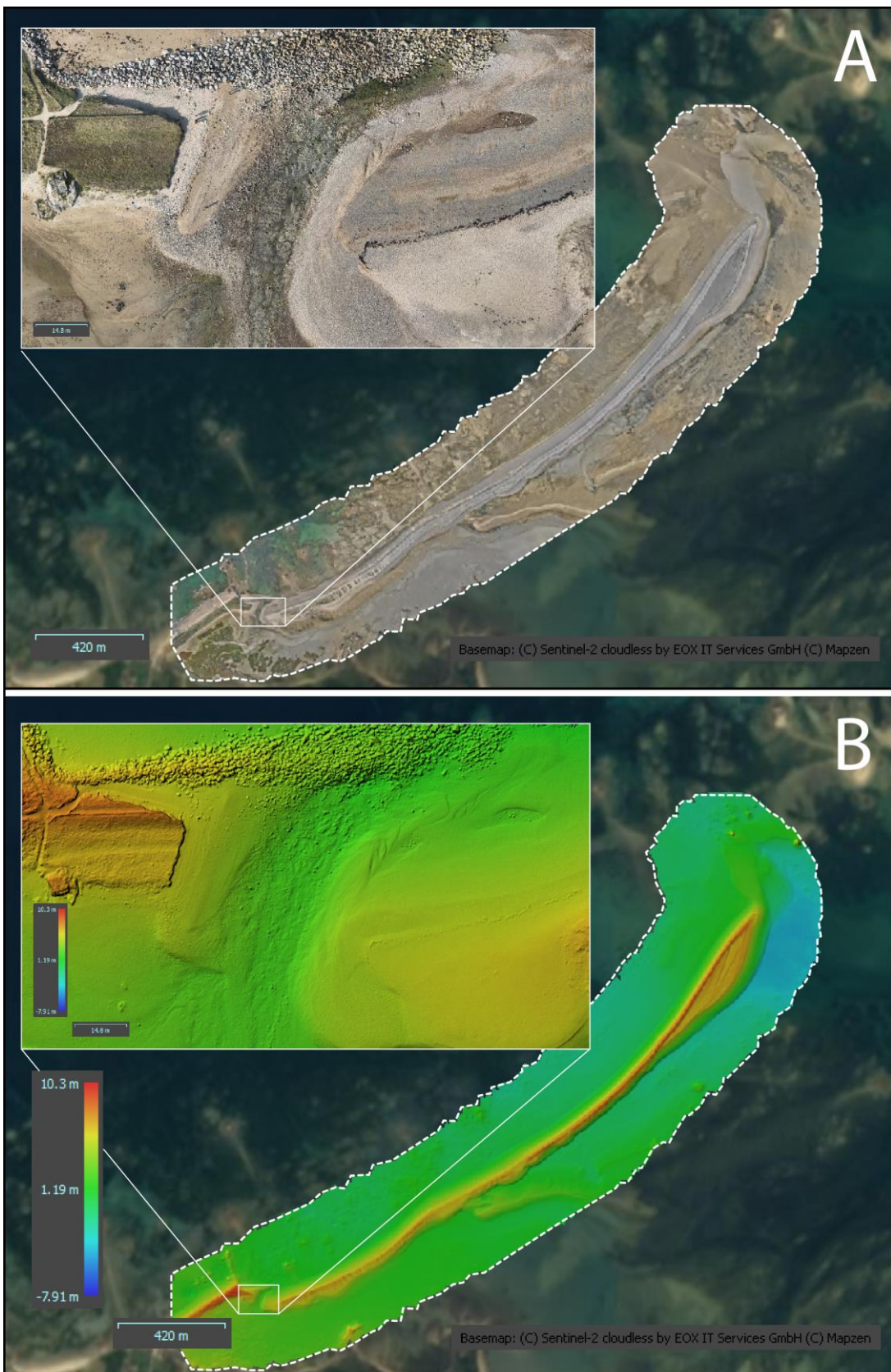


Figure 1 : Résultats du traitement photogrammétrique des prises de vues aériennes par drone réalisées le 18 septembre 2024 sur le Sillon de Talbert. A. Orthophotographie du secteur. B. Modèle numérique d'élévation obtenu après traitement des données.

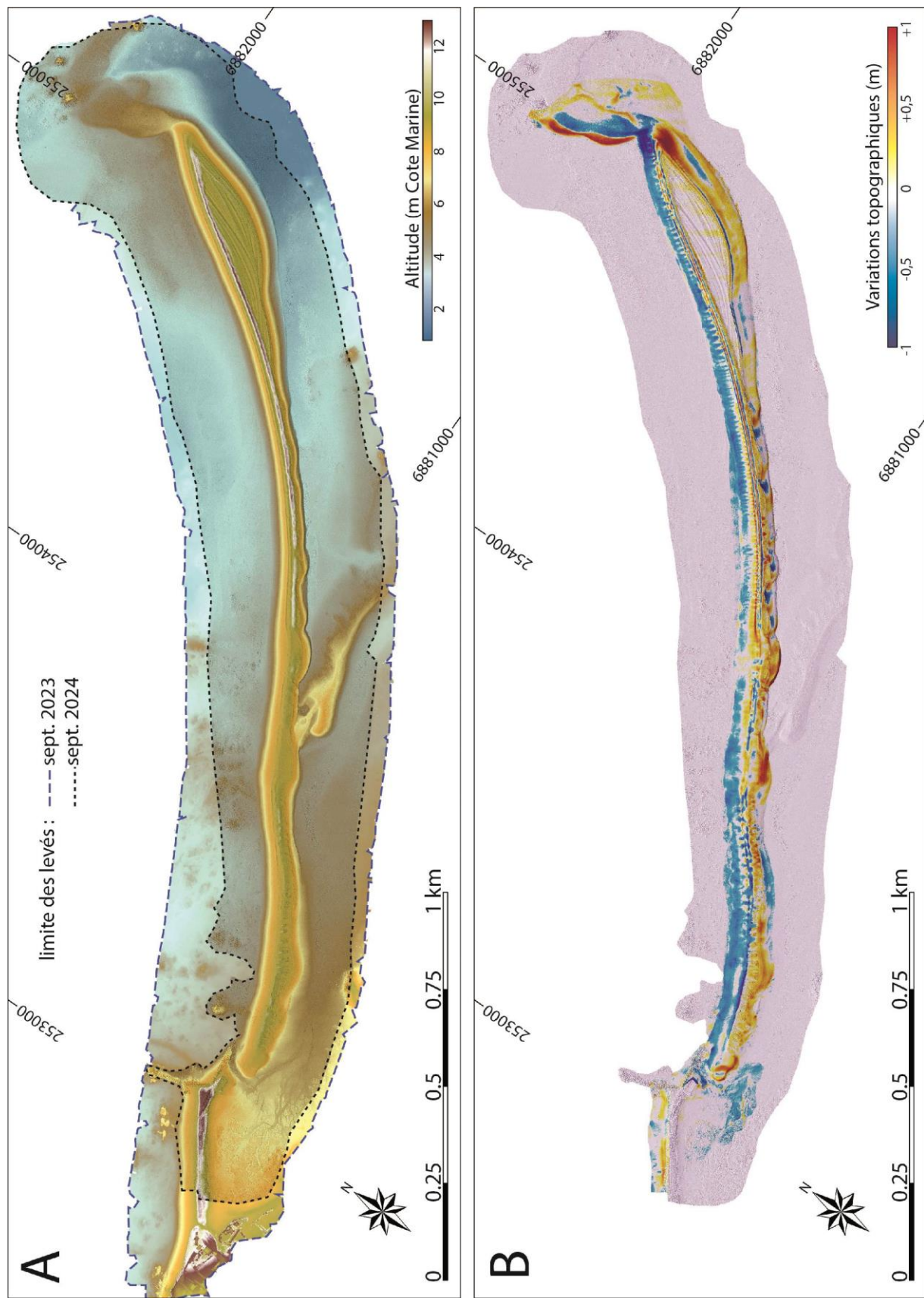


Figure 2 : Modèle Numérique de Terrain du Sillon de Talbert en septembre 2024 (A). Evolution topomorphologique du Sillon de Talbert entre septembre 2023 et septembre 2024.

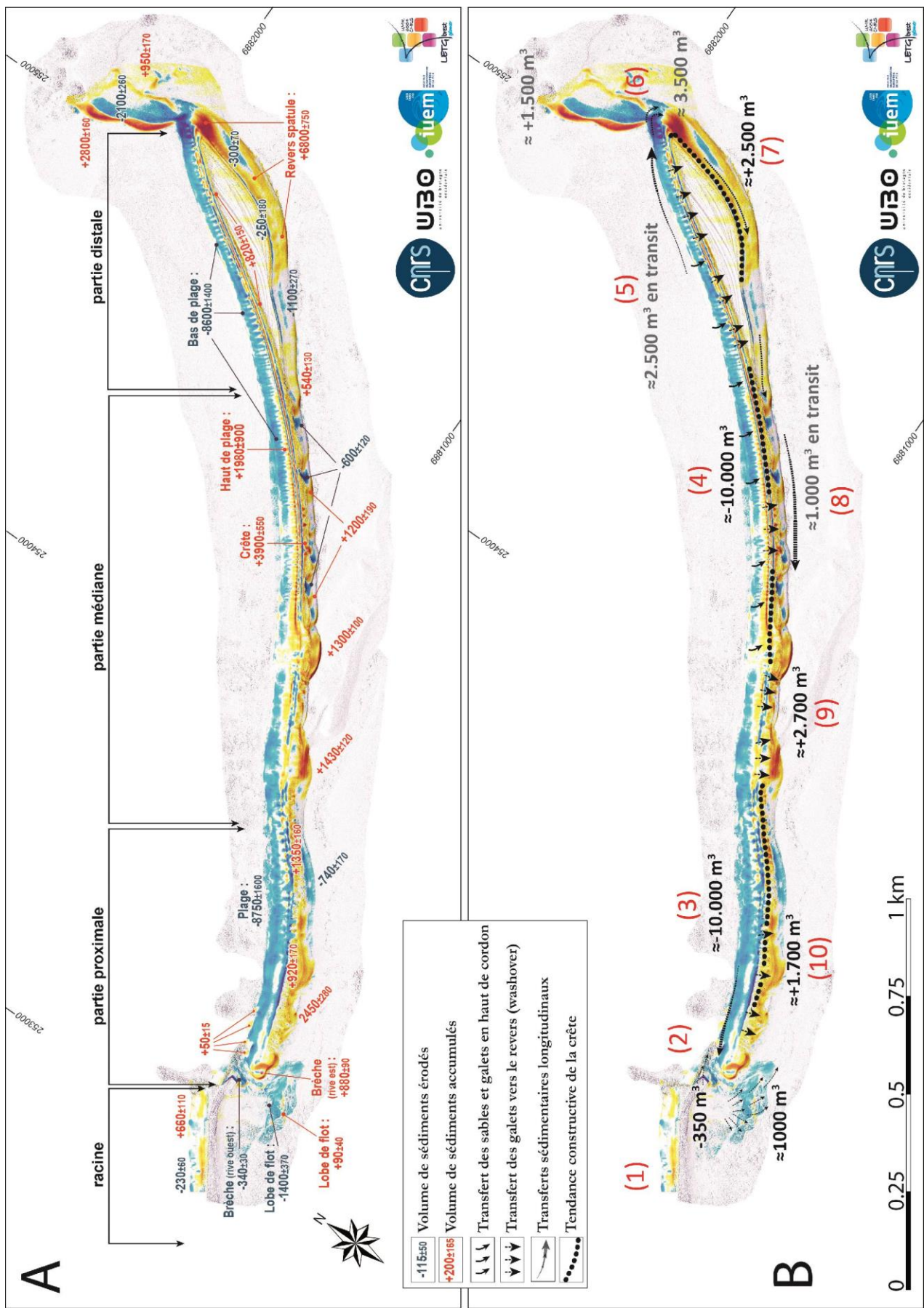


Figure 3 : Dynamiques morphosédimentaires sur le Sillon de Talbert entre septembre 2023 et septembre 2024.

Suivi morphologique du Sillon de Talbert – Pleubian – Période 2023-2024

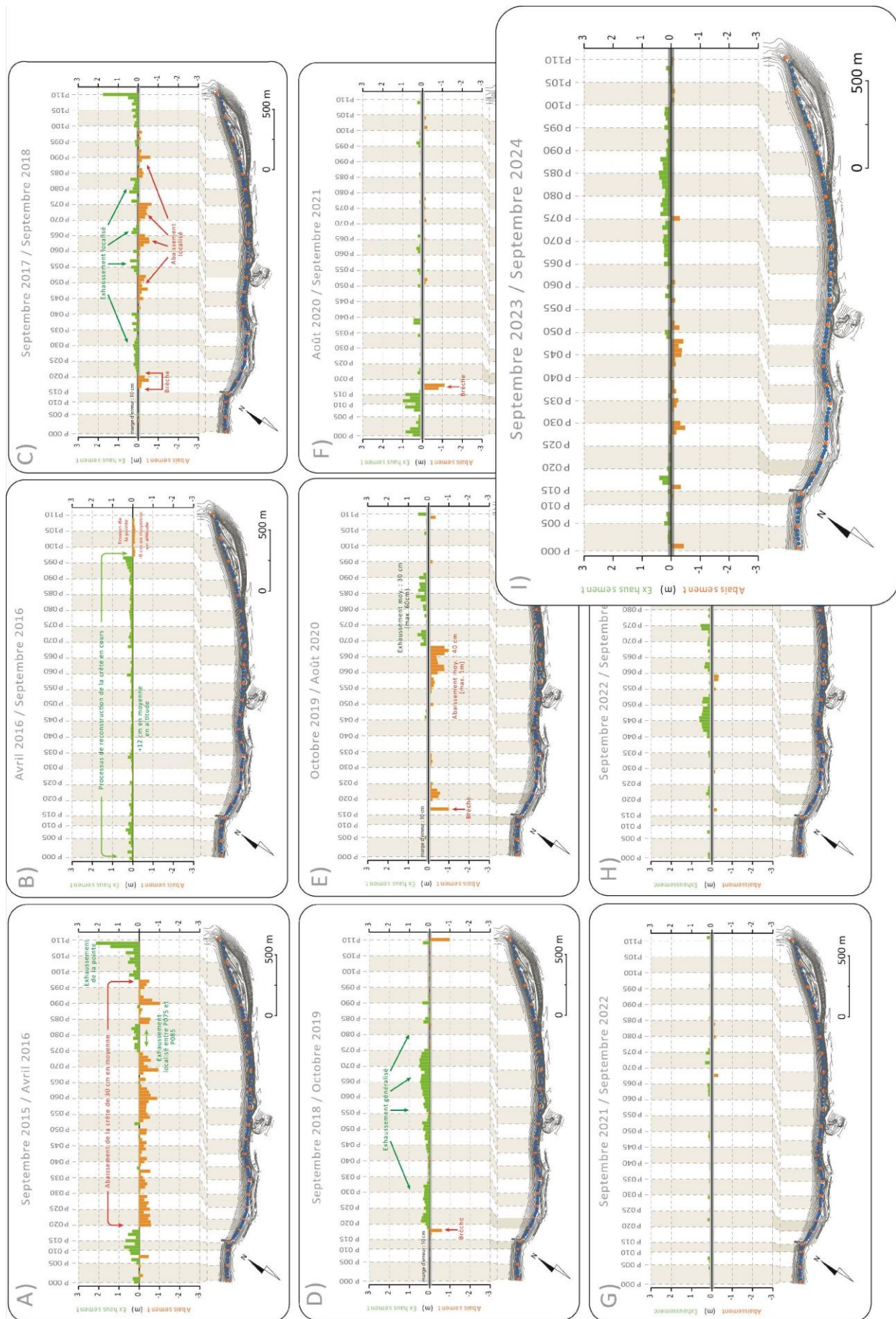


Figure 4 : Variations de l'altitude de la crête du Sillon de Talbert.

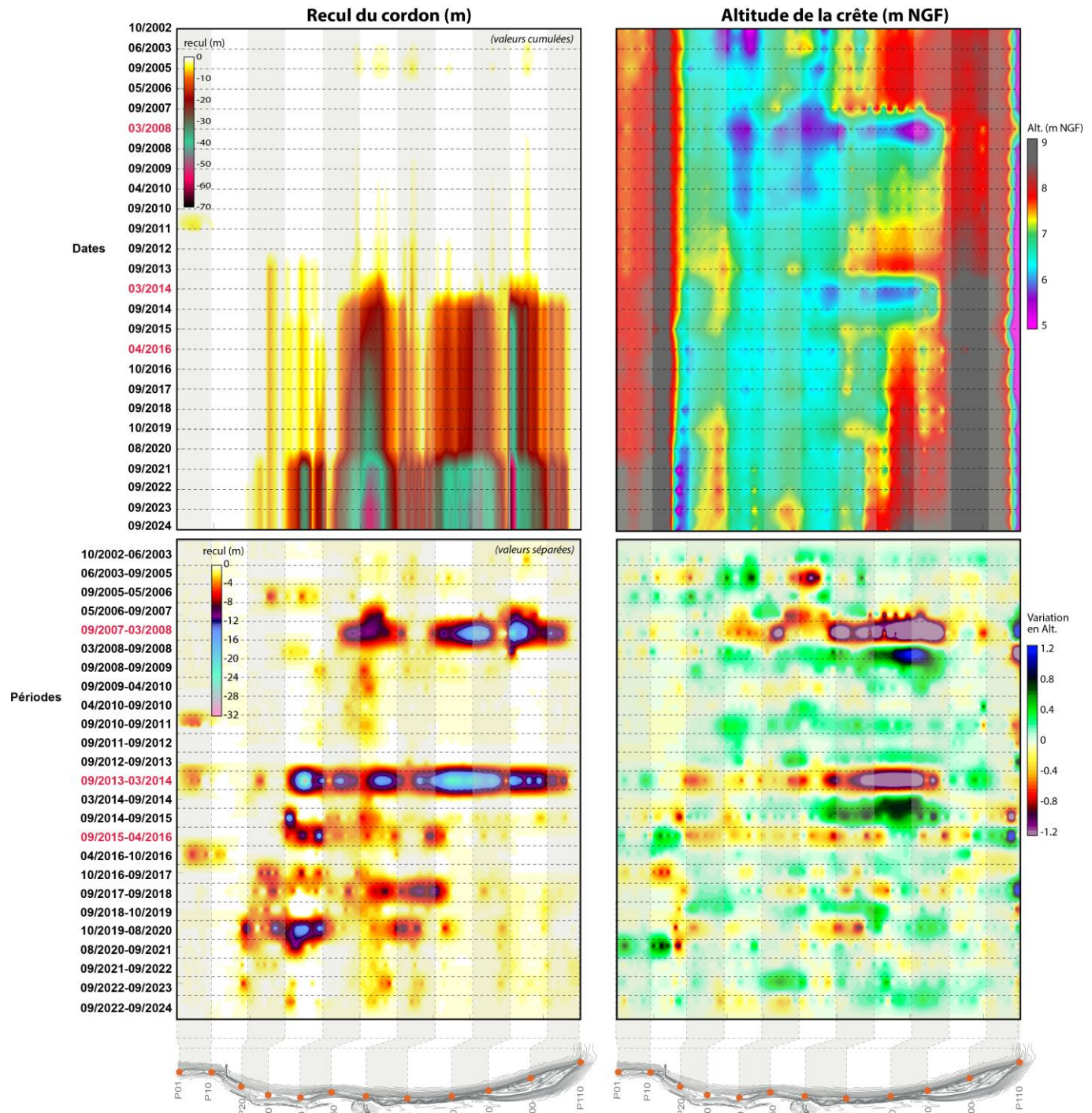


Figure 5 : valeurs du recul et de la hauteur du sillon de Talbert depuis le début des suivis en 2002.

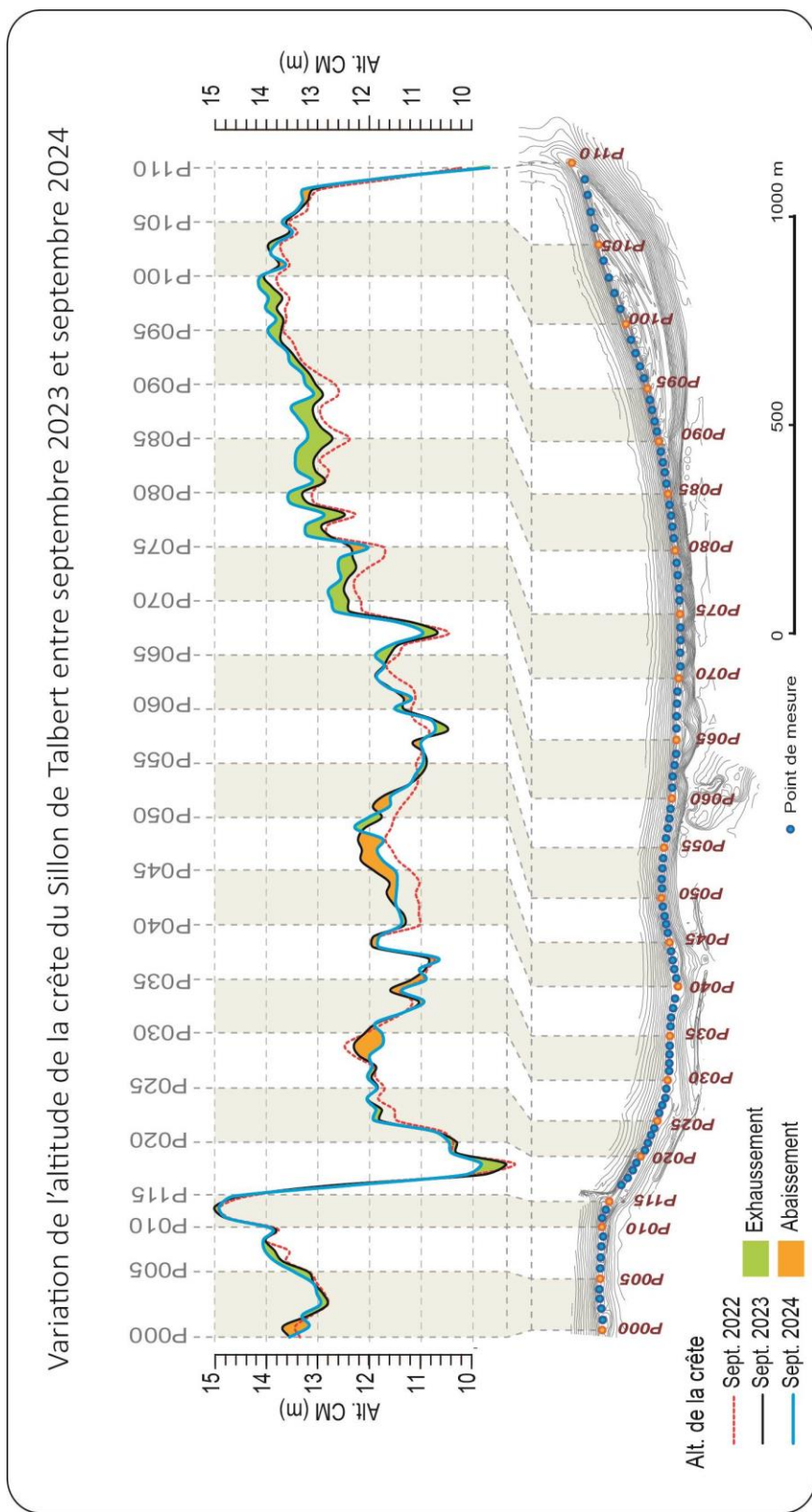


Figure 6 : Variations de l'altitude de la crête du Sillon de Talbert entre septembre 2023 et septembre 2024.

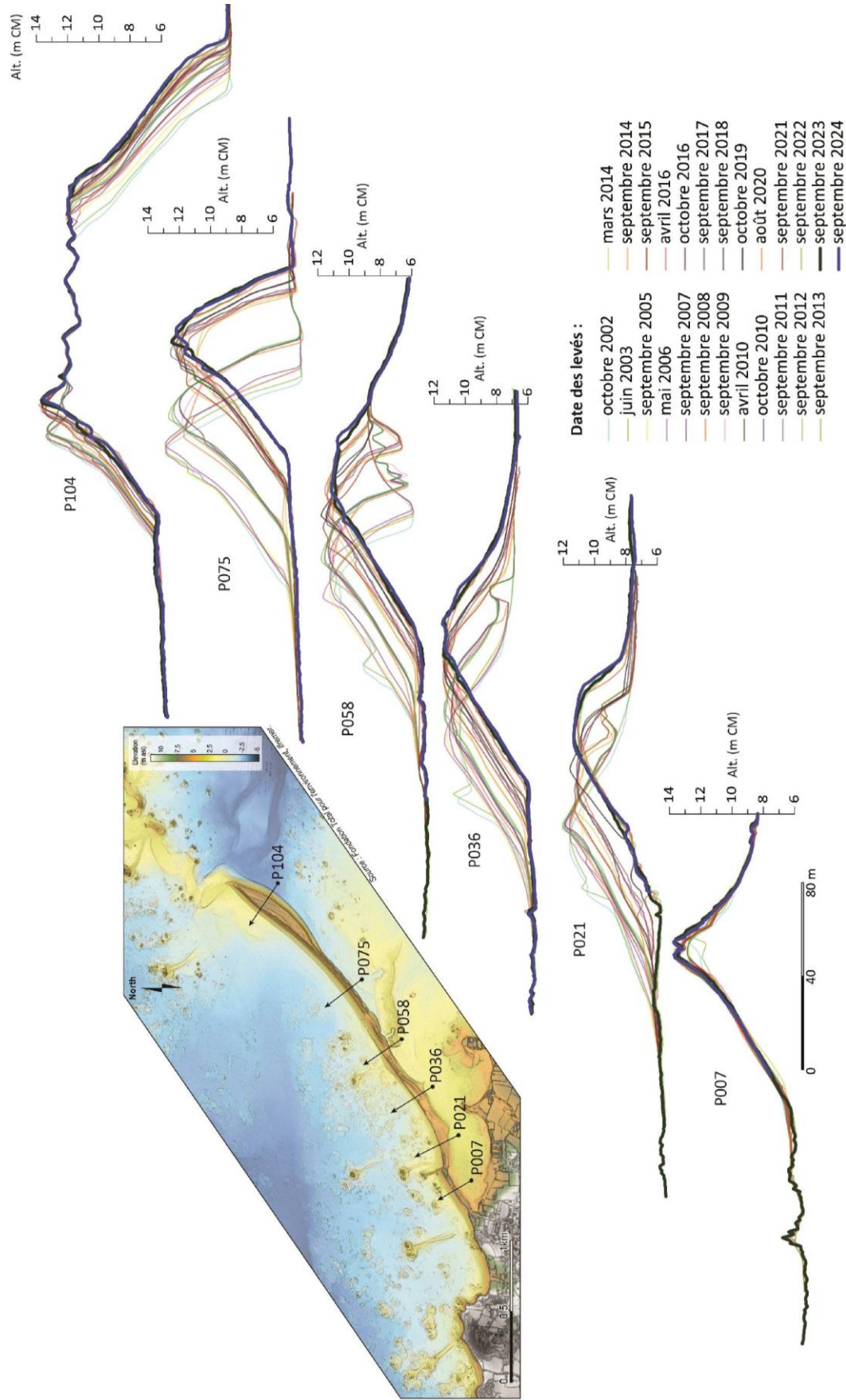


Figure 7 : Evolution des profils transversaux du sillon de Talbert.

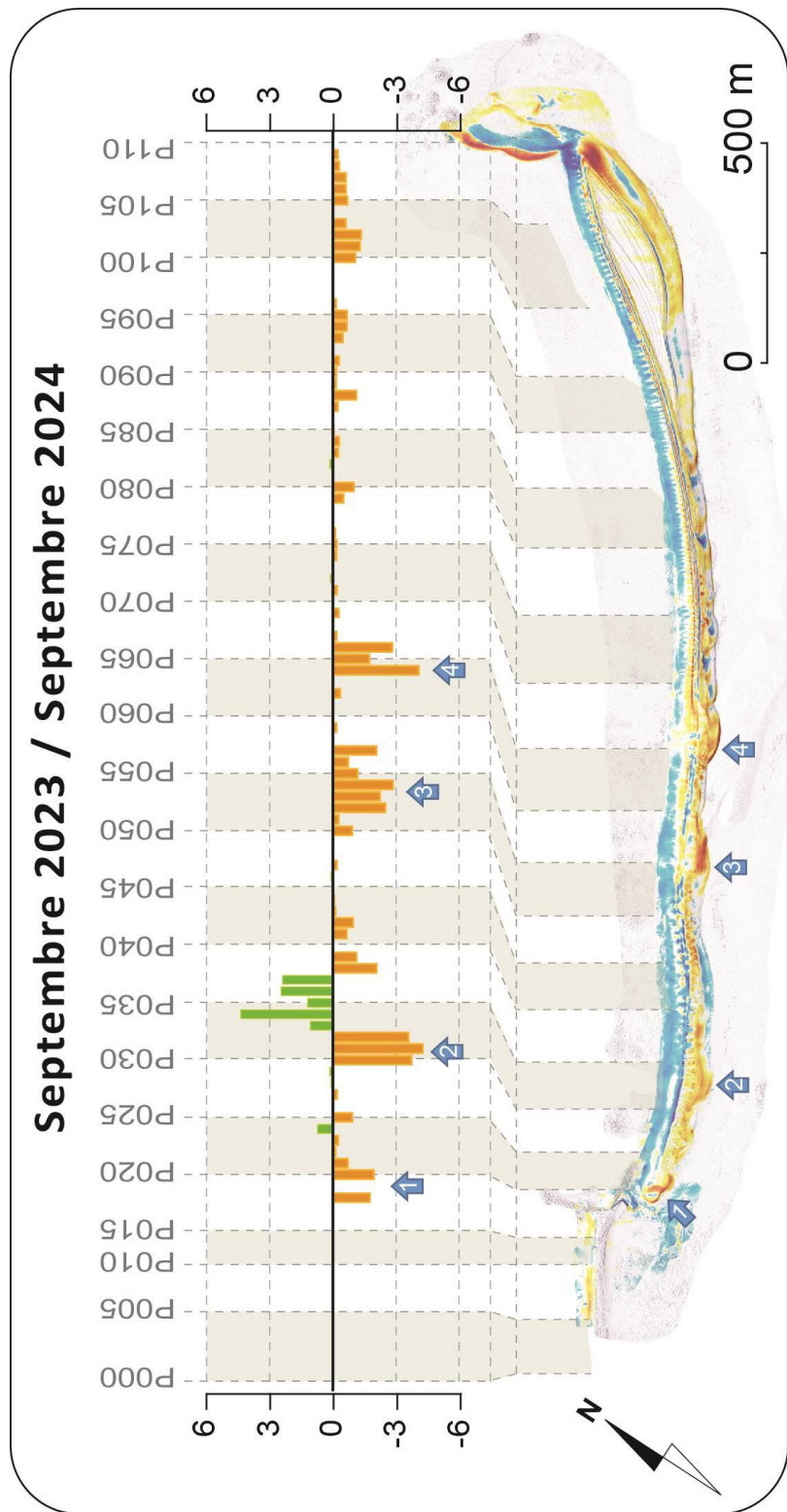


Figure 8 : Recul de la base du revers du Sillon de Talbert entre septembre 2023 et septembre 2024.

Suivi morphologique du Sillon de Talbert – Pleubian – Période 2023-2024

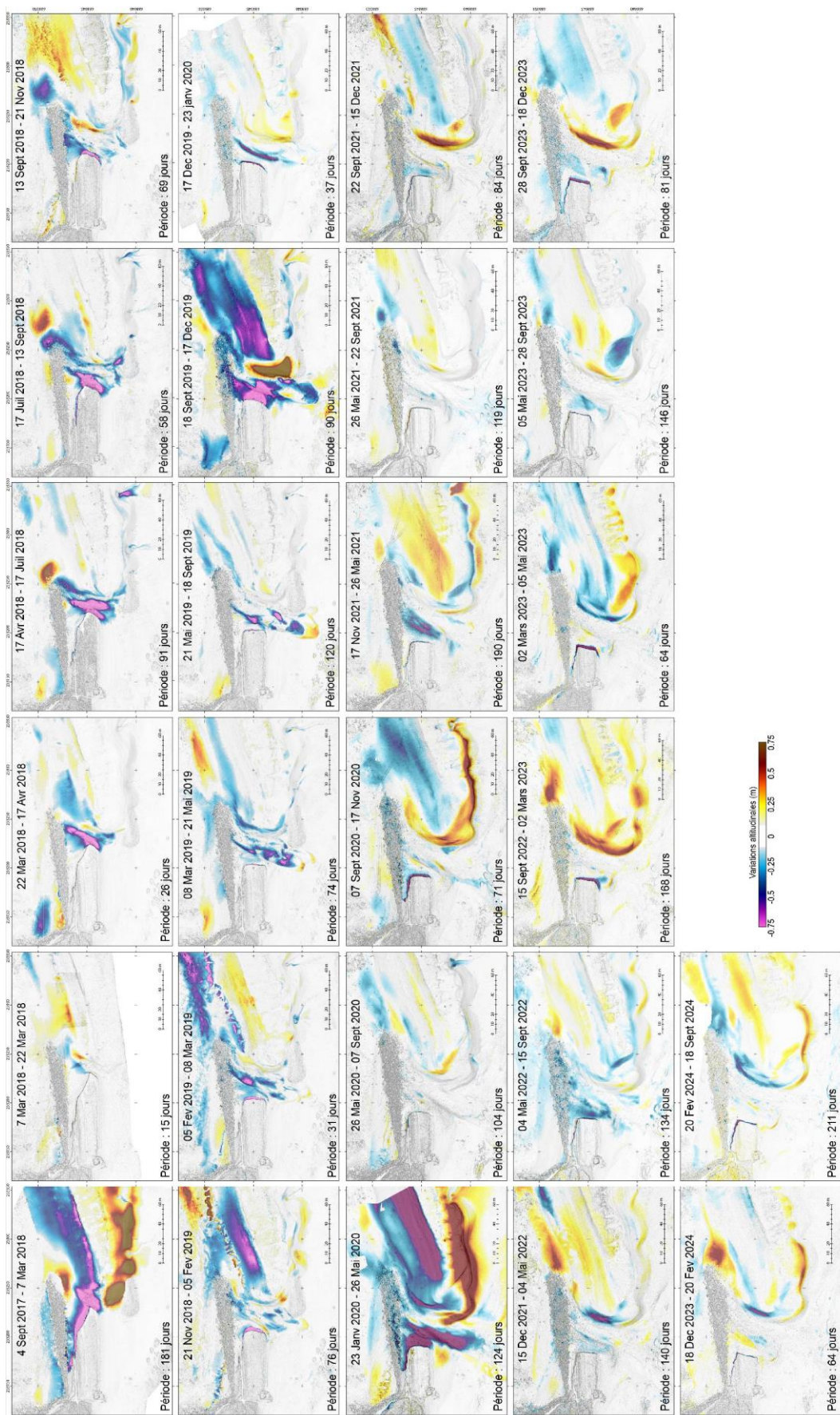


Figure 9 : Evolution topo-morphologique dans le secteur de la brèche (partie proximale du Sillon de Talbert) entre septembre 2017 et septembre 2024.

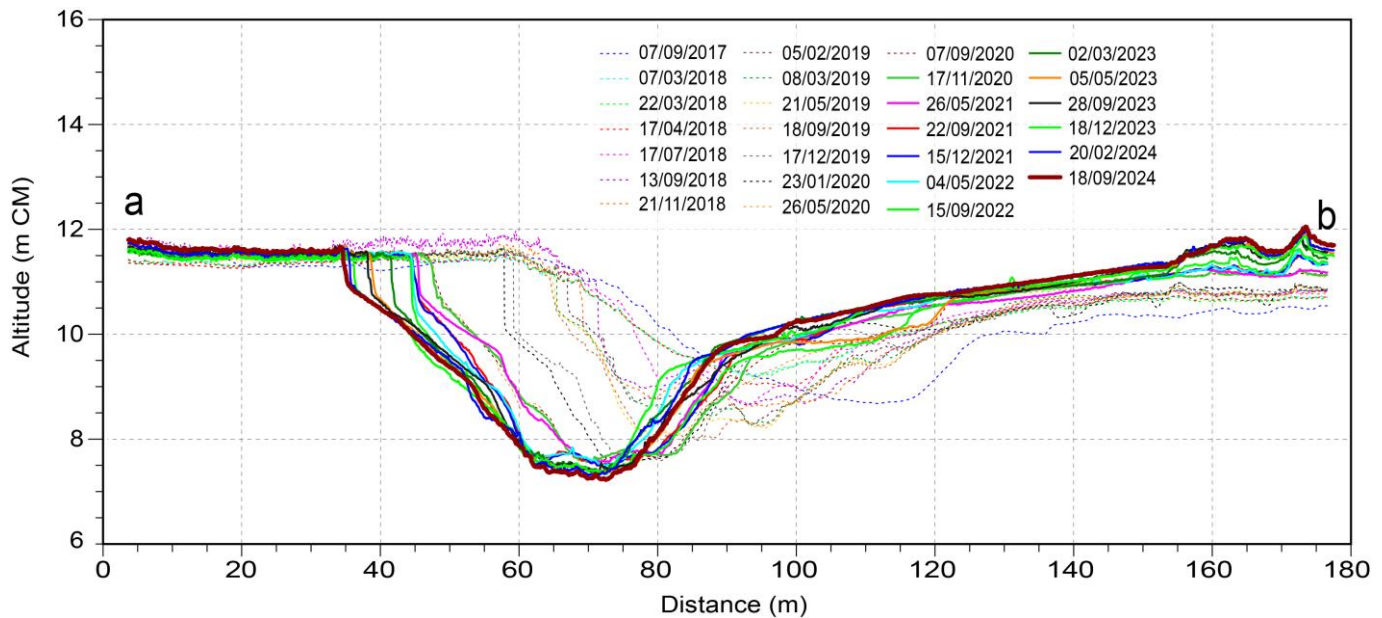


Figure 10 : Evolution du profil transversal de la brèche. L'axe de ce profil est localisé sur la Figure 12.

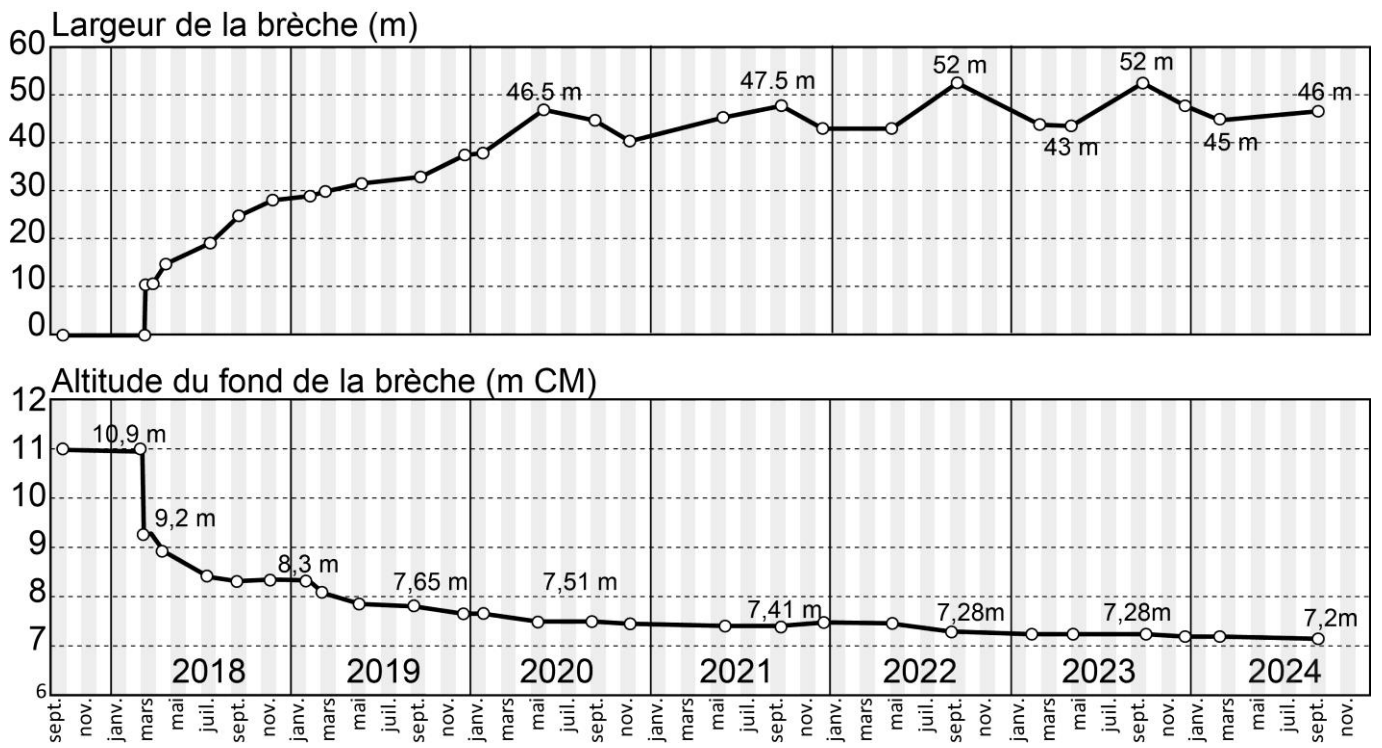


Figure 11 : Largeur et altitude de la brèche (partie proximale du Sillon de Talbert) entre septembre 2017 et septembre 2023. La largeur de la brèche à la distance minimale qui sépare la ligne des pleines-mers de vive eau de part et d'autre de la brèche. L'incision est mesurée en considérant la plus basse altitude mesurée dans la brèche.

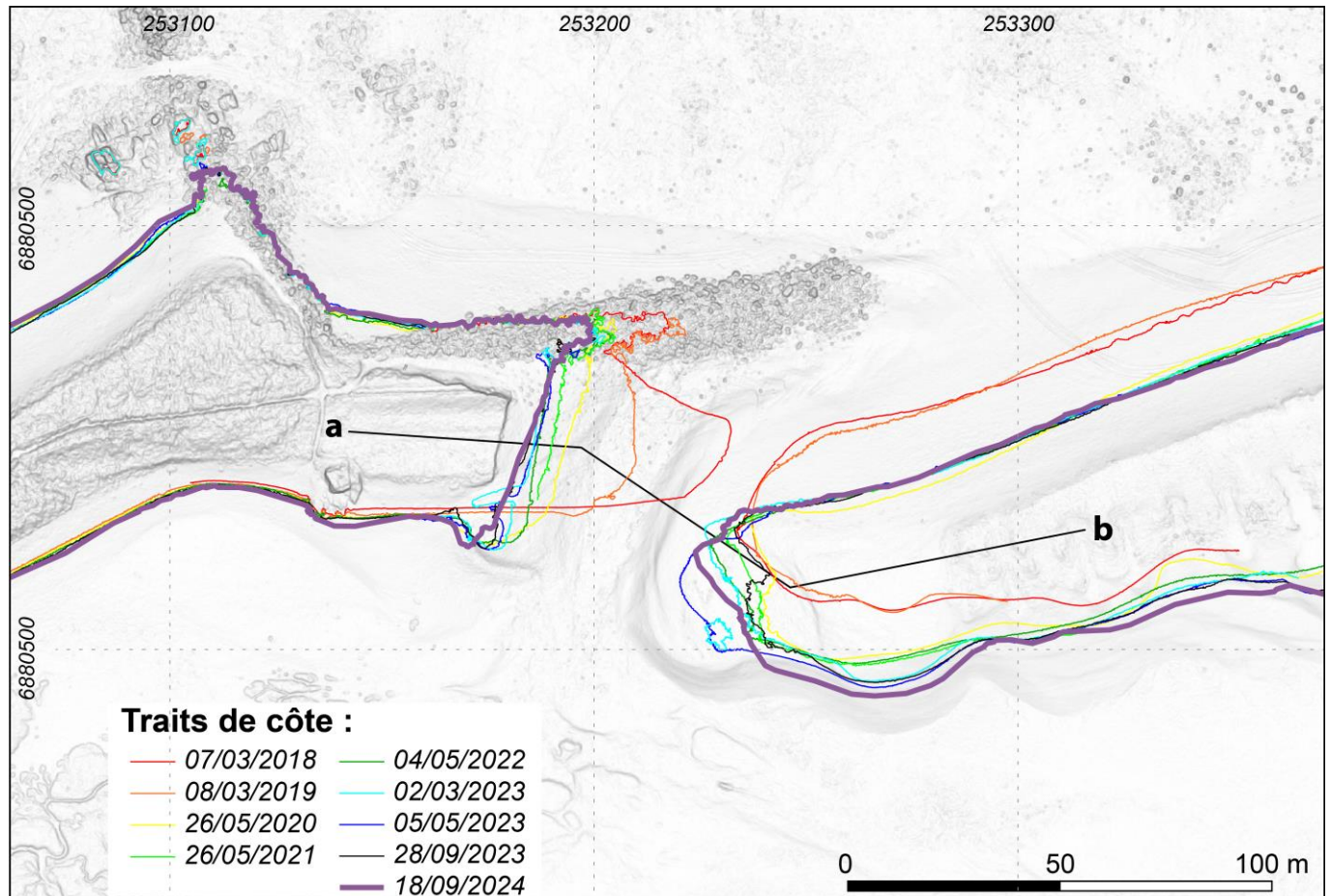


Figure 12 : Evolution du trait de côte au niveau de la brèche entre mars 2018 et septembre 2024.
Seuls quelques traits de côte représentatifs ont été figurés et correspondent à la ligne des pleines mers de vive-eau.

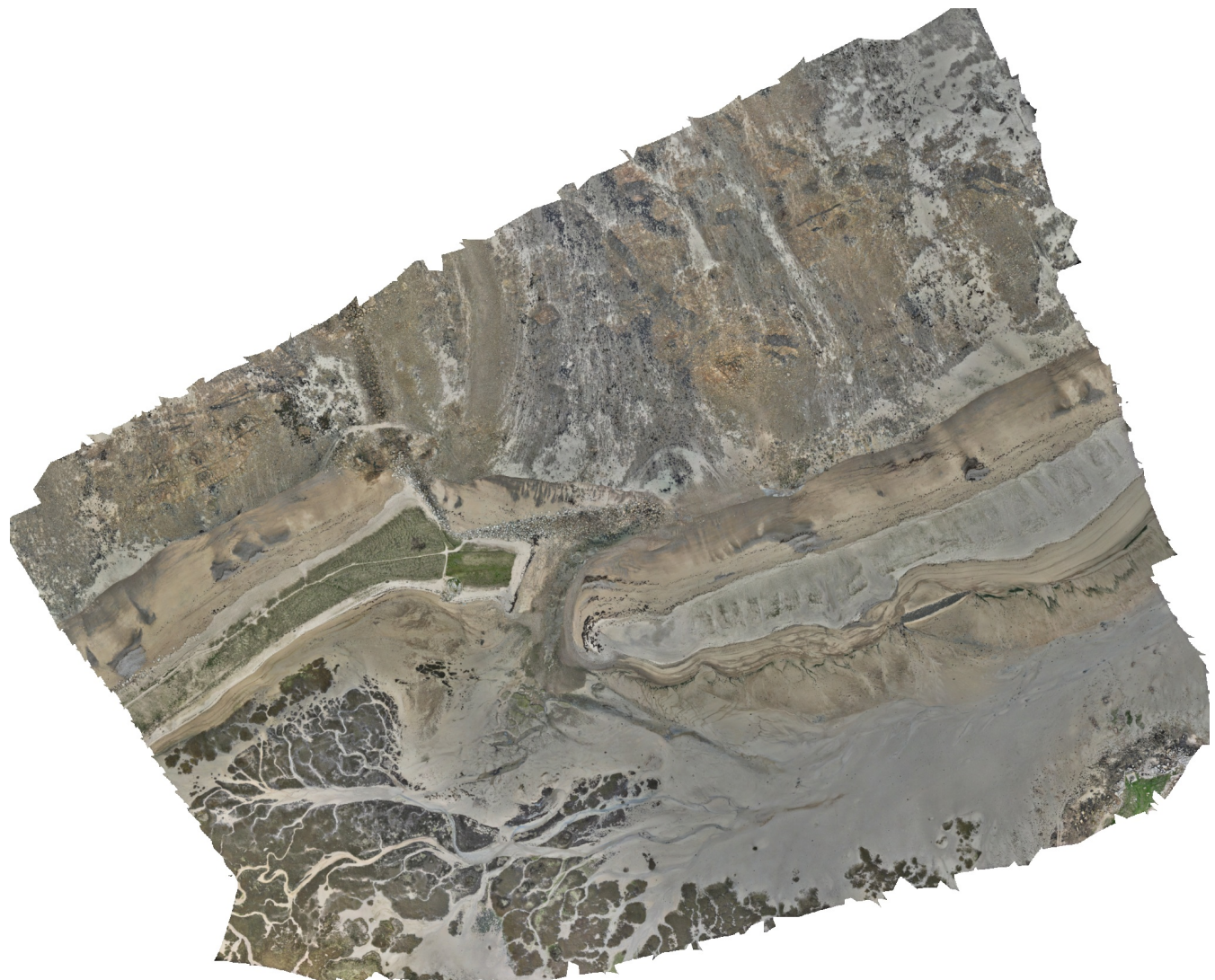
Annexe 1

Détail des traitements photogrammériques (rapports des traitements réalisés à partir du logiciel Agisoft Metashape).

Talbert_20231218_Rapport

Rapport de traitement Metashape

20 December 2023



Données du levé

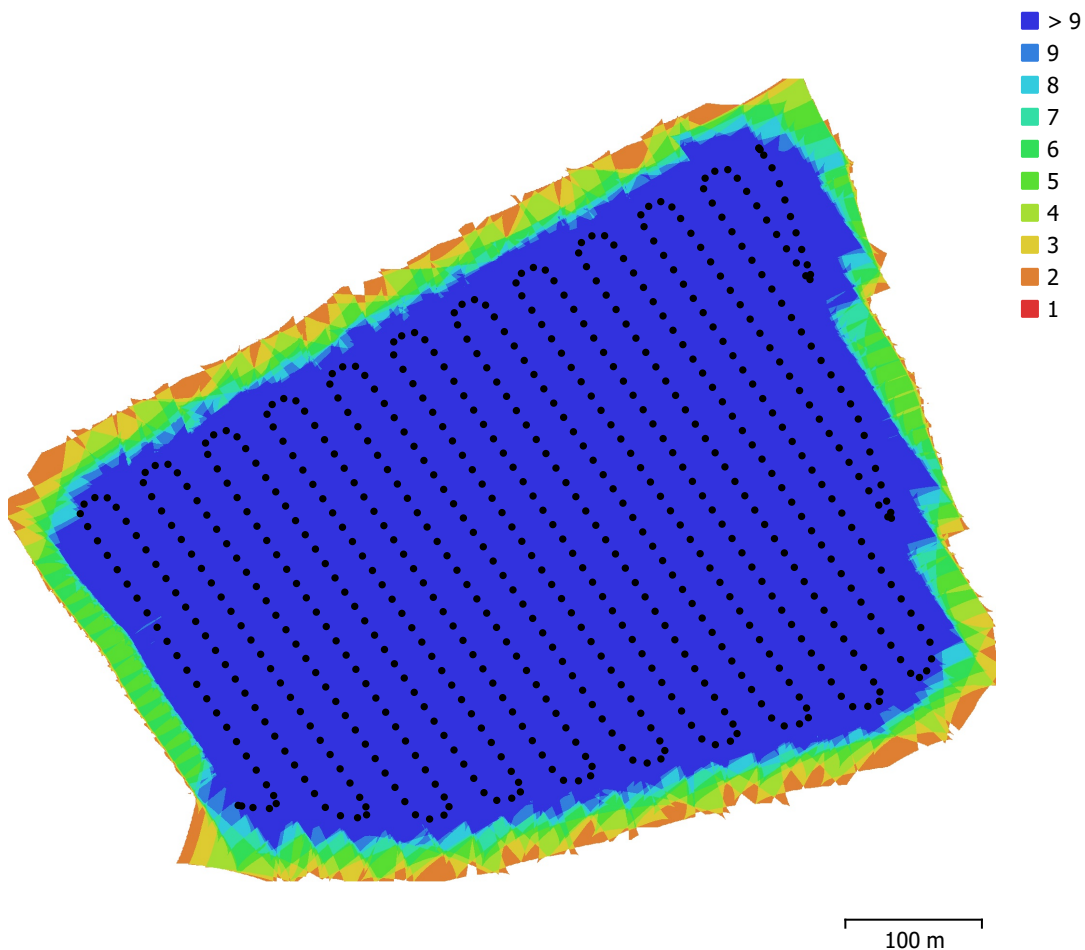


Fig. 1. Emplacements des caméras et chevauchement des images.

| | | | |
|---------------------|-----------------------|-------------------------|-----------|
| Nombre d'images: | 655 | Stations de caméras: | 655 |
| Altitude de vol: | 63.2 m | Points de liaison: | 468,253 |
| Résolution au sol: | 1.67 cm/px | Projections: | 5,313,309 |
| Zone de couverture: | 0.274 km ² | Erreur de reprojection: | 0.476 px |

| Modèle de caméra | Résolution | Longueur focale | Taille de pixel | Précalibré |
|------------------|-------------|-----------------|-----------------|------------|
| M3E (12.29mm) | 5280 x 3956 | 12.29 mm | 3.36 x 3.36 µm | Oui |

Tableau 1. Caméras.

Calibration de la caméra

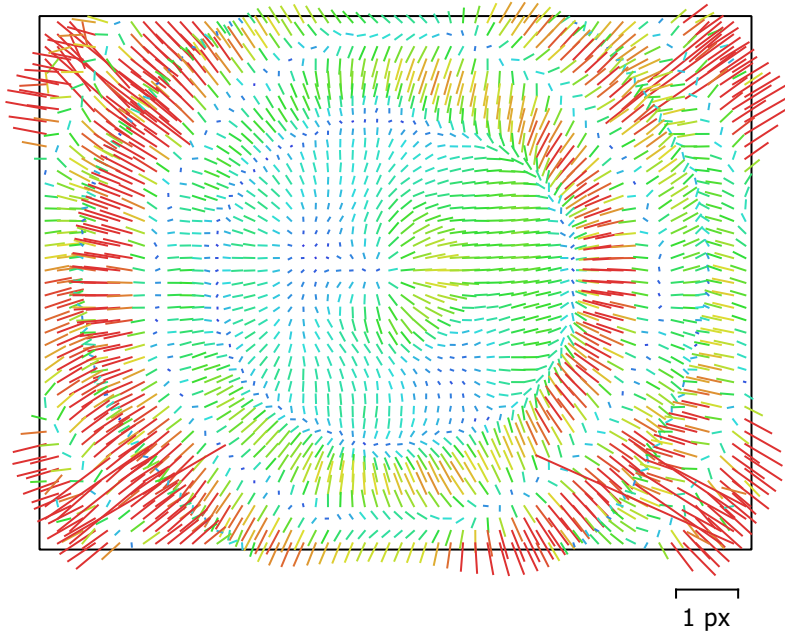


Fig. 2. Résiduelles des points de liaison pour M3E (12.29mm).

M3E (12.29mm)

655 images, Précalibré

| Type | Résolution | Longueur focale | Taille de pixel |
|-------|-------------|-----------------|-----------------|
| Cadre | 5280 x 3956 | 12.29 mm | 3.36 x 3.36 µm |

| | Valeur | Erreur | F | Cx | Cy | B1 | B2 | K1 | K2 | K3 | K4 | P1 | P2 |
|-----------|---------------------|---------|------|------|------|-------|-------|-------|-------|-------|-------|-------|-------|
| F | 3620.23 | 0.51 | 1.00 | 0.54 | 0.45 | -0.01 | 0.02 | -0.91 | -0.80 | 0.89 | -0.95 | -0.54 | -0.43 |
| Cx | -4.48233 | 0.016 | | 1.00 | 0.22 | -0.04 | -0.00 | -0.49 | -0.43 | 0.48 | -0.51 | -0.90 | -0.21 |
| Cy | -21.1754 | 0.015 | | | 1.00 | 0.01 | -0.03 | -0.41 | -0.37 | 0.41 | -0.43 | -0.22 | -0.91 |
| B1 | -0.117467 | 0.0016 | | | | 1.00 | 0.02 | 0.02 | -0.01 | 0.00 | 0.00 | 0.03 | -0.01 |
| B2 | 0.0527739 | 0.0016 | | | | | 1.00 | -0.02 | -0.01 | 0.02 | -0.02 | -0.01 | 0.02 |
| K1 | -0.0806681 | 2.5e-05 | | | | | | 1.00 | 0.49 | -0.64 | 0.75 | 0.49 | 0.39 |
| K2 | -0.102088 | 7.2e-05 | | | | | | | 1.00 | -0.98 | 0.95 | 0.43 | 0.35 |
| K3 | 0.160259 | 0.00015 | | | | | | | | 1.00 | -0.99 | -0.48 | -0.39 |
| K4 | -0.0973055 | 0.00012 | | | | | | | | | 1.00 | 0.51 | 0.41 |
| P1 | -8.17042e-05 | 5.9e-07 | | | | | | | | | | 1.00 | 0.21 |
| P2 | 2.03249e-05 | 5.2e-07 | | | | | | | | | | | 1.00 |

Tableau 2. Coefficients de calibration et matrice de corrélation.

Points de contrôle au sol

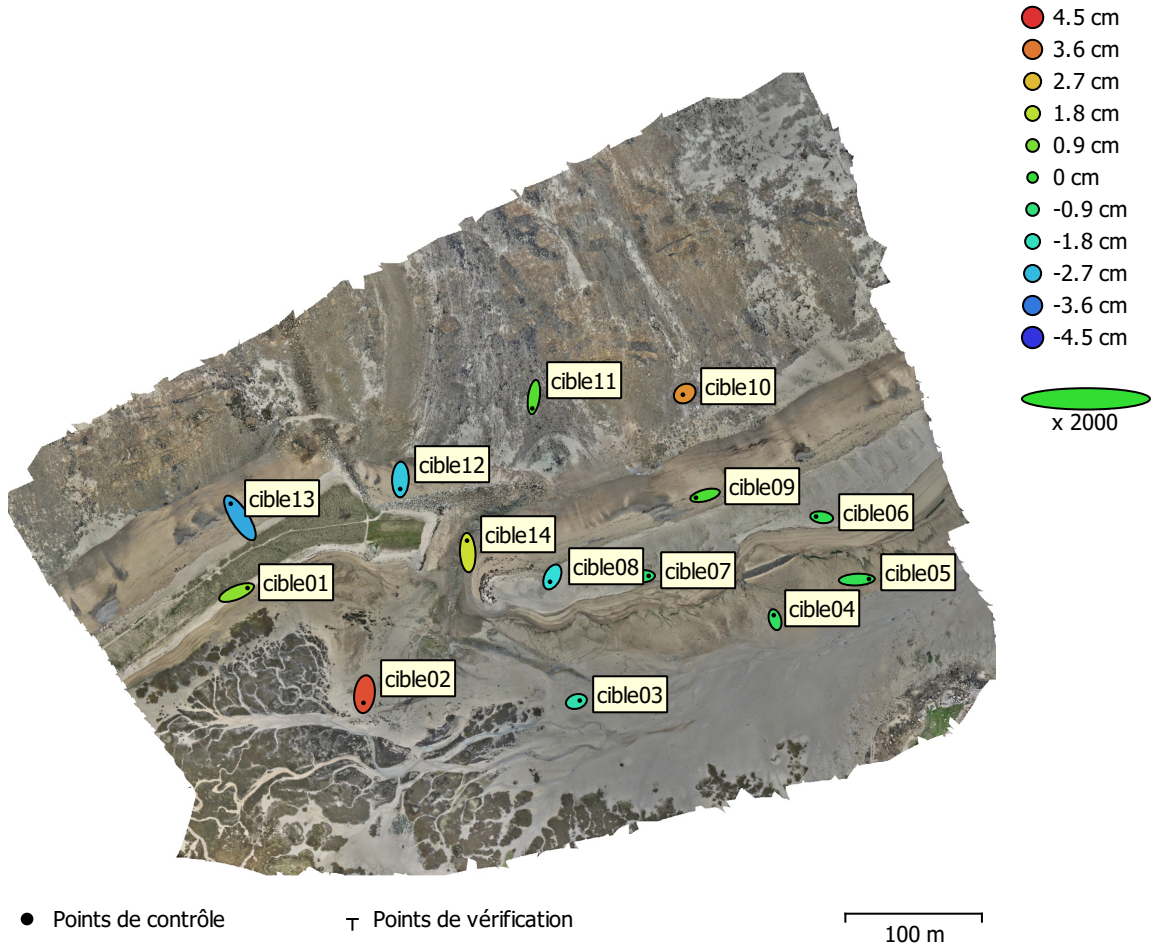


Fig. 3. Emplacements des points de contrôle au sol et estimations d'erreur.

L'erreur Z est représentée par la couleur de l'ellipse. Les erreurs X et Y sont représentées par la forme de l'ellipse. Les emplacements estimés des points de contrôle au sol sont marqués d'un point ou d'une croix.

| Nombre | Erreur X (cm) | Erreur Y (cm) | Erreur Z (cm) | Erreur XY (cm) | Total (cm) |
|--------|---------------|---------------|---------------|----------------|------------|
| 14 | 0.452408 | 0.52334 | 2.02384 | 0.691778 | 2.13881 |

Tableau 3. Points de contrôle RMSE.

X - Est, Y - Nord, Z - Altitude.

| Etiquette | Erreur X (cm) | Erreur Y (cm) | Erreur Z (cm) | Total (cm) | Image (px) |
|------------------|----------------------|----------------------|----------------------|-------------------|-------------------|
| cible13 | -0.672402 | 1.0501 | -2.95476 | 3.20709 | 0.806 (18) |
| cible12 | -0.0186742 | -0.693513 | -2.53862 | 2.63171 | 0.728 (17) |
| cible01 | 0.804718 | 0.329864 | 1.19745 | 1.47995 | 0.799 (18) |
| cible14 | -0.049948 | 0.875385 | 2.02401 | 2.20577 | 1.042 (22) |
| cible08 | -0.17045 | -0.354882 | -2.16211 | 2.19766 | 0.672 (16) |
| cible03 | 0.244314 | 0.0679504 | -1.57571 | 1.59599 | 0.735 (20) |
| cible07 | 0.470833 | 0.0275444 | -0.748051 | 0.88432 | 0.522 (15) |
| cible09 | -0.668498 | -0.17421 | 0.341194 | 0.770488 | 0.843 (18) |
| cible06 | -0.412212 | 0.0511528 | -0.406821 | 0.581411 | 0.506 (18) |
| cible05 | 0.888837 | 0.0421173 | -0.425396 | 0.98629 | 0.474 (17) |
| cible04 | -0.0916453 | 0.327085 | -0.608372 | 0.696778 | 0.535 (16) |
| cible11 | -0.114836 | -0.831628 | 0.43747 | 0.946663 | 1.230 (23) |
| cible10 | -0.13643 | -0.0810452 | 3.27985 | 3.28369 | 1.273 (19) |
| cible02 | -0.0736074 | -0.635919 | 4.13987 | 4.18907 | 1.023 (20) |
| Total | 0.452408 | 0.52334 | 2.02384 | 2.13881 | 0.861 |

Tableau 4. Points de contrôle.

X - Est, Y - Nord, Z - Altitude.

Modèle Numérique d'élévation

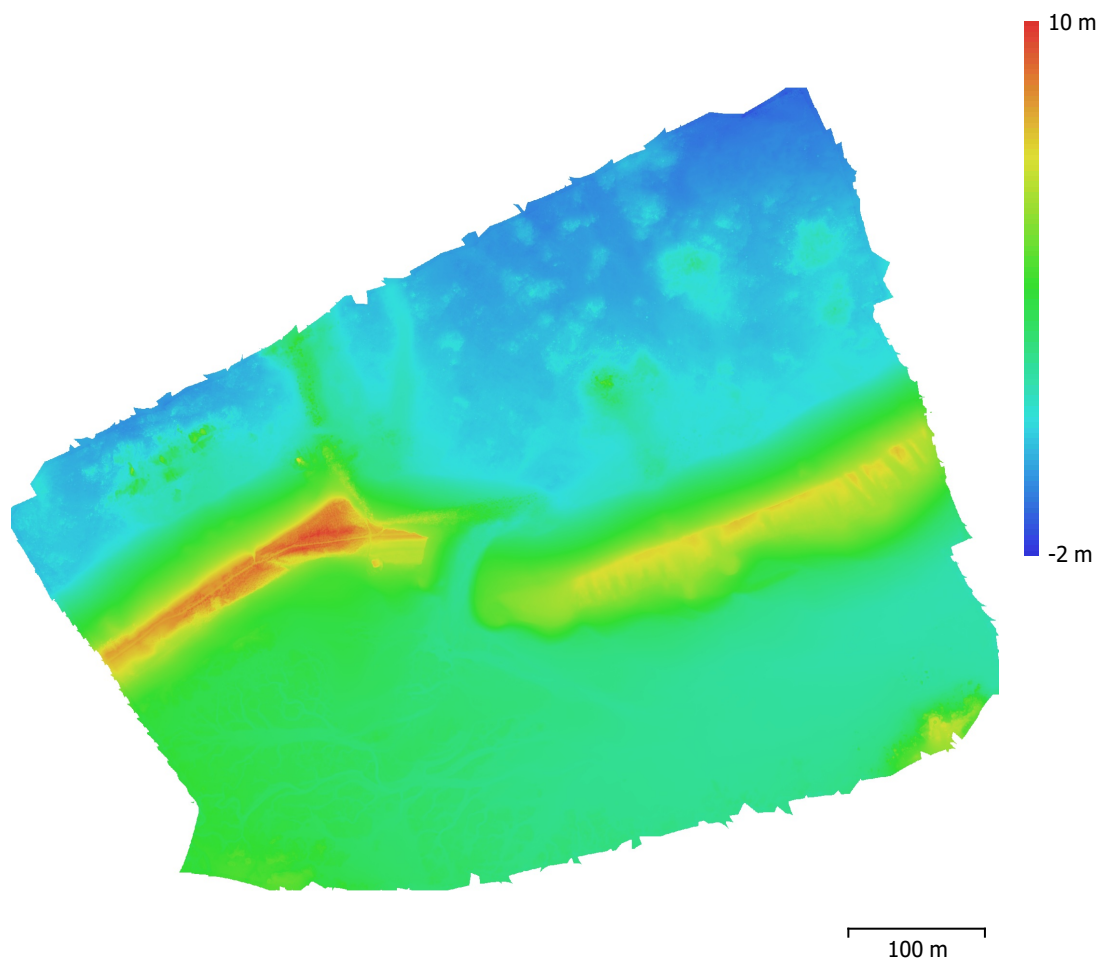


Fig. 4. Modèle numérique d'élévation reconstruit.

Résolution: 3.49 cm/px

Densité des points: 819 points/m²

Paramètres de traitement

Général

| | |
|------------------------|---------------------------------|
| Caméras | 655 |
| Caméras alignées | 655 |
| Repères | 14 |
| Système de coordonnées | RGF93 / Lambert-93 (EPSG::2154) |
| Angles de rotation | Lacet, Tangage, Roulis |

NUAGE DE POINT

| | |
|--|------------------------|
| Points | 468,253 de 686,316 |
| Erreur RMS de reprojection | 0.186196 (0.476328 px) |
| Erreur Max de reprojection | 1.37035 (4.95863 px) |
| Taille moyenne de point | 2.62716 px |
| Couleurs des points | 3 bandes, uint8 |
| Points-clé | 3.10 GB |
| Multiplicité moyenne des points de liaison | 10.1967 |

PARAMÈTRES D'ALIGNEMENT

| | |
|--|------------------------|
| Précision | Haute |
| Présélection générique | Oui |
| Présélection par références | Source |
| Limite de points | 60,000 |
| Limite de points-clé par Mpx | 60,000 |
| Limite de points de liaison | 10,000 |
| Exclure les points de liaison fixes | Non |
| Correspondance d'images guidée | Non |
| Ajustement progressif du modèle de la caméra | Non |
| Temps de concordance | 10 minutes 53 secondes |
| Utilisation de la mémoire de correspondance | 857.67 MB |
| Temps d'alignement | 8 minutes 29 secondes |
| Utilisation de la mémoire d'alignement | 784.96 MB |

PARAMÈTRES D'OPTIMISATION

| | |
|--|----------------------------------|
| Paramètres | f, b1, b2, cx, cy, k1-k4, p1, p2 |
| Ajustement progressif du modèle de la caméra | Oui |
| Durée d'optimisation | 27 secondes |
| Date de création | 2023:12:19 11:01:42 |
| Version du programme | 1.8.5.15709 |
| Taille du fichier | 146.26 MB |

CARTES DE PROFONDEUR

| | |
|--------|-----|
| Nombre | 655 |
|--------|-----|

PARAMÈTRES DE GÉNÉRATION DES CARTES DE PROFONDEUR

| | |
|---------------------------|------------------------|
| Qualité | Haute |
| Mode de filtrage | Agressif |
| Max voisins | 16 |
| Temps de traitement | 41 minutes 10 secondes |
| Utilisation de la mémoire | 5.64 GB |
| Date de création | 2023:12:19 13:45:07 |
| Version du programme | 1.8.5.15709 |
| Taille du fichier | 5.13 GB |

NUAGE DE POINTS DENSE

| | |
|---------------------|-----------------|
| Points | 260,159,966 |
| Couleurs des points | 3 bandes, uint8 |

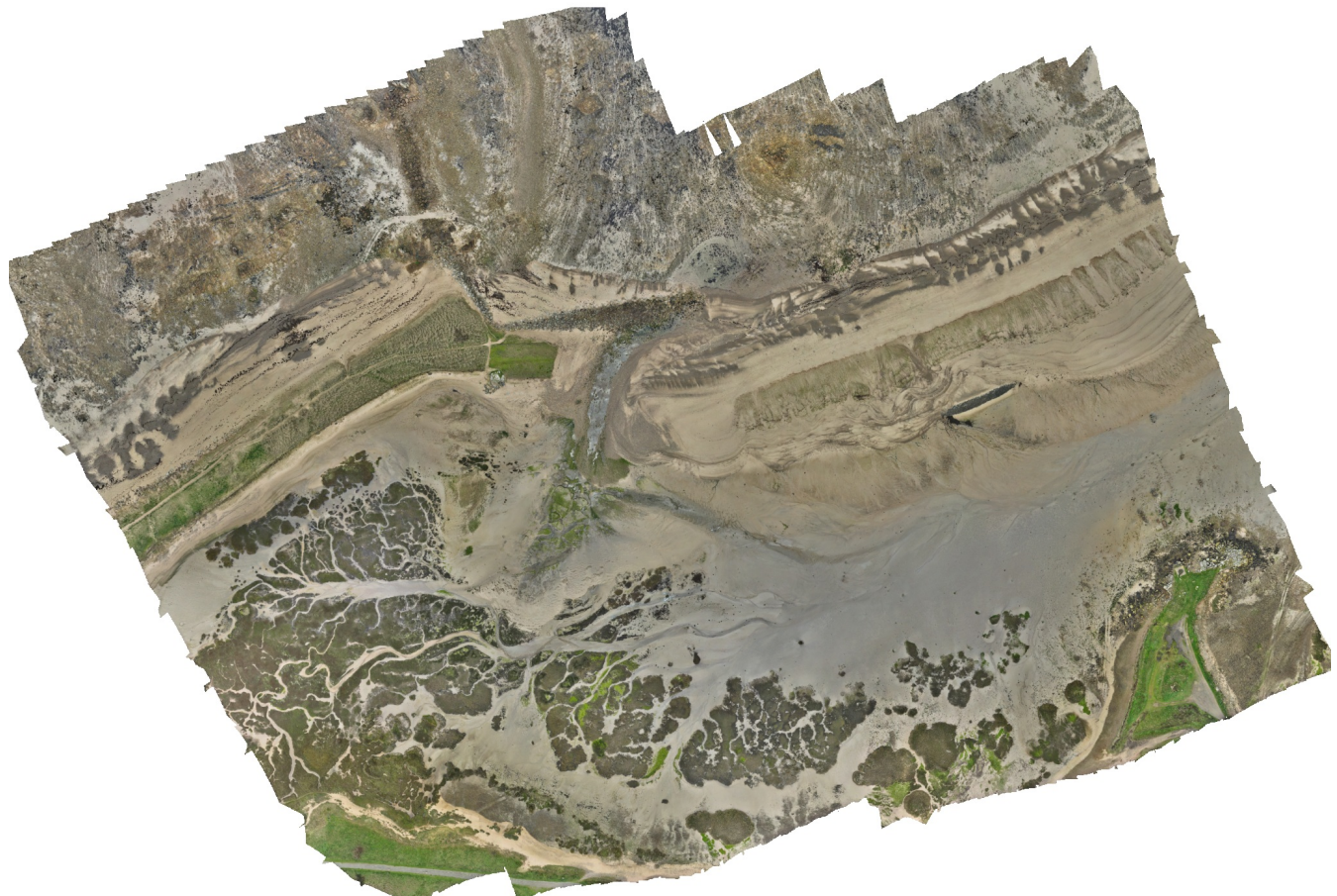
PARAMÈTRES DE GÉNÉRATION DES CARTES DE PROFONDEUR

| | |
|--|--|
| Qualité | Haute |
| Mode de filtrage | Agressif |
| Max voisins | 16 |
| Temps de traitement | 41 minutes 10 secondes |
| Utilisation de la mémoire | 5.64 GB |
| Paramètres de génération du nuage de points dense | |
| Temps de traitement | 1 heure 10 minutes |
| Utilisation de la mémoire | 9.05 GB |
| Date de création | 2023:12:19 14:55:11 |
| Version du programme | 1.8.5.15709 |
| Taille du fichier | 3.67 GB |
| MNE | |
| Taille | 20,684 x 16,804 |
| Système de coordonnées | RGF93 / Lambert-93 (EPSG::2154) |
| Paramètres de génération des cartes de profondeur | |
| Qualité | Haute |
| Mode de filtrage | Agressif |
| Max voisins | 16 |
| Temps de traitement | 41 minutes 10 secondes |
| Utilisation de la mémoire | 5.64 GB |
| Paramètres de reconstruction | |
| Données source | Cartes de profondeur |
| Interpolation | Activé |
| Temps de traitement | 51 minutes 10 secondes |
| Utilisation de la mémoire | 11.66 GB |
| Date de création | 2023:12:20 09:35:06 |
| Version du programme | 1.8.5.15709 |
| Taille du fichier | 1.10 GB |
| Orthomosaïque | |
| Taille | 41,368 x 33,608 |
| Système de coordonnées | RGF93 / Lambert-93 (EPSG::2154) |
| Couleurs | 3 bandes, uint8 |
| Paramètres de reconstruction | |
| Mode de fusion | Mosaïque |
| Surface | MNE |
| Activer le remplissage des trous | Oui |
| Activer le filtre fantôme | Non |
| Temps de traitement | 15 minutes 58 secondes |
| Utilisation de la mémoire | 1.69 GB |
| Date de création | 2023:12:20 09:53:21 |
| Version du programme | 1.8.5.15709 |
| Taille du fichier | 14.59 GB |
| Système | |
| Nom du programme | Agisoft Metashape Professional |
| Version du programme | 1.8.5 build 15709 |
| Système d'exploitation | Windows 64 bit |
| RAM | 31.72 GB |
| CPU | Intel(R) Xeon(R) W-1250P CPU @ 4.10GHz |
| GPU(s) | NVIDIA GeForce RTX 2060 SUPER |

Sillon de Talbert - relevé du 20 février 2024

**Mavik3E + Base D-RTK 2 / GCPs relevés au DGPS TopCon Hyper V (Base+Mobile)
/ coordonnées Lambert 93 (EPSG 2154) / ref. altitudinal : m NGF**

02 April 2024



Données du levé

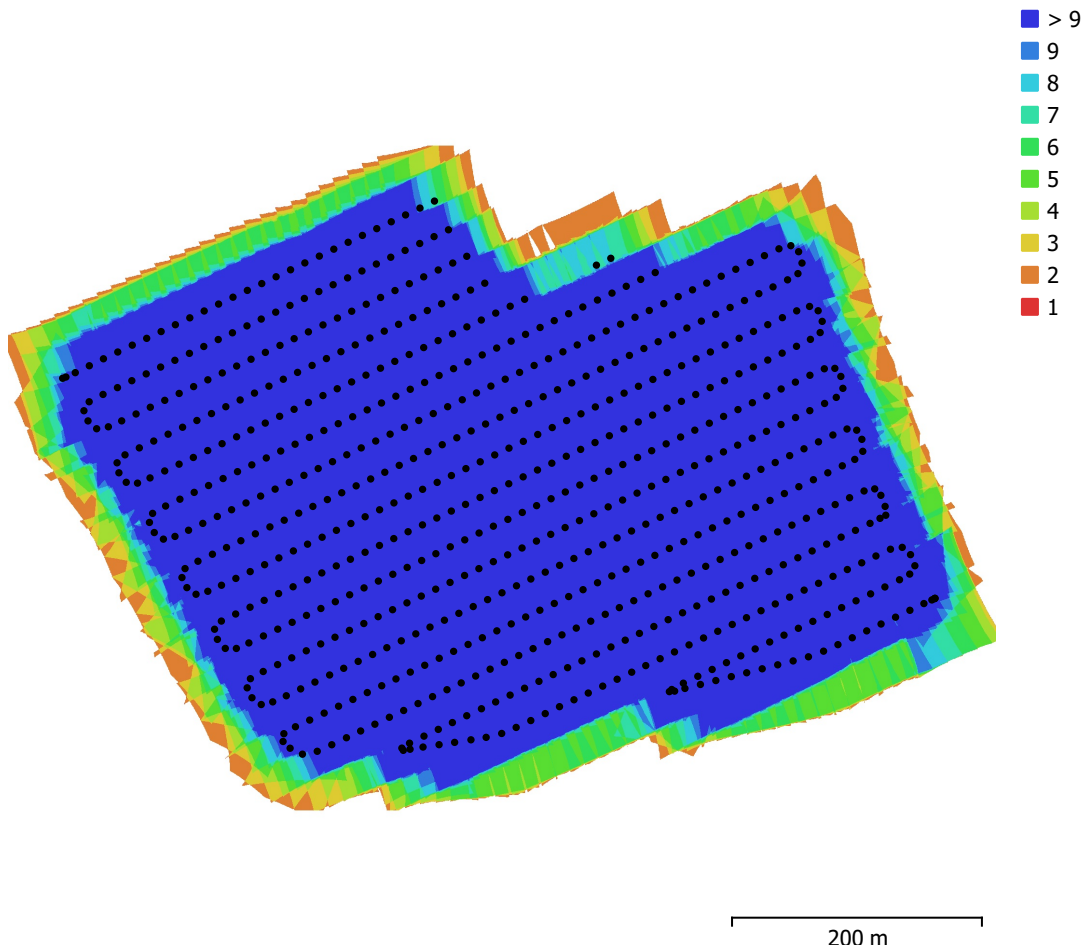


Fig. 1. Emplacements des caméras et chevauchement des images.

| | | | |
|---------------------|-----------------------|-------------------------|-----------|
| Nombre d'images: | 810 | Stations de caméras: | 700 |
| Altitude de vol: | 65.3 m | Points de liaison: | 288,329 |
| Résolution au sol: | 1.66 cm/px | Projections: | 2,568,086 |
| Zone de couverture: | 0.293 km ² | Erreur de reprojection: | 0.558 px |

| Modèle de caméra | Résolution | Longueur focale | Taille de pixel | Précalibré |
|------------------|-------------|-----------------|-----------------|------------|
| M3E (12.29mm) | 5280 x 3956 | 12.29 mm | 3.36 x 3.36 µm | Non |

Tableau 1. Caméras.

Calibration de la caméra

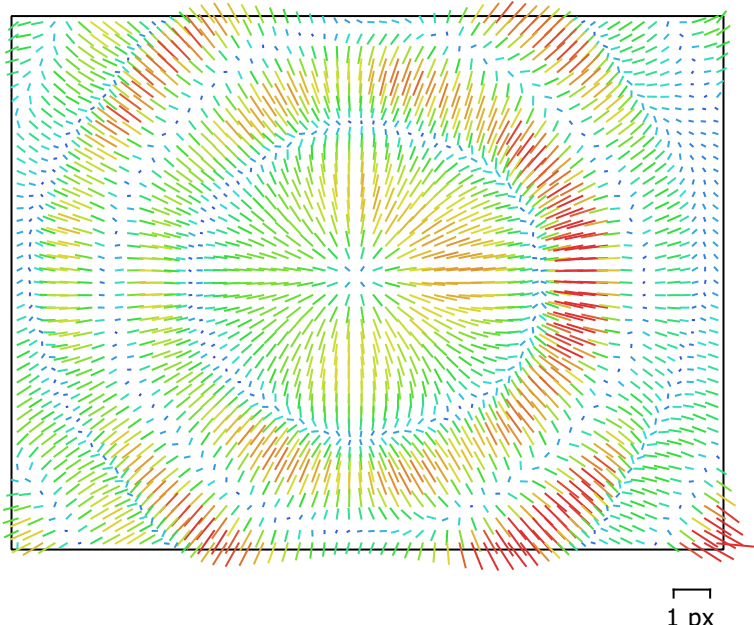


Fig. 2. Résiduelles des points de liaison pour M3E (12.29mm).

M3E (12.29mm)

810 images

| Type | Résolution | Longueur focale | Taille de pixel |
|-------|--------------------|-----------------|-----------------------|
| Cadre | 5280 x 3956 | 12.29 mm | 3.36 x 3.36 µm |

| | Valeur | Erreur | F | Cx | Cy | K1 | K2 | K3 | P1 | P2 |
|-----------|---------------------|---------|------|------|------|-------|-------|-------|-------|-------|
| F | 3740.84 | 0.55 | 1.00 | 0.49 | 0.33 | -0.97 | 0.28 | -0.79 | -0.49 | -0.33 |
| Cx | -2.47014 | 0.03 | | 1.00 | 0.15 | -0.48 | 0.15 | -0.40 | -0.91 | -0.16 |
| Cy | -19.3867 | 0.026 | | | 1.00 | -0.32 | 0.08 | -0.25 | -0.16 | -0.89 |
| K1 | -0.113188 | 3.5e-05 | | | | 1.00 | -0.50 | 0.90 | 0.49 | 0.32 |
| K2 | 0.0109696 | 2.3e-05 | | | | | 1.00 | -0.80 | -0.18 | -0.09 |
| K3 | -0.0247128 | 2.7e-05 | | | | | | 1.00 | 0.41 | 0.26 |
| P1 | -0.000146523 | 1.1e-06 | | | | | | | 1.00 | 0.16 |
| P2 | -4.22142e-05 | 9.2e-07 | | | | | | | | 1.00 |

Tableau 2. Coefficients de calibration et matrice de corrélation.

Positions de caméra

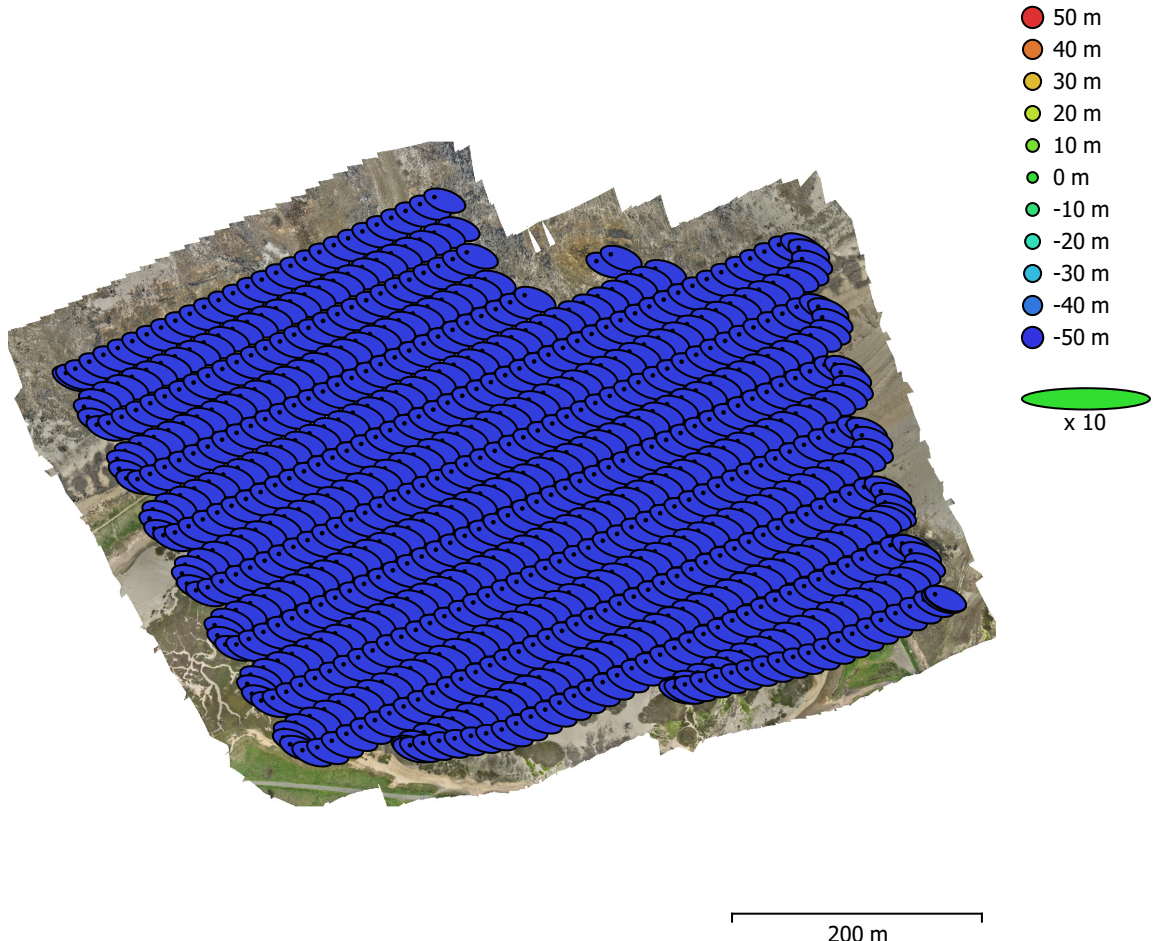


Fig. 3. Emplacements de la caméra et estimations d'erreur.

L'erreur Z est représentée par la couleur de l'ellipse. Les erreurs X et Y sont représentées par la forme de l'ellipse. Les emplacements estimés des caméras sont identifiés par un point noir.

| Erreur X (m) | Erreur Y (m) | Erreur Z (m) | Erreur XY (m) | Erreur totale (m) |
|--------------|--------------|--------------|---------------|-------------------|
| 1.6809 | 0.642546 | 48.4136 | 1.79952 | 48.4471 |

Tableau 3. Erreur moyenne d'emplacement de la caméra.

X - Est, Y - Nord, Z - Altitude.

Points de contrôle au sol

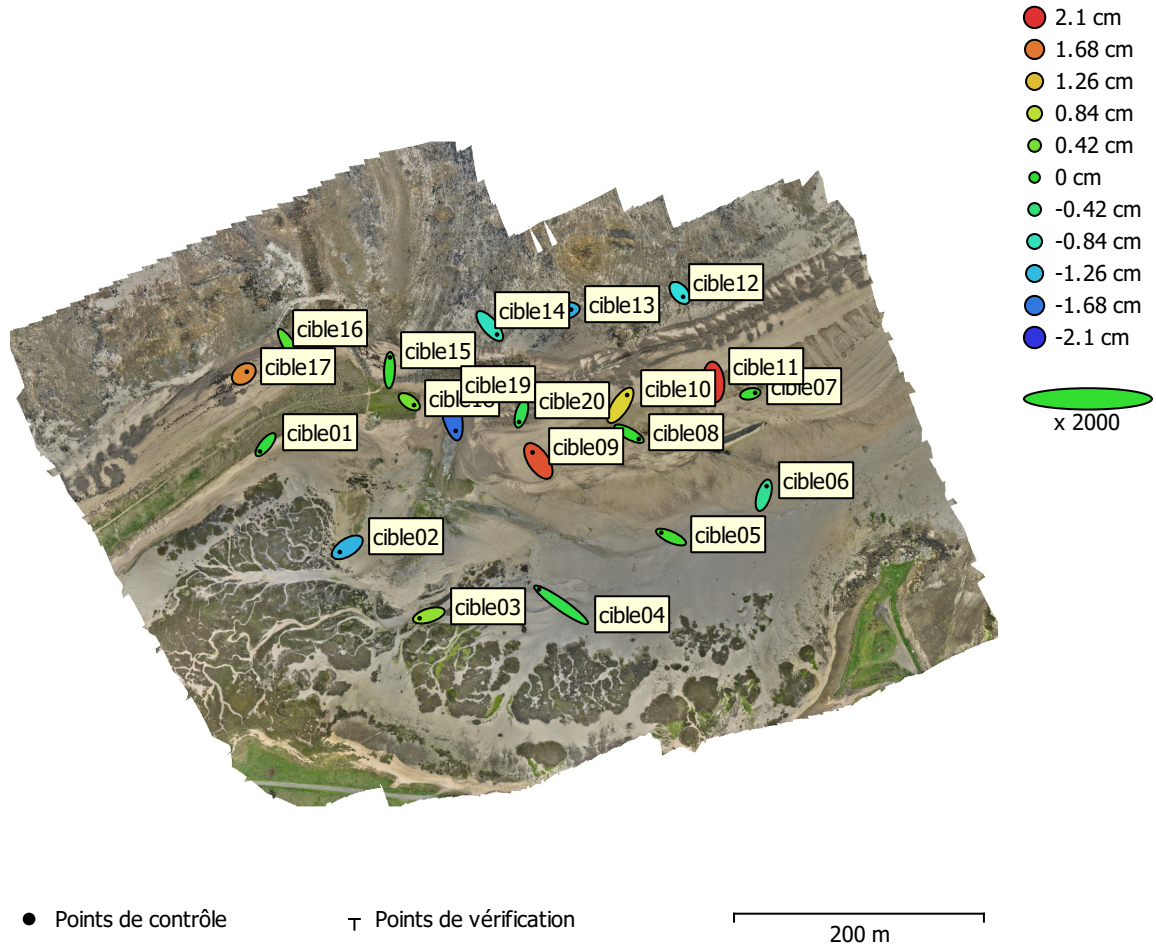


Fig. 4. Emplacements des points de contrôle au sol et estimations d'erreur.

L'erreur Z est représentée par la couleur de l'ellipse. Les erreurs X et Y sont représentées par la forme de l'ellipse. Les emplacements estimés des points de contrôle au sol sont marqués d'un point ou d'une croix.

| Nombre | Erreur X (cm) | Erreur Y (cm) | Erreur Z (cm) | Erreur XY (cm) | Total (cm) |
|--------|---------------|---------------|---------------|----------------|------------|
| 20 | 0.622273 | 0.717156 | 1.02113 | 0.949493 | 1.39436 |

Tableau 4. Points de contrôle RMSE.

X - Est, Y - Nord, Z - Altitude.

| Etiquette | Erreur X (cm) | Erreur Y (cm) | Erreur Z (cm) | Total (cm) | Image (px) |
|------------------|----------------------|----------------------|----------------------|-------------------|-------------------|
| cible01 | -0.449125 | -0.541262 | -0.0683094 | 0.706642 | 0.429 (17) |
| cible02 | -0.597078 | -0.378596 | -1.31644 | 1.49427 | 0.471 (22) |
| cible04 | -1.76734 | 1.2412 | -0.142716 | 2.16436 | 0.278 (22) |
| cible03 | -0.737418 | -0.227293 | 0.587775 | 0.970014 | 0.142 (23) |
| cible05 | -0.777307 | 0.352723 | 0.0893888 | 0.85826 | 0.254 (23) |
| cible06 | 0.229647 | 0.72771 | -0.585423 | 0.96178 | 0.392 (22) |
| cible07 | 0.383985 | 0.0801965 | 0.0664781 | 0.397864 | 0.506 (14) |
| cible08 | 0.776878 | -0.421681 | 0.0433601 | 0.885005 | 0.358 (22) |
| cible09 | -0.461651 | 0.68196 | 1.90581 | 2.07612 | 0.477 (21) |
| cible10 | 0.545858 | 0.826915 | 1.11484 | 1.49152 | 0.428 (16) |
| cible11 | -0.0725435 | 0.785688 | 2.04941 | 2.19605 | 0.346 (22) |
| cible12 | 0.261634 | -0.304874 | -1.01897 | 1.09531 | 0.546 (16) |
| cible13 | 0.673824 | 0.137458 | -1.34627 | 1.51174 | 0.404 (15) |
| cible14 | 0.58134 | -0.680819 | -0.838471 | 1.22658 | 0.209 (21) |
| cible15 | 0.0396447 | 1.02184 | 0.035295 | 1.02322 | 0.160 (20) |
| cible16 | 0.601589 | -0.986308 | 0.225952 | 1.17719 | 0.458 (20) |
| cible17 | 0.241819 | 0.182412 | 1.57854 | 1.60734 | 0.467 (21) |
| cible18 | 0.381323 | -0.264268 | 0.407055 | 0.617202 | 0.299 (21) |
| cible19 | 0.362571 | -1.59096 | -1.73585 | 2.38239 | 0.597 (12) |
| cible20 | -0.188231 | -0.653261 | -0.204215 | 0.709848 | 0.304 (17) |
| Total | 0.622273 | 0.717156 | 1.02113 | 1.39436 | 0.384 |

Tableau 5. Points de contrôle.

X - Est, Y - Nord, Z - Altitude.

Modèle Numérique d'élévation

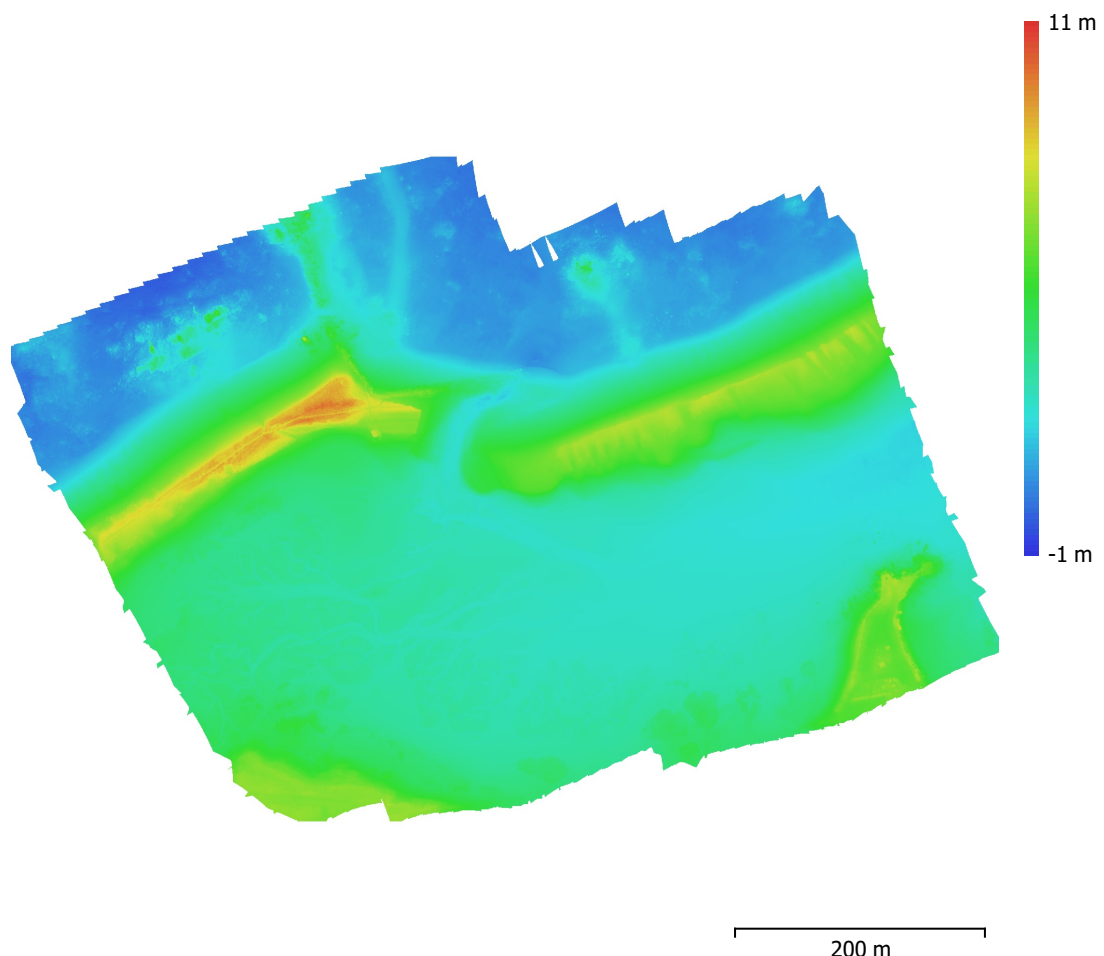


Fig. 5. Modèle numérique d'élévation reconstruit.

Résolution: 3.32 cm/px

Densité des points: 907 points/m²

Paramètres de traitement

Général

| | |
|------------------------|---------------------------------|
| Caméras | 810 |
| Caméras alignées | 700 |
| Repères | 20 |
| Système de coordonnées | RGF93 / Lambert-93 (EPSG::2154) |
| Angles de rotation | Lacet, Tangage, Roulis |

NUAGE DE POINT

| | |
|--|------------------------|
| Points | 288,329 de 968,732 |
| Erreur RMS de reprojection | 0.192052 (0.557509 px) |
| Erreur Max de reprojection | 0.713072 (5.05134 px) |
| Taille moyenne de point | 3.09792 px |
| Couleurs des points | 3 bandes, uint8 |
| Points-clé | Non |
| Multiplicité moyenne des points de liaison | 8.80413 |

PARAMÈTRES D'ALIGNEMENT

| | |
|--|------------------------|
| Précision | La plus haute |
| Préélection générique | Oui |
| Préélection par références | Non |
| Limite de points | 40,000 |
| Limite de points-clé par Mpx | 60,000 |
| Limite de points de liaison | 10,000 |
| Exclure les points de liaison fixes | Oui |
| Correspondance d'images guidée | Non |
| Ajustement progressif du modèle de la caméra | Non |
| Temps de concordance | 23 minutes 1 seconde |
| Utilisation de la mémoire de correspondance | 1.51 GB |
| Temps d'alignement | 44 minutes 15 secondes |
| Utilisation de la mémoire d'alignement | 2.12 GB |

PARAMÈTRES D'OPTIMISATION

| | |
|--|--------------------------|
| Paramètres | f, cx, cy, k1-k3, p1, p2 |
| Ajustement progressif du modèle de la caméra | Non |
| Durée d'optimisation | 32 secondes |
| Date de création | 2024:04:02 09:52:50 |
| Version du programme | 1.8.5.15709 |
| Taille du fichier | 139.62 MB |

CARTES DE PROFONDEUR

| | |
|--------|-----|
| Nombre | 700 |
|--------|-----|

PARAMÈTRES DE GÉNÉRATION DES CARTES DE PROFONDEUR

| | |
|---------------------------|-----------------------|
| Qualité | Haute |
| Mode de filtrage | Modéré |
| Max voisins | 16 |
| Temps de traitement | 35 minutes 2 secondes |
| Utilisation de la mémoire | 13.50 GB |
| Date de création | 2024:04:02 12:45:26 |
| Version du programme | 1.8.5.15709 |
| Taille du fichier | 5.64 GB |

NUAGE DE POINTS DENSE

| | |
|---------------------|-------------|
| Points | 282,775,917 |
| Couleurs des points | Aucun |

PARAMÈTRES DE GÉNÉRATION DES CARTES DE PROFONDEUR

| | |
|---------------------------|-----------------------|
| Qualité | Haute |
| Mode de filtrage | Modéré |
| Max voisins | 16 |
| Temps de traitement | 35 minutes 2 secondes |
| Utilisation de la mémoire | 13.50 GB |

Paramètres de génération du nuage de points dense

| | |
|---------------------------|-----------------------|
| Temps de traitement | 39 minutes 8 secondes |
| Utilisation de la mémoire | 10.63 GB |
| Date de création | 2024:04:02 13:24:38 |
| Version du programme | 1.8.5.15709 |
| Taille du fichier | 2.58 GB |

MNE

| | |
|------------------------|---------------------------------|
| Taille | 23,795 x 16,009 |
| Système de coordonnées | RGF93 / Lambert-93 (EPSG::2154) |

Paramètres de reconstruction

| | |
|---------------------------|----------------------|
| Données source | NUAGE dense |
| Interpolation | Activé |
| Temps de traitement | 3 minutes 2 secondes |
| Utilisation de la mémoire | 342.89 MB |
| Date de création | 2024:04:02 13:27:44 |
| Version du programme | 1.8.5.15709 |
| Taille du fichier | 1.17 GB |

Orthomosaïque

| | |
|------------------------|---------------------------------|
| Taille | 47,590 x 32,018 |
| Système de coordonnées | RGF93 / Lambert-93 (EPSG::2154) |
| Couleurs | 3 bandes, uint8 |

Paramètres de reconstruction

| | |
|----------------------------------|-----------------------|
| Mode de fusion | Mosaïque |
| Surface | MNE |
| Activer le remplissage des trous | Oui |
| Activer le filtre fantôme | Non |
| Temps de traitement | 20 minutes 2 secondes |
| Utilisation de la mémoire | 2.58 GB |
| Date de création | 2024:04:02 13:36:30 |
| Version du programme | 1.8.5.15709 |
| Taille du fichier | 15.91 GB |

Système

| | |
|------------------------|--|
| Nom du programme | Agisoft Metashape Professional |
| Version du programme | 1.8.5 build 15709 |
| Système d'exploitation | Windows 64 bit |
| RAM | 15.82 GB |
| CPU | Intel(R) Core(TM) i7-8665U CPU @ 1.90GHz |
| GPU(s) | Aucun |

Sillon de Talbert - 18 septembre 2024

**Mavik3E + Base D-RTK 2 / GCPs relevés au DGPS TopCon Hyper V (Base+Mobile)
/ coordonnées L93 (EPSG:2154) / ref. altitudinal : m NGF**

21 September 2024



Données du levé

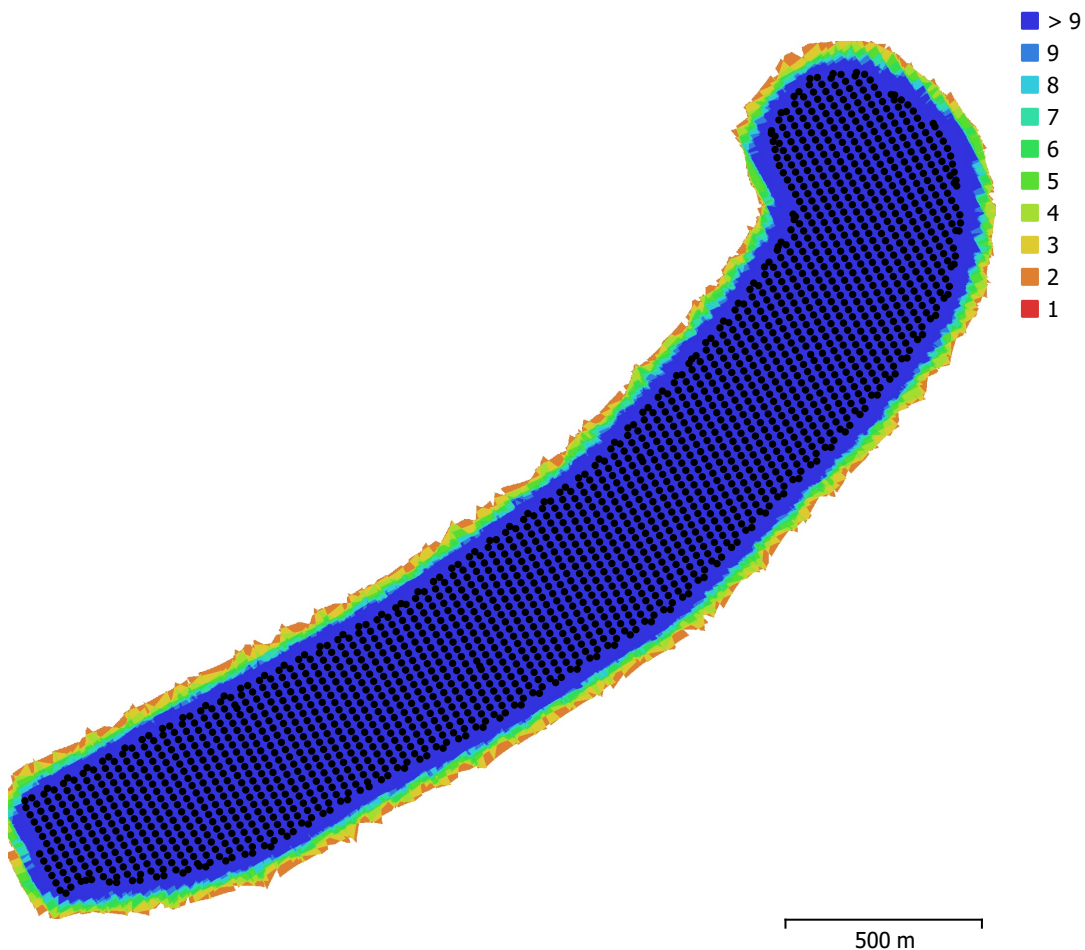


Fig. 1. Emplacements des caméras et chevauchement des images.

| | | | |
|---------------------|----------------------|-------------------------|------------|
| Nombre d'images: | 2,171 | Stations de caméras: | 2,171 |
| Altitude de vol: | 113 m | Points de liaison: | 759,435 |
| Résolution au sol: | 2.85 cm/px | Projections: | 13,543,930 |
| Zone de couverture: | 1.76 km ² | Erreur de reprojection: | 0.76 px |

| Modèle de caméra | Résolution | Longueur focale | Taille de pixel | Précalibré |
|------------------|-------------|-----------------|-----------------|------------|
| M3E (12.29mm) | 5280 x 3956 | 12.29 mm | 3.36 x 3.36 µm | Non |

Tableau 1. Caméras.

Calibration de la caméra

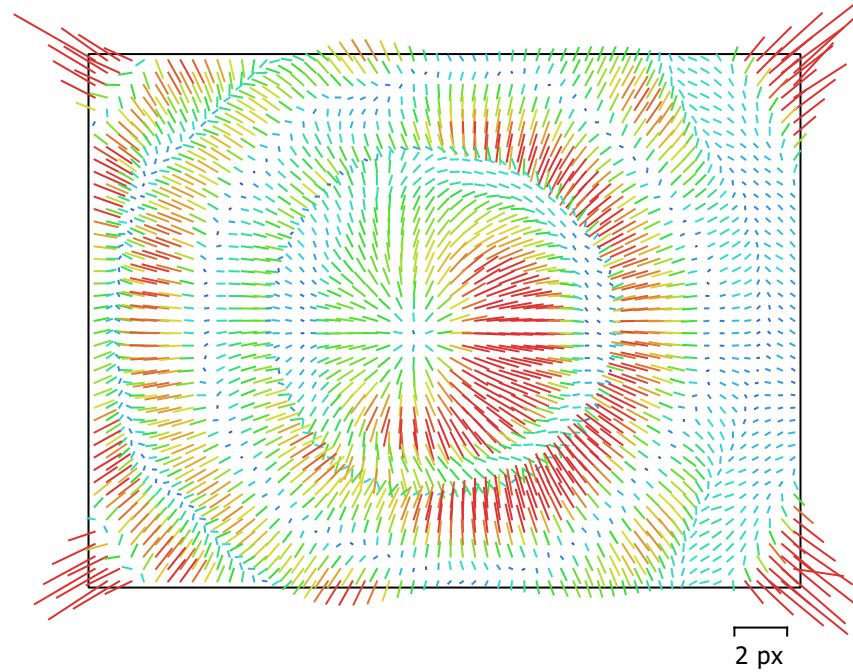


Fig. 2. Résiduelles des points de liaison pour M3E (12.29mm).

M3E (12.29mm)

2171 images

| Type | Résolution | Longueur focale | Taille de pixel |
|-------|--------------------|-----------------|-----------------------|
| Cadre | 5280 x 3956 | 12.29 mm | 3.36 x 3.36 µm |

| | Valeur | Erreur | F | Cx | Cy | K1 | K2 | K3 | P1 | P2 |
|-----------|--------------------|---------|------|------|-------|-------|-------|-------|-------|-------|
| F | 3807.48 | 0.28 | 1.00 | 0.02 | -0.89 | -0.96 | -0.07 | -0.54 | 0.04 | 0.89 |
| Cx | 1.07569 | 0.012 | | 1.00 | -0.00 | -0.01 | -0.06 | 0.05 | -0.82 | 0.00 |
| Cy | -24.9203 | 0.027 | | | 1.00 | 0.85 | 0.07 | 0.47 | -0.06 | -0.97 |
| K1 | -0.111392 | 1.7e-05 | | | | 1.00 | -0.21 | 0.74 | -0.04 | -0.85 |
| K2 | -0.00187606 | 1.4e-05 | | | | | 1.00 | -0.79 | 0.00 | -0.06 |
| K3 | -0.0171128 | 1.3e-05 | | | | | | 1.00 | -0.03 | -0.48 |
| P1 | 0.000312752 | 4.5e-07 | | | | | | | 1.00 | 0.06 |
| P2 | 0.000411139 | 9.4e-07 | | | | | | | | 1.00 |

Tableau 2. Coefficients de calibration et matrice de corrélation.

Points de contrôle au sol

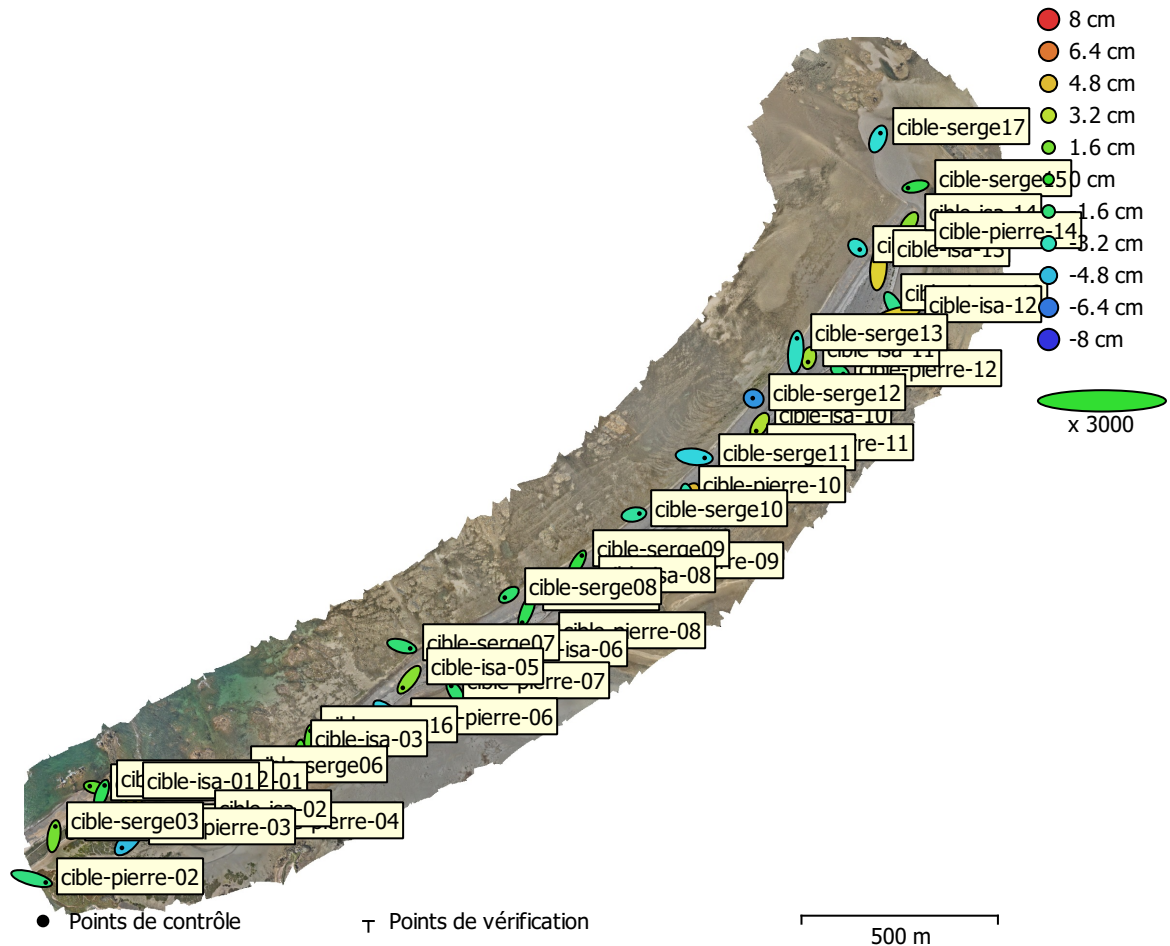


Fig. 3. Emplacements des points de contrôle au sol et estimations d'erreur.

L'erreur Z est représentée par la couleur de l'ellipse. Les erreurs X et Y sont représentées par la forme de l'ellipse. Les emplacements estimés des points de contrôle au sol sont marqués d'un point ou d'une croix.

| Nombre | Erreur X (cm) | Erreur Y (cm) | Erreur Z (cm) | Erreur XY (cm) | Total (cm) |
|--------|---------------|---------------|---------------|----------------|------------|
| 42 | 1.05712 | 1.17841 | 3.04246 | 1.58309 | 3.42968 |

Tableau 3. Points de contrôle RMSE.

X - Est, Y - Nord, Z - Altitude.

| Etiquette | Erreur X (cm) | Erreur Y (cm) | Erreur Z (cm) | Total (cm) | Image (px) |
|------------------|----------------------|----------------------|----------------------|-------------------|-------------------|
| cible-serge... | 0.407855 | 0.994811 | -3.76554 | 3.91603 | 1.355 (30) |
| cible-serge... | -1.26259 | -0.247382 | -0.654144 | 1.44334 | 0.627 (33) |
| cible-serge... | 0.365 | -0.304293 | -3.5591 | 3.59068 | 1.034 (32) |
| cible-isa-13 | 0.197548 | 2.29637 | 4.29183 | 4.87156 | 1.241 (33) |
| cible-isa-14 | -0.630485 | -0.968638 | 2.07597 | 2.37601 | 0.761 (32) |
| cible-pierr... | 0.907274 | -0.487365 | 0.103621 | 1.03509 | 0.659 (34) |
| cible-pierr... | 0.752279 | -1.26469 | -2.12139 | 2.58179 | 1.101 (36) |
| cible-isa-12 | -3.14684 | -1.04801 | 4.39156 | 5.50334 | 1.032 (28) |
| cible-pierr... | 0.552517 | -0.396221 | -1.66498 | 1.79845 | 0.549 (35) |
| cible-isa-11 | -0.150986 | -0.681964 | 2.6018 | 2.69393 | 0.660 (25) |
| cible-serge... | 0.202097 | 2.33196 | -3.43048 | 4.15296 | 0.812 (35) |
| cible-isa-10 | -0.580277 | -0.962268 | 2.90201 | 3.11197 | 1.143 (30) |
| cible-pierr... | 0.118426 | 0.717358 | -4.40691 | 4.46648 | 1.223 (30) |
| cible-serge... | -0.152753 | 0.0569928 | -5.72025 | 5.72257 | 1.519 (33) |
| cible-serge... | 1.76935 | -0.197422 | -4.19154 | 4.55397 | 0.750 (36) |
| cible-isa-09 | -0.567298 | -0.995521 | 4.86771 | 5.00075 | 1.223 (26) |
| cible-pierr... | 0.243785 | -1.83642 | -2.82916 | 3.38171 | 0.801 (31) |
| cible-serge... | 0.92535 | 0.163247 | -2.48738 | 2.65894 | 0.997 (32) |
| cible-pierr... | 1.17616 | -0.314069 | 1.7258 | 2.11196 | 0.610 (33) |
| cible-serge... | 0.795644 | 1.36907 | -0.353468 | 1.62245 | 0.368 (36) |
| cible-isa-08 | -0.282601 | 0.976317 | 7.53758 | 7.6058 | 1.437 (31) |
| cible-pierr... | -0.00337389 | 1.11457 | -2.7111 | 2.93126 | 0.988 (31) |
| cible-isa-07 | -0.81383 | -2.09415 | -0.836531 | 2.39741 | 0.959 (27) |
| cible-serge... | -0.692288 | -0.462291 | -1.34744 | 1.58384 | 0.678 (35) |
| cible-isa-06 | -1.71347 | 0.716096 | 3.85941 | 4.28297 | 0.812 (35) |
| cible-pierr... | -0.719312 | 1.14789 | -1.4202 | 1.96266 | 0.489 (34) |
| cible-serge... | 1.42444 | -0.395033 | -1.56502 | 2.15275 | 0.797 (30) |
| cible-isa-05 | -1.06723 | -1.36753 | 1.97753 | 2.63054 | 0.867 (34) |
| cible-pierr... | 1.4081 | -1.31979 | -4.26693 | 4.68308 | 0.796 (34) |
| cible-serge... | 0.0647878 | 2.59482 | 0.97462 | 2.77257 | 0.484 (36) |
| cible-isa-03 | -0.183228 | -1.81076 | 0.698364 | 1.9494 | 0.765 (28) |

| Etiquette | Erreur X (cm) | Erreur Y (cm) | Erreur Z (cm) | Total (cm) | Image (px) |
|------------------|----------------------|----------------------|----------------------|-------------------|-------------------|
| cible-pierr... | 0.487014 | -0.284913 | -3.07567 | 3.12699 | 0.771 (32) |
| cible-serge... | -0.226564 | 1.01294 | 0.560304 | 1.17954 | 1.063 (32) |
| cible-chou... | 1.03692 | 1.14342 | 1.47557 | 2.1354 | 1.187 (32) |
| cible-serge... | -0.794127 | 0.181052 | 1.05718 | 1.33456 | 0.532 (29) |
| cible-chou... | 0.519096 | 1.41929 | -0.873314 | 1.74543 | 0.836 (31) |
| cible-pierr... | -0.135251 | -0.349947 | 1.08657 | 1.14952 | 0.350 (24) |
| cible-isa-01 | 0.434769 | -1.40043 | 4.57786 | 4.80698 | 1.029 (30) |
| cible-isa-02 | -2.60441 | -0.649541 | 0.672708 | 2.7672 | 0.914 (32) |
| cible-pierr... | -1.16179 | -1.26175 | -4.7974 | 5.09478 | 1.025 (35) |
| cible-pierr... | 2.37907 | -0.66509 | -1.78626 | 3.04845 | 1.853 (6) |
| cible-serge... | 0.242524 | 1.64941 | 1.52273 | 2.25789 | 0.883 (16) |
| Total | 1.05712 | 1.17841 | 3.04246 | 3.42968 | 0.927 |

Tableau 4. Points de contrôle.

X - Est, Y - Nord, Z - Altitude.

Modèle Numérique d'élévation

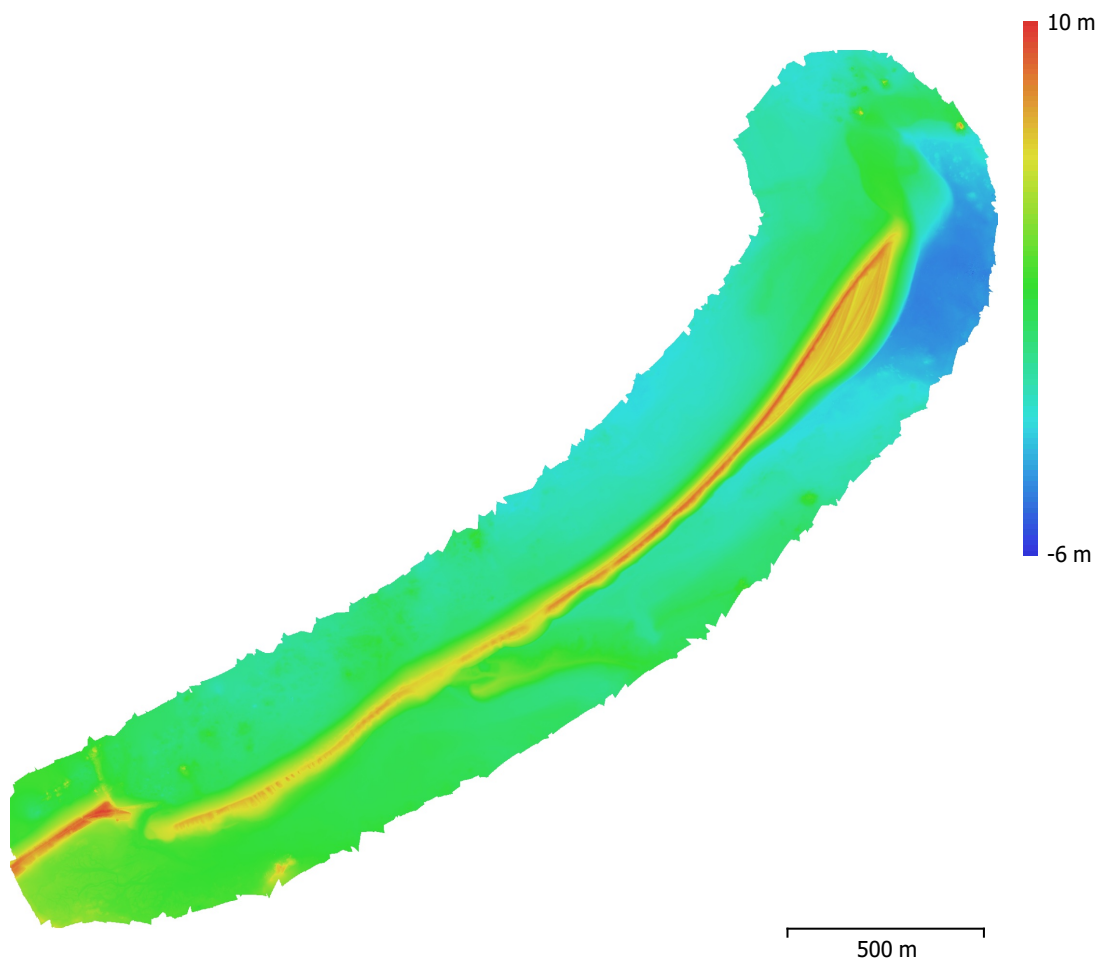


Fig. 4. Modèle numérique d'élévation reconstruit.

Résolution: 5.69 cm/px

Densité des points: 309 points/m²

Paramètres de traitement

Général

| | |
|------------------------|---------------------------------|
| Caméras | 2171 |
| Caméras alignées | 2171 |
| Repères | 42 |
| Système de coordonnées | RGF93 / Lambert-93 (EPSG::2154) |
| Angles de rotation | Lacet, Tangage, Roulis |

NUAGE DE POINT

| | |
|--|------------------------|
| Points | 759,435 de 1,570,270 |
| Erreur RMS de reprojection | 0.311078 (0.760425 px) |
| Erreur Max de reprojection | 1.48913 (8.99367 px) |
| Taille moyenne de point | 2.55334 px |
| Couleurs des points | 3 bandes, uint8 |
| Points-clé | Non |
| Multiplicité moyenne des points de liaison | 14.8141 |

PARAMÈTRES D'ALIGNEMENT

| | |
|--|------------------------|
| Précision | Haute |
| Présélection générique | Oui |
| Présélection par références | Non |
| Limite de points | 60,000 |
| Limite de points-clé par Mpx | 60,000 |
| Limite de points de liaison | 10,000 |
| Exclure les points de liaison fixes | Non |
| Correspondance d'images guidée | Non |
| Ajustement progressif du modèle de la caméra | Non |
| Temps de concordance | 1 heure 30 minutes |
| Utilisation de la mémoire de correspondance | 3.36 GB |
| Temps d'alignement | 39 minutes 12 secondes |
| Utilisation de la mémoire d'alignement | 1.87 GB |

PARAMÈTRES D'OPTIMISATION

| | |
|--|--------------------------|
| Paramètres | f, cx, cy, k1-k3, p1, p2 |
| Ajustement progressif du modèle de la caméra | Non |
| Durée d'optimisation | 2 minutes 6 secondes |
| Date de création | 2024:09:20 14:20:04 |
| Version du programme | 1.8.5.15709 |
| Taille du fichier | 377.11 MB |

CARTES DE PROFONDEUR

| | |
|--------|------|
| Nombre | 2167 |
|--------|------|

PARAMÈTRES DE GÉNÉRATION DES CARTES DE PROFONDEUR

| | |
|---------------------------|---------------------|
| Qualité | Haute |
| Mode de filtrage | Modéré |
| Max voisins | 16 |
| Temps de traitement | 2 heures 23 minutes |
| Utilisation de la mémoire | 11.09 GB |
| Date de création | 2024:09:21 01:02:39 |
| Version du programme | 1.8.5.15709 |
| Taille du fichier | 16.28 GB |

NUAGE DE POINTS DENSE

| | |
|---------------------|-------------|
| Points | 510,486,224 |
| Couleurs des points | Aucun |

PARAMÈTRES DE GÉNÉRATION DES CARTES DE PROFONDEUR

| | |
|---------------------------|---------------------|
| Qualité | Haute |
| Mode de filtrage | Modéré |
| Max voisins | 16 |
| Temps de traitement | 2 heures 23 minutes |
| Utilisation de la mémoire | 11.09 GB |

Paramètres de génération du nuage de points dense

| | |
|---------------------------|---------------------|
| Temps de traitement | 2 heures 41 minutes |
| Utilisation de la mémoire | 13.94 GB |
| Date de création | 2024:09:21 03:43:59 |
| Version du programme | 1.8.5.15709 |
| Taille du fichier | 4.58 GB |

MNE

| | |
|------------------------|---------------------------------|
| Taille | 44,138 x 39,223 |
| Système de coordonnées | RGF93 / Lambert-93 (EPSG::2154) |

Paramètres de reconstruction

| | |
|---------------------------|-----------------------|
| Données source | NUAGE dense |
| Interpolation | Activé |
| Temps de traitement | 8 minutes 15 secondes |
| Utilisation de la mémoire | 337.81 MB |
| Date de création | 2024:09:21 03:52:19 |
| Version du programme | 1.8.5.15709 |
| Taille du fichier | 2.53 GB |

Orthomosaïque

| | |
|------------------------|---------------------------------|
| Taille | 25,120 x 22,323 |
| Système de coordonnées | RGF93 / Lambert-93 (EPSG::2154) |
| Couleurs | 3 bandes, uint8 |

Paramètres de reconstruction

| | |
|----------------------------------|------------------------|
| Mode de fusion | Mosaïque |
| Surface | MNE |
| Activer le remplissage des trous | Oui |
| Activer le filtre fantôme | Non |
| Temps de traitement | 22 minutes 46 secondes |
| Utilisation de la mémoire | 2.01 GB |
| Date de création | 2024:09:21 04:07:37 |
| Version du programme | 1.8.5.15709 |
| Taille du fichier | 7.95 GB |

Système

| | |
|------------------------|--|
| Nom du programme | Agisoft Metashape Professional |
| Version du programme | 1.8.5 build 15709 |
| Système d'exploitation | Windows 64 bit |
| RAM | 15.82 GB |
| CPU | Intel(R) Core(TM) i7-8665U CPU @ 1.90GHz |
| GPU(s) | Aucun |

Annexe 2

Article scientifique paru dans la revue *Géomorphology* en juin 2024.



Breaching of the Sillon de Talbert gravel spit (North Brittany, France) and coastal flooding risk assessment

Pierre Stéphan^a, Serge Suanez^{b,*}, Thomas Guérin^c, Aurélie Rivier^d, Laurent Leballeur^d, Benoit Waeles^c, Jérôme Ammann^e, Julien Houron^f

^a CNRS, Univ Brest, UMR LETG 6554, Institut Universitaire Européen de la Mer, F-29280 Plouzané, France

^b Univ Brest, CNRS, UMR LETG 6554, Institut Universitaire Européen de la Mer, F-29280 Plouzané, France

^c Waeles Marine Consultants, 53 rue du commandant Graix, 29200 Brest, France

^d Actimar SAS, 36, quai de la Douane, 29200 Brest, France

^e CNRS, Univ Brest, UMR LGO 6538, Institut Universitaire Européen de la Mer, Plouzané, France

^f Réserve Naturelle Régionale du Sillon de Talbert, 22610 Pleubian, France

ARTICLE INFO

Keywords:

Gravel spit
Breach
Flooding risk
Modelling
Coastal management, Brittany

ABSTRACT

Coastal barriers are a natural defence against the marine submersion of low-lying back-barrier areas. In March 2018, a breach opened up in the proximal section of the Sillon de Talbert spit barrier (North Brittany, France), causing great concern among local residents and elected representatives. A study to assess the risk of submersion of the low-lying areas of the Laneros Peninsula, located behind the barrier, was carried out in 2020. Hydrodynamic conditions (waves, currents, and water levels) were modeled using Telemac-2D coupled with the phase-averaged wave model TOMAWAC. Simulations were compiled for the storm of February 1, 2014, corresponding to the most morphogenic event to occur in the last two decades. Five topomorphological configurations were considered for the numerical simulations: configurations #1 and #2 correspond to the ante-breach and post-breach morphological settings, while configurations #3, #4, and #5 correspond to hypothetical scenarios, from the enlargement of the breach (from 300 to 500 m width), to complete crest lowering of the barrier after a complete removing of the crest due to catastrophic overwash events. The results show that the breach accelerates the draining of the back-barrier sandflat, thereby reducing the height of extreme water levels at the coastline. This is mainly due to different tidal impacts on either side of the barrier, with a higher water level and the tidal peak occurring 15 min later and on the back-barrier than on the ocean-side zone. As a result, ebb currents begin to flow before the high tide level is reached, inducing a significant draining with a lowering of the extreme water level at the back-barrier zone. However, these simulations do not take into account the effects of climate change over the coming years, in particular the future rise in sea level and/or the acceleration of erosion processes already underway.

1. Introduction

Coastal barriers provide an effective coastal defence for the low-lying back-barrier areas (Schoonees et al., 1998; Hartley and Pontee, 2008; Pye and Blott, 2009; Dornbusch, 2017). Therefore, they act as natural coastal protection feature since they may significantly dissipate energetic storm wave energy related to overwash and flooding hazards (Plomaritis et al., 2018; Pollard et al., 2021). Coastal barriers (including barrier-spits and barrier-islands) are widely spread along the world's

coastline. While they are mainly composed of sand, a few proportion of gravel-dominated barriers are concentrated in formerly glaciated areas in mid- and upper-latitudes (Forbes et al., 1995; Orford et al., 1995, 2002). Due to the steep beach sea-face related to the coarse sediments composing these coastal landforms, gravel barrier morphodynamics are mainly dominated by highly reflective processes (Carter and Orford, 1984; Jennings and Shulmeister, 2002; Buscombe and Masselink, 2006), and occasionally by infragravity waves (Bertin et al., 2018; Billson et al., 2019). Therefore, during storm wave conditions, energetic swash

* Corresponding author.

E-mail addresses: pierre.stephan@univ-brest.fr (P. Stéphan), serge.suanez@univ-brest.fr (S. Suanez), thomas.guerin@bw-cgc.fr (T. Guérin), aurelie.rivier@actimar.fr (A. Rivier), Laurent.leballeur@shom.fr (L. Leballeur), benoit.waeles@bw-cgc.fr (B. Waeles), Jerome.Ammann@univ-brest.fr (J. Ammann), garde.littoral@mairie-pleubian.fr (J. Houron).

motions generated by waves breaking close to -and/or on- the lower beach face induce frequent overtopping/overwashing of the barrier crest (Carter and Orford, 1981; Poate et al., 2013; Almeida et al., 2015).

For swash-aligned barriers, overtopping to overwashing processes affecting gravel barriers mainly occur during extreme storm conditions. However, according to the storm-impact scaling model of Orford and Carter (1982), the morphological responses of the barriers to storm impact are ranged into four distinct regimes: (i) *swash overtopping* inducing crest raising, (ii) *discrete overwash* inducing crest lowering, (iii) *sluicing overwash* inducing barrier landward migration through rollover, and (iv) exceptionally *catastrophic overwash* inducing barrier breaching. These different barrier responses to storm events are controlled by the elevation difference between the extreme water level (including runup) and the barrier crest, which is known as *freeboard* (Orford and Anthony, 2011). When the extreme water level does not exceed the crest height (i.e., positive *freeboard*), regime of energetic swash processes induce the raising of the barrier. In contrast, as the extreme water level starts to exceed the crest height (i.e., negative *freeboard*), the top of barrier starts to erode and sediments are displaced to the back-barrier slope. As the extreme water level and swash flows increase even more, overtopping is replaced by catastrophic overwashing that may open a breach along the barrier (Orford and Carter, 1995).

The breaching process also impacts the drift-aligned barriers, which are very sensitive to longshore sediment supply (Orford et al., 1991). The scarcity of sediment generally induces an erosion of the barrier in the updrift (proximal) zone. Along the barrier, selective sediment transports tend to lead to the formation of distinct erosion/accretion cells, and even sub-cells. Within each cell or sub-cell, sediment is eroded updrift to be accumulated downdrift (sink zone) where the shoreline is prograding. With time, these processes lead to a thinning of the updrift eroded zone (weaker point), eventually resulting in a breaching of the barrier (Orford et al., 1996).

The study of sandy- and gravel-dominated barrier breaching processes and the related environmental and socio-economic consequences has been the subject of numerous studies (Kraus and Wamsley, 2003; Wamsley and Kraus, 2005; Stockdon et al., 2007; Dornbusch, 2017; Plomaritis et al., 2018). The East and Gulf Coasts of the United States (i.e., from Florida to New York States), which are regularly impacted by severe hurricanes, have clearly been the most studied areas in the world for barrier breaches, particularly those of barrier-islands (Plant et al., 2010; Plant and Stockdon, 2012; Stockdon et al., 2012, 2013). In natural areas with no human settlements, the consequences are essentially environmental due to the modification of hydrologic exchanges between the sea and the back-barrier lagoons (Kraus et al., 2002). These modifications can result in increased water levels linked to the inflow of marine water (Elsayed and Oumeraci, 2016), inducing saltwater intrusion to the deeper freshwater aquifers (Elsayed and Oumeraci, 2018). Under these conditions, the biodiversity of the coastal wetland ecosystem is affected by the changes in the salinity of the surface water (Li et al., 2020). In terms of morphological features, overwashing flows causing erosion and barrier breaching generally lead to inlet formation (Leatherman, 1979a; Nienhuis et al., 2021). The removed sediments can then be deposited and form washover fans (Leatherman, 1979b; Carter and Orford, 1981, 1984). However, the most significant risk generated by the opening of breaches in the coastal barriers deals with flood hazard management and habitat conservation (Pye and Blott, 2009; Durand et al., 2010; Pollard et al., 2021). The threats to coastal communities due to the damage of property (including loss in life) have led to an in-depth assessment of the storm overwash induced breaching hazards on coastal barriers (Schoonees et al., 1998; Kraus et al., 2002; Plant et al., 2010; Plant and Stockdon, 2012; Stockdon et al., 2012, 2013; Plomaritis et al.,

2018).

This present study deals with the assessment of the flooding risk of a low-lying inhabited area of the Laneros Peninsula after the opening of a breach in the Sillon de Talbert spit barrier (North Brittany). This breach opened in March 2018 in the proximal section of the barrier spit (Suanez et al., 2018a), leading the inhabitants and politicians of the municipality to fear the possibility of coastal flooding. While the scientific council of the Sillon de Talbert Natural Reserve refused any engineering intervention (such as those proposed by Stéphan et al., 2018a) aimed at filling the breach with sediment replenishment, the mayor of Pleubian wished to carry out a study on the coastal flooding risk of the low-lying zone of the Laneros Peninsula located behind the breach. Besides the purely scientific aspects, the objective of this study was also to give the potentially impacted inhabitants accurate information on the potential flooding. This study was carried out between 2020 and 2021 with the help of a consulting company specializing in hydrodynamic modelling, taking into account several hypothetical scenarios of morphological evolution of the breach and/or the barrier in its proximal part.

2. Study area

2.1. Geomorphologic and hydrodynamic setting

The gravel barrier spit of the Sillon de Talbert is located on the northern coast of Brittany in the department of Côtes d'Armor (Fig. 1). This coast experiences a megatidal range of up to ~11 m for the highest astronomical tide (SHOM, 2016). The most frequent swells come from the WNW with a resultant vector of around 303°N (Fig. 1b). Consequently, the waves break with an angle according to the average coastline's orientation (~50°N). Therefore, this non-parallel swash alignment generates a longshore current oriented from the SW to the NE. The most frequent offshore wave heights (H_{m0}) range between 1 and 1.5 m, and between 9 and 10 s for wave period (T_p). During storms, wave heights can reach 9 m with periods of 20 s (Suanez et al., 2022).

The Sillon de Talbert gravel barrier spit stretches over 3.5 km long and it is composed of a volume reaching $1.23 \times 10^6 \text{ m}^3$ of sandy-gravel sediment (Stéphan et al., 2012). This barrier shelters a large intertidal zone corresponding to a sandflat scattered with reefs and some Pleistocene marine deposits. The highest parts of the sandflat are covered with a dense halophyte vegetation, particularly in the La Petite Grève area towards the back of the proximal part of the spit (Fig. 2b). The barrier spit is driven by both longshore and cross-shore dynamics (Stéphan et al., 2018a; Suanez et al., 2018a), however, since cross-shore sediment transfers are dominant as compared to longshore sediment transfers ($430,000 \text{ m}^3$ vs $52,000 \text{ m}^3$ between 2002 and 2019) (Suanez et al., 2020), the Sillon de Talbert is considered to be a single-ridge swash-aligned barrier. According to the morphological and sedimentary features, Stéphan et al. (2012) have subdivided the barrier into four distinct morphosedimentary units (Fig. 1c), from the proximal sandy dune section (Unit 1) to the gravel distal section (Unit 4). These two sections are the most stable in terms of shoreline dynamics, while the last two sections, corresponding to the proximal gravel section (Unit 2) and the gravel median section (Unit 3), have displayed the largest retreat since 1930, up to ~160 m and ~150 m, respectively (Stéphan et al., 2012, 2018a; Suanez et al., 2018a). The long-term morphological evolution of the Sillon de Talbert indicates that at the beginning of the 18th century its morphology has changed from a barrier anchored at both ends, to a barrier spit disconnected from the islets of the Olone archipelago located in the NE (Fig. 1c) (Stéphan et al., 2012). This change of morphology increased the longshore sediment transport through a cannibalization process, mainly throughout the 19th and 20th

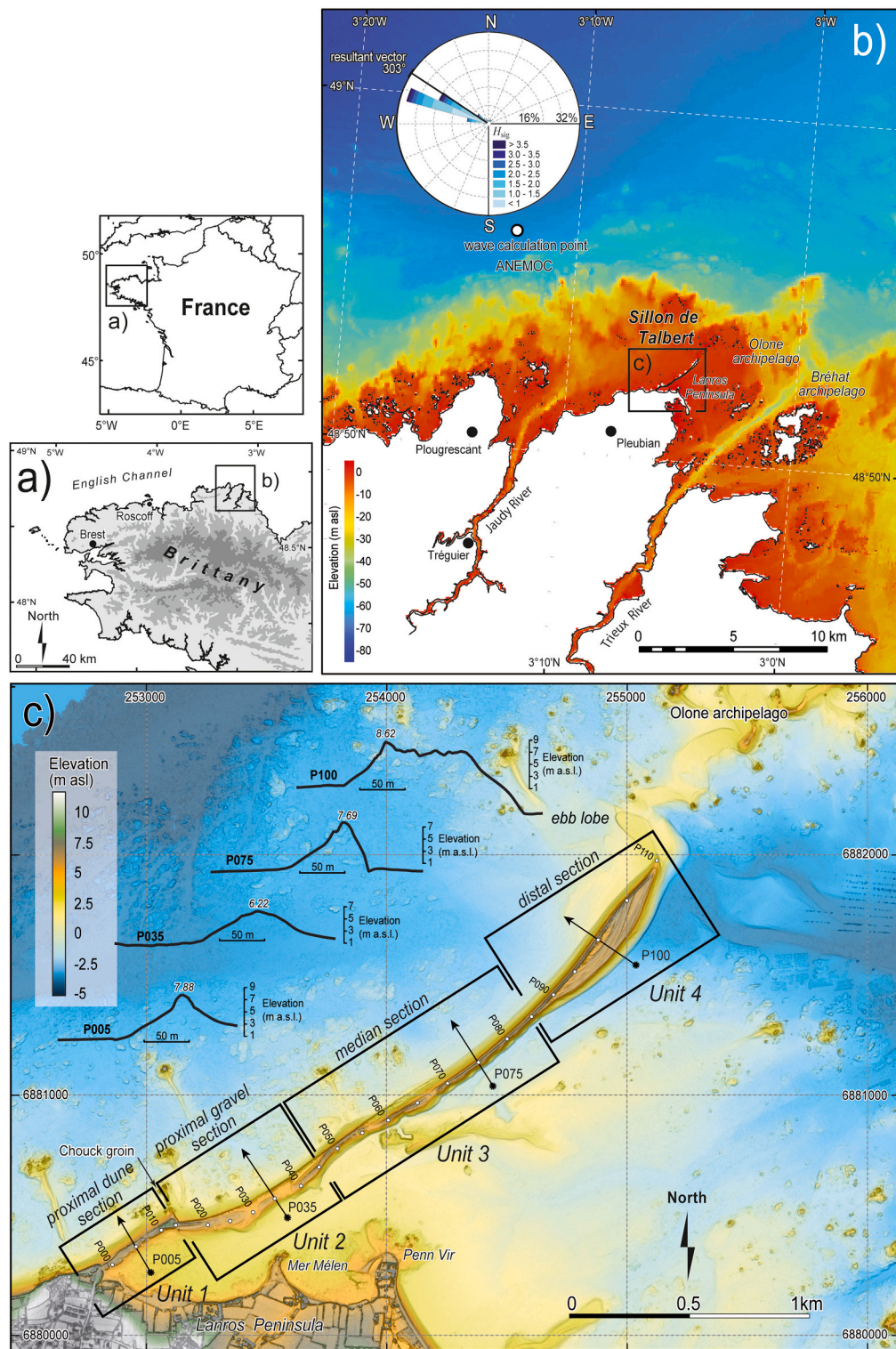


Fig. 1. Location map. (a) regional scale; (b) local scale. Wave rose established from the data obtained by the ANEMOC numerical model over the period of 1979–2002 (source: *Laboratoire National d'Hydrologie et d'Environnement, LNHE-EDF Chatou, and CEREMA-Brest*) at the calculation point $3^{\circ}12.66'$ W; $48^{\circ}56.28'$ N; depth of 36.1 m. (c) Different longshore morphological units of the spit and representative beach profiles of the four units (after Suanez et al., 2018a, modified).

centuries with the sediment depletion and rollover of the landward displacement of the barrier spit. As indicated above, Stéphan et al. (2012) calculated an average of landward migration rate of up to -1.1 m.yr $^{-1}$ between 1930 and 2010. More recently, Stéphan et al. (2018a) and Suanez et al. (2018a) indicated an increase of this averaged rate over the last fifteen years (2002–2017), reaching -2 m.yr $^{-1}$. A recent

study based on a high frequency survey carried out along two beach profiles between 2012 and 2019 shows a landward migration rate reaching -3.3 to -4.3 m.yr $^{-1}$ (Suanez et al., 2022). Both longshore and cross-shore dynamics affecting sediment transport and spit barrier migration lead to the opening of a breach on March 2018 on the proximal section of the spit barrier (Suanez et al., 2018a).

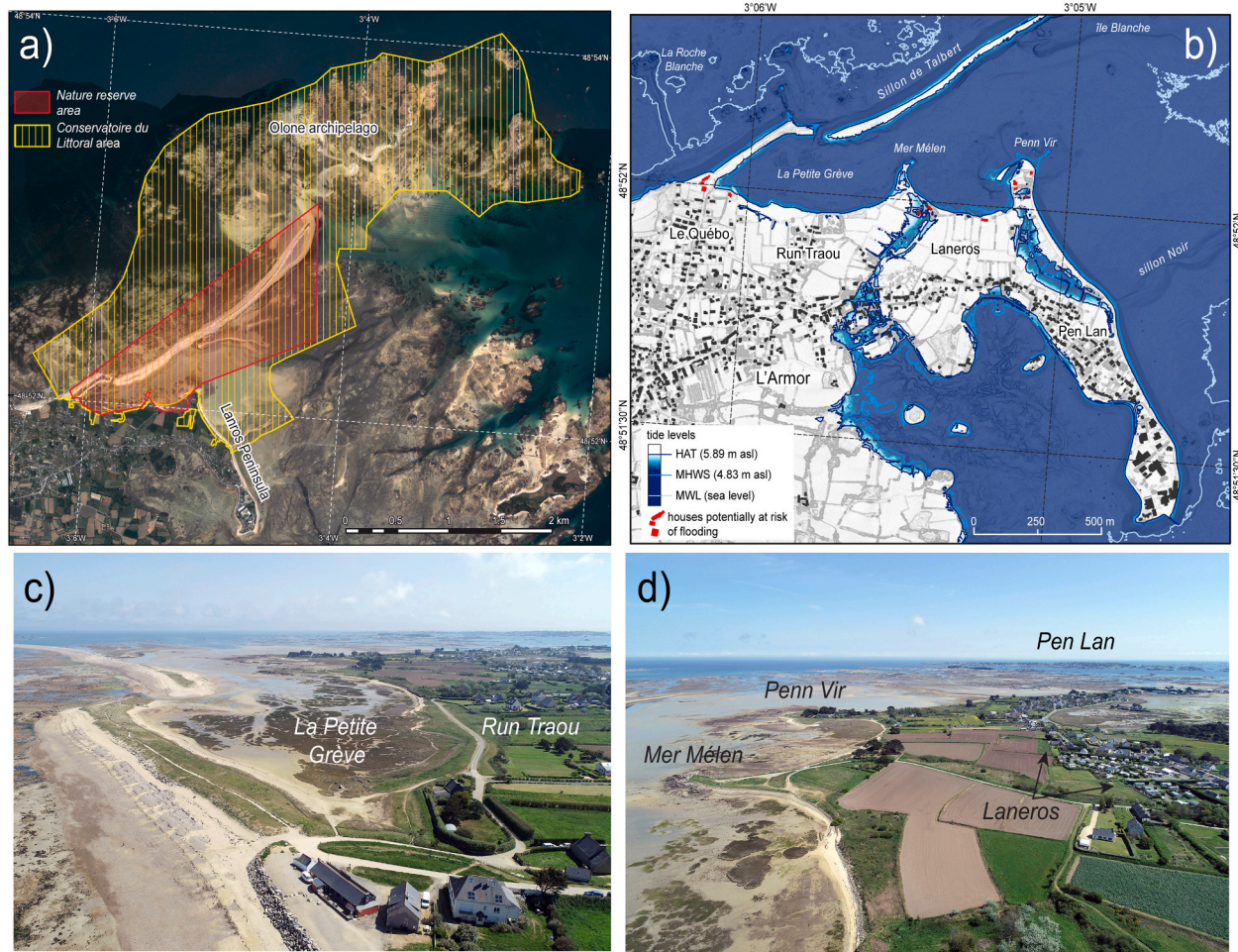


Fig. 2. Anthropogenic features. (a) Protected areas of the “*Conservatoire du Littoral*” (yellow) and nature reserve (red). (b) Map of human settlements in habitats along the Laneros Peninsula coastline. Source: DEM is a merge of the 2012 LiDAR data from the *Service Hydrographique et Océanographique de la Marine* database Lito3D® (SHOM, 2008) and a drone measurement of the breach section achieved in 2019. Cadastral data on building locations for the entire study area come from the French government's open access database (<https://cadastre.data.gouv.fr/>). (c) and (d) Aerial photos of *La Petite Grève* (photo credit: J. Ammann 2023-03-02). (d) Aerial photography of *La Petite Grève* and *Mer Melen-Laneros*, respectively (photo credit: J. Ammann, 2023-03-02).

2.2. Management policy and human settlement setting

The Sillon de Talbert is part of a protected natural area called “Réserve Naturelle Régionale du Sillon de Talbert” (<https://www.reserve-s-naturelles.org/sillon-de-talbert>) created in 2006 by the Brittany region and the French State. The perimeter of this nature reserve covers around 205 ha (Fig. 2a). In addition, the “*Conservatoire du Littoral*” has established a preemption area on the privately owned lands bordering the southern limit of the Nature Reserve, which was extended to include the archipelago of Olone in 2018 (Fig. 2a). Three stakeholders have established a management plan for a period of five years: the Brittany region, Conservatoire du Littoral, and the local authorities (municipality of Pleubian). The latter is in charge of the implementation of the management actions, which are defined and voted on by the scientific council of the Nature Reserve. Therefore, the municipality of Pleubian, through the authority of the mayor, cannot carry out any intervention on the morphology of the Sillon de Talbert barrier spit –especially in terms of engineering works– without the agreement of the scientific council of the nature reserve.

The gravel spit barrier acts as a “natural structure” for coastal defence. It mainly protects the Laneros Peninsula located behind the proximal section of the spit (Fig. 1). The role of coastal defence is even more important as this peninsula is urbanized (Fig. 2b). Though most of the housing is located in the south of the peninsula, there are still a few

isolated houses close to the shoreline on the north coast. As indicated in the paragraph above (Section 2.1), the question of the risk of coastal flooding, even if very limited in this area, arose when the breach opened in March 2018 in the proximal section of spit.

Fig. 2b illustrates the morphological and hydrodynamic context taking into account the Mean High Water Spring tide (MHWS) which reaches 4.83 m asl, and the Highest Astronomical Tide (HAT), which reaches 5.89 m asl (above sea level –asl– used throughout the text refers to the topographic reference level corresponding to the French geodetic Datum NGF-IGN69). We can see that on the north coast of the peninsula, about ten houses near the shoreline are potentially subject to the risk of coastal flooding. Indeed, the highest astronomical tide level (HAT) is very close to these houses, especially in the sector of *La Petite Grève* (Fig. 2c) and *Mer Melen* (Fig. 2d), between the neighborhoods of *Le Québo* to the west, and *Laneros* to the east. This sector is low-lying and oriented from the north to the south, which extends to the very dense housing zone located to the south. It is mainly in this sector that the risk of coastal flooding is of the greatest concern for the local population.

3. Opening and morphological evolution of the breach

The opening of the breach in the proximal part of the Sillon de Talbert took place between the 3rd and 4th of March 2018, during a high spring tide (tide level decreased from 5.54 to 5.18 m asl between March

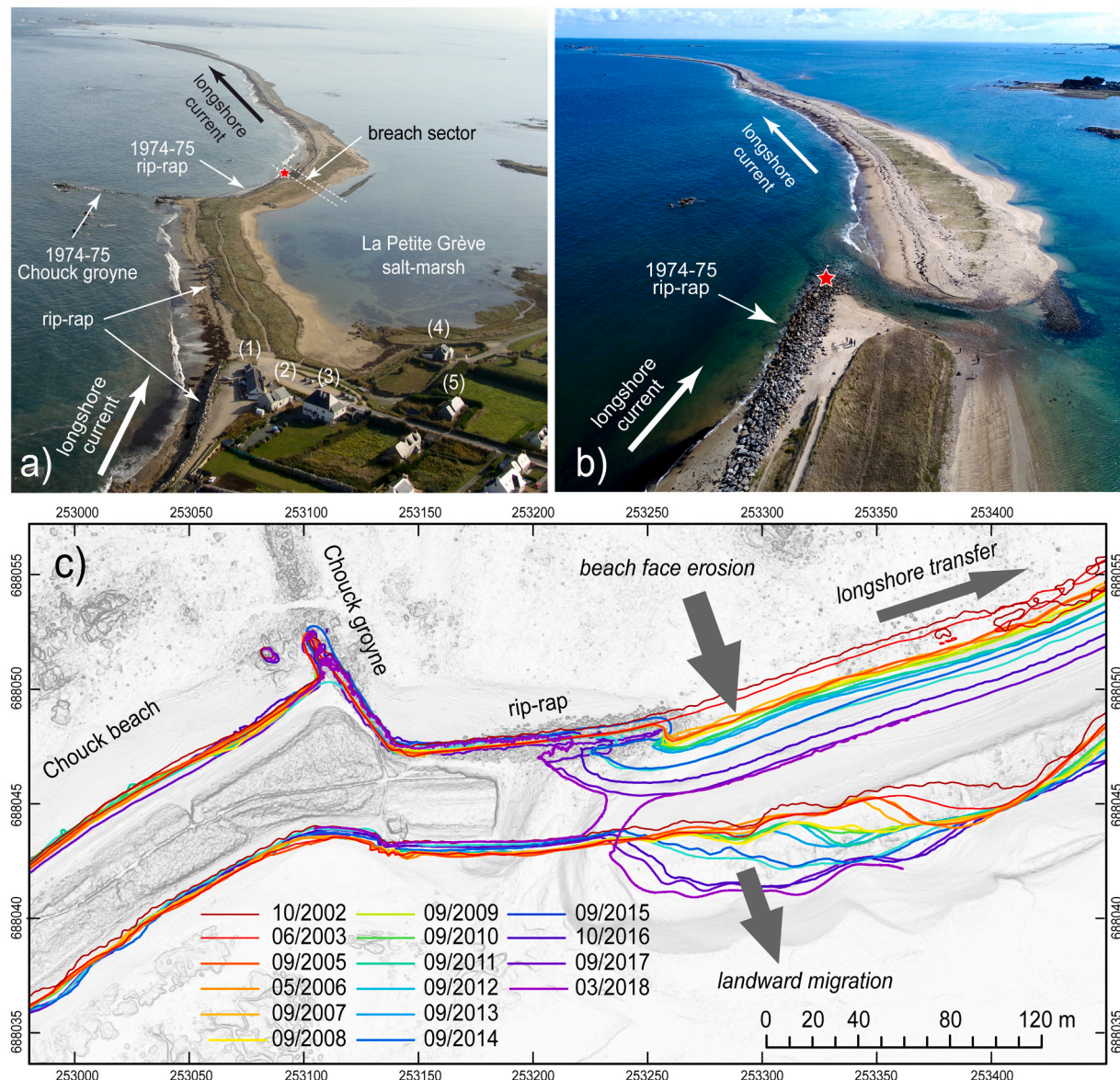


Fig. 3. (a) Aerial photo of the Sillon de Talbert before the opening of the breach (Photo credit: D. Halleux, September 23, 2009). (b) Aerial photo of the breach on the proximal section of the Sillon de Talbert 6 months after the opening (Photo credit: J. Ammann, September 14, 2018). Both photos show coastal defence structures and longshore currents. Numbers correspond to the houses built on the coastline. (c) Shoreline changes of the proximal section between 2002 and 2018. The limit of the shoreline is defined by the highest astronomical tide level (HAT) extracted from DEMs produced from 2002 to 2018.

3rd and 4th, and surge from 0.39 to 0.34 m) and fair offshore wave conditions (significant wave height from 1.22 to 0.40 m) (Fig. 3a and b). The breach opening was therefore due to the barrier flooding by a tide with strong ebb tide current, not by energetic waves. As indicated above, this rupture was part of a long process of erosion of the proximal part of the barrier through a cannibalization phenomenon (Suanez et al., 2018a). This evolution resulted in a very significant reduction in the width of the barrier in this weakened sector (Fig. 3c), which the authors described as a “wasp’s waist” (Stéphan et al., 2018a).

The significant morphological evolution of the breach was extremely rapid and significant during the first year after it opened. The topomorphological survey undertaken from February 2018 using KAP (Kite Aerial Photography) and UAVs (Unmanned Aerial Vehicle) indicated wide-spread morphological changes (Fig. 4a). Between February 2018 and May 2023, the breach gradually widened by about 50 m and deepened of about 3 to 3.5 m (Fig. 4b). The evolution of the coastline in the area of the breach shows that the retreat of the western bank has been continuous over time, following an east-west progression (Fig. 4c).

The evolution of the eastern bank is more complicated. It has resulted in a lowering of the beach profile of up to 2.5 m due to the landward migration through a rollover process (Fig. 4b, c).

However, since the end of 2019 and beginning of 2020, the breach channel incision has stopped with the complete removal of the soft sedimentary accumulation of the barrier (sands and pebbles). Much of this sandy material actually built up a large flood lobe that accumulated as a washover fan in the back-barrier salt marsh, which grew over time (Fig. 5a, b, c). Beyond the morphosedimentary and hydrodynamic aspects, the accumulation of this sandy washover fan has also had an impact on the marsh’s ecological environment, particularly in terms of flora. Since 2020, the erosive dynamics have impacted the compact and resistant Pleistocene hard clay layer, which significantly limits the incision of the channel through the breach (Fig. 5d). Currently, the current main evolution of the breach is a continuous retreat of its western bank, and a displacement by rollover of its eastern bank, which tends to flatten through a spreading of the material (Fig. 4b, c).

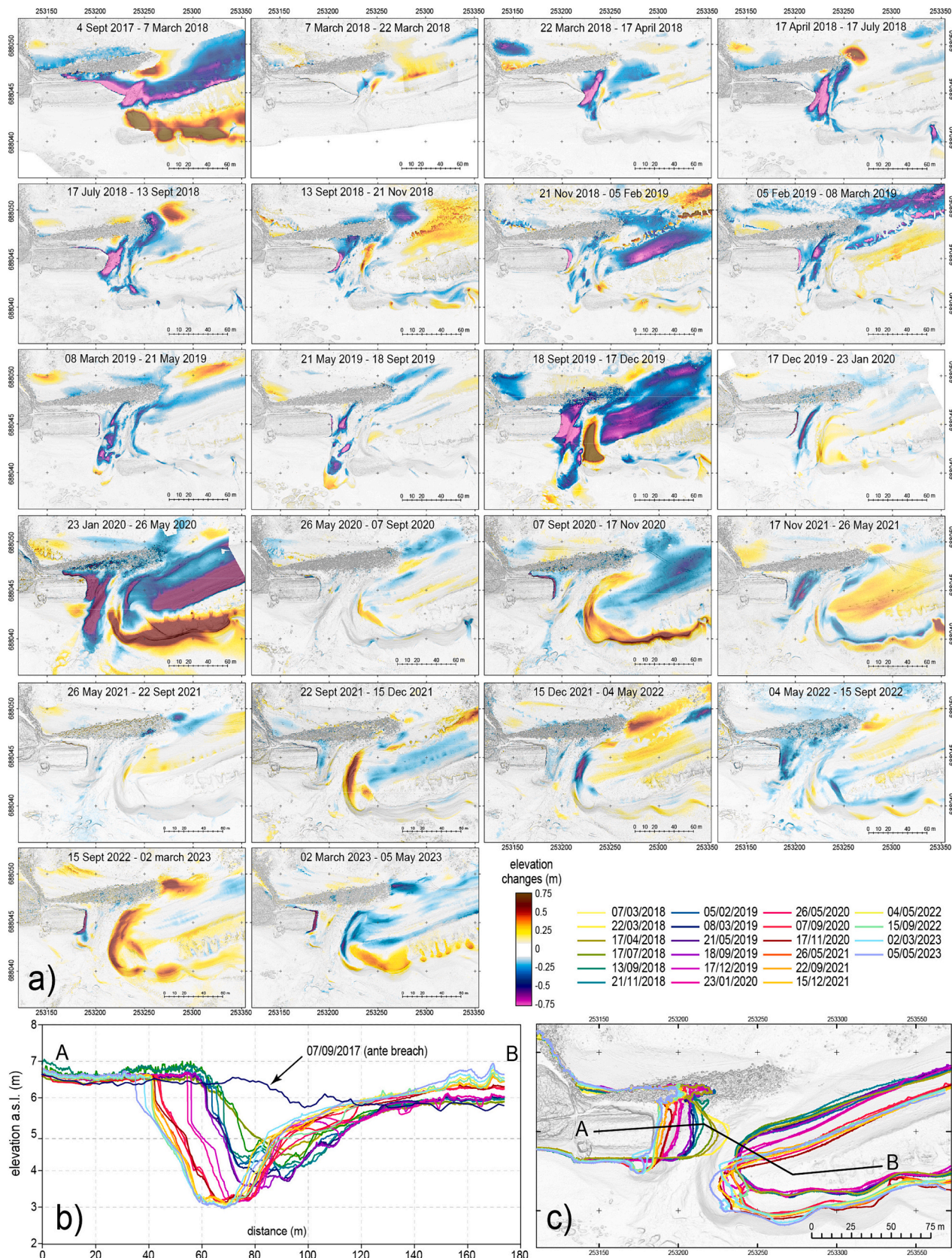


Fig. 4. Morphological evolution of the breach based on elevation changes between September 2017 and December 2021 (a). (b) Morphological changes of the breach along the cross-shore profile A-B. (c) Shoreline changes on the breach area since it opened (from 07/03/2018 to 15/12/2021).

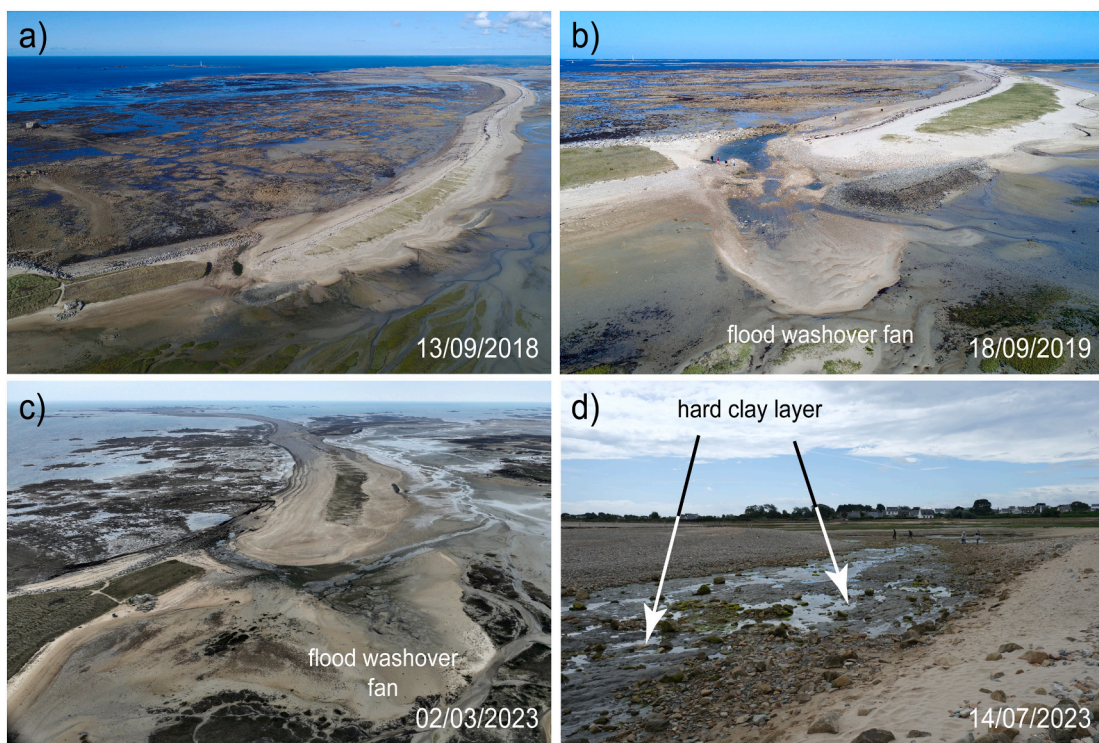


Fig. 5. Morphological changes of the breach zone between 2018 and 2023. a) Morphology of the breach six months after opening. No washover fan has yet accumulated (Photo credit: Jérôme Ammann – 13/09/2018). b) Washover fan corresponding to the sandy flood lobe accumulated on the back-barrier salt marsh through the breach of the Sillon de Talbert (Photo credit: Jérôme Ammann – 18/09/2019). c) Five years after the opening of the breach, the enlargement of the washover fan is linked to the widening of the breach, which favors more intense sediment transport (Photo credit: Jérôme Ammann – 02/03/2023). d) Photo taken on July 14, 2023 showing of the hard clay layer on the bottom of the breach (Photo credit: Julien Houron).

4. Data and methods

The numerical modelling system employed in the present study to further analyse the effect of the Sillon de Talbert gravel barrier breaching on the hydrodynamics of the area is described in this section, along with the required data and forcing processes.

4.1. Dataset

4.1.1. Topo-bathymetric data

The topo-bathymetric setting used in the modelling system corresponds to a merging from three different sources. The first dataset is a high resolution (1×1 m) topo-bathymetric digital elevation model (DEM) produced by IFREMER using airborne LiDAR measurements from October 2002 (Boersma and Hoenderkamp, 2003). These data cover both the terrestrial and the intertidal zone up to a depth of -5 m asl, from the Jaudy estuary in the west to the Bréhat archipelago in the east. The second dataset corresponds to the DEMs (ante- and post-breaching, i.e. September 2017 and October 2019, respectively) produced as a part of the topo-morphological survey of the Sillon de Talbert (Stéphan et al., 2018b, 2023). These data were collected using DGPS measurements in *Real Time Kinematics* mode. The third dataset consists of the bathymetry, extended from the tidal zone to the shelf platform, corresponding to the DEM HOMONIM provided by the *Service Hydrographique et Océanographique de la Marine* (SHOM), with a resolution of ~ 100 m.

4.1.2. Tidal, wave and atmospheric forcing

The predicted astronomical tides were obtained from the tidal database FES 2014 (finite element solution), produced by Noveltis, Legos, and CLS and distributed by Aviso+, with support from Cnes (Carrere et al., 2016), using 34 harmonic tidal constituents with a spatial

resolution of $1/16^\circ$.

Offshore wave data from 1994 to 2016 were obtained from the HOMERE hindcast dataset (Boudière et al., 2013). This hindcast was generated with the WAVEWATCH III® (WW3) spectral model (Roland and Ardhuin, 2014; Tolman and the WAVEWATCH III® Development Group, 2014). The model is based on an unstructured grid covering the Channel - Bay of Biscay area with a spatial resolution of ~ 250 m in the coastal zone. The model was forced by wind fields from the NCEP-CFSR (NOAA) reanalysis with a spatial resolution ranging from 0.25° to 0.5° (Saha et al., 2010) and by the surface currents generated from an atlas of harmonic tidal constituents obtained from outputs of the MARS circulation model (Lazure and Dumas, 2008).

Wind (speed and direction) and atmospheric pressure fields were accounted for the hydrodynamic part of the numerical modelling system in order to represent storm surge, wind-induced currents, and their effects on wave fields. They were obtained from the CFSR (Climate Forecast System Reanalysis) database produced by the NCEP and based on a global model that uses observations from data sources including surface observations, upper air balloon observations, aircraft observations, and satellite observations (Saha et al., 2010).

4.2. Model description

The numerical modelling system uses the hydrodynamic model Telemac-2D (Ata, 2018), coupled with the phase-averaged wave model TOMAWAC (Fouquet, 2018).

4.2.1. Telemac-2D for hydrodynamic modelling

The Telemac-2D model, developed by the “Laboratoire National d’Hydraulique et Environnement” (LNHE), was used to simulate hydrodynamic conditions. Telemac-2D solves the shallow-water (Saint-Venant) hydrodynamic equations using finite-element or finite-volume

methods on unstructured computational meshes. These equations express the conservation of mass (continuity equation) and the conservation of momentum (dynamic equations) in the two horizontal space directions (2DH) at any point of the computational domain. Telemac-2D has been frequently used to simulate hydrodynamic conditions in coastal, river, and estuarine zones (Breugem, 2020) as it deals with non-permanent free surface flows in shallow water. The model uses unstructured meshes, which are skilled in representing complex geometries by locally refining the resolution of the computational grid near the shoreline (Galland et al., 1991).

Telemac-2D takes into account the meteorological effects by integrating wind and atmospheric pressure, and calculates wave-induced currents, and wave setup based on the concept of radiation stress. The model can also simulate hydrodynamic conditions on the intertidal zones alternatively covered and uncovered by the water over time.

4.2.2. TOMAWAC for wave propagation

The TOMAWAC simulation module is used to model spectral wave progradation in coastal areas. It is based on the wave action density evolution equation (i.e. the energy density divided by the pulsation). Since TOMAWAC is a “third generation” model, it does not impose any parameterization on the spectral or directional distribution of the wave energy (or wave action). The simulation includes various processes such as (i) wave-bottom interaction (including refraction, shoaling, bottom

friction, and breaking depth effects), (ii) wave-atmosphere interaction (including wind-to-wave energy transfer, white capping, nonlinear energy transfers between frequency quadruplets effects), (iii) wave-current interaction (including refraction, shoaling, counter-current breaking), and (iv) wave-tide interaction.

4.2.3. Wave-currents interactions

The interactions between currents and waves can lead to variations in the wave direction, frequency, and amplitude (Ardhuin et al., 2012; Villas Boas et al., 2020). In the macro to megatidal environments, the effects of currents on waves are emphasised by the tide. The dissipation of waves by strong currents (wave blocking effect) is parameterized according to the formulation by van der Westhuyzen et al. (2012). When wave propagation is impeded by an opposing current, wave height and steepness increase and can break. An energy transfer within the wave spectrum can then be observed in areas with strong currents. These effects are simulated by coupling Telemac-2D and TOMAWAC data every 1 min, in order to provide information to each other, i.e., water depth and current from Telemac-2D to TOMAWAC and radiation stresses from TOMAWAC to Telemac-2D.

4.2.4. Model domain and boundary conditions

The employed numerical modelling system is based on a finite element method (FEM) using a unique unstructured grid (triangular

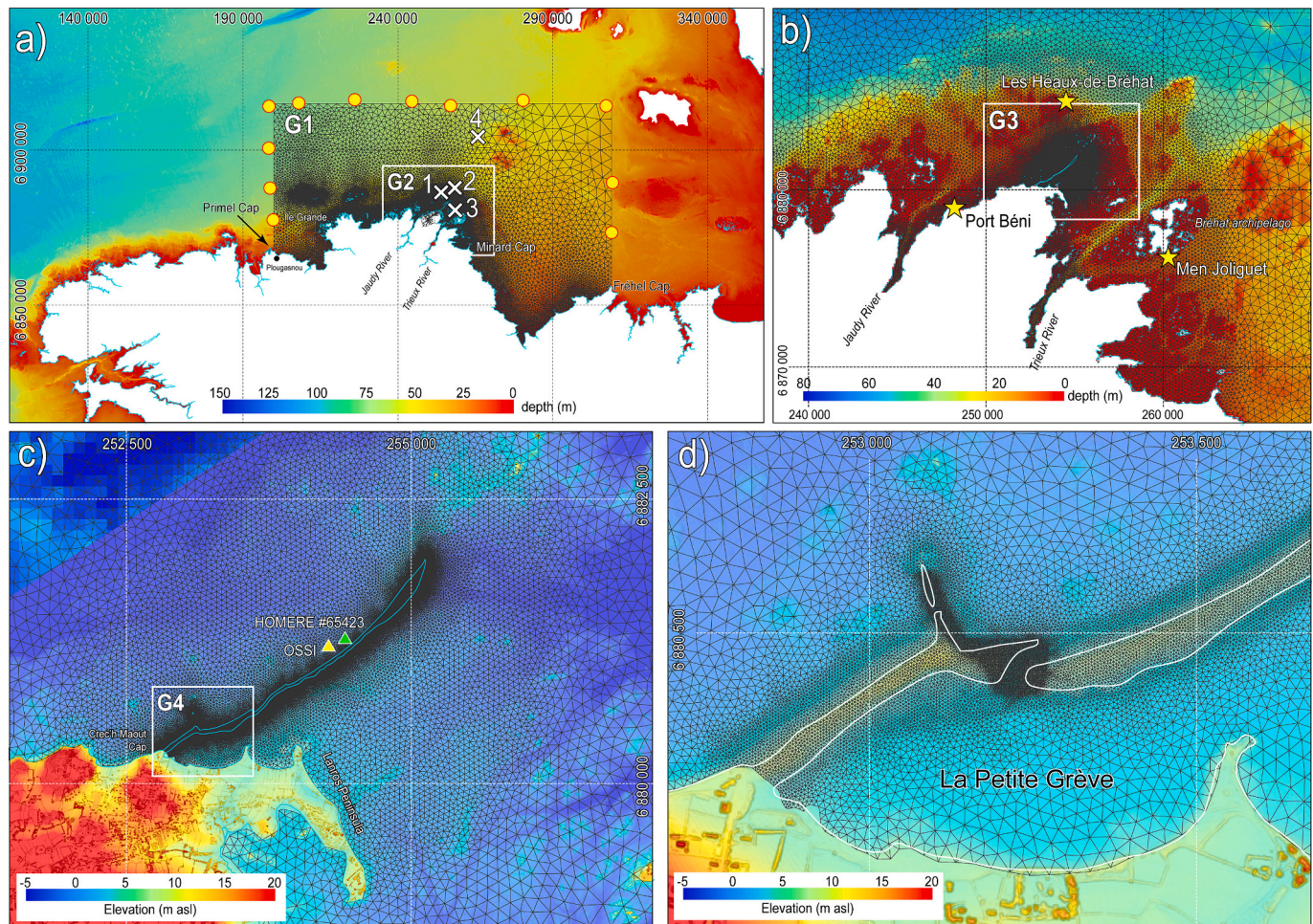


Fig. 6. Model setup based on a single unstructured grid, from coarse (G1: 2–3 km), to medium (G2: 500–200 m, and G3: 100–50 m), to small (G4: 5–2 m) spatial resolution. The yellow circles in (a) indicate the location of the HOMERE wave data extraction points used for wave forcing at the grid boundary. White crosses in (a) represent the location of the four calculation points used for the validation of the current velocity and direction between the Telemac-2D model and the predictions achieved by the SHOM. Yellow stars in (b) correspond to the three locations of tide predictions by the SHOM to validate the Telemac-2D simulated water levels. Yellow and green triangles (c) correspond respectively to wave measurement and modelling (WW3 HOMERE) points used in Section 4.5.

meshes) for both hydrodynamic and wave modules. Unlike regular grids, the meshes associated with unstructured grids can be coarse in a wide zone far from the study area, becoming finer the closer you get to the area of interest. In this study, a single grid was used consisting of 56,175 nodes and 110,642 triangular elements. In order to correctly represent large-scale hydrodynamic processes such as tide propagation,

the computational grid extends over ~ 108 km along the west-east direction, from the Primel Cap (Plougasnou town) to the Fréhel Cap, and extends up to 35 km offshore to the north of the Sillon de Talbert (Fig. 6a). The offshore limit of the computational grid has been defined in such a way that the positions of the 2D sea-state spectra (frequency/direction) in the HOMERE database (yellow circles in Fig. 6a)

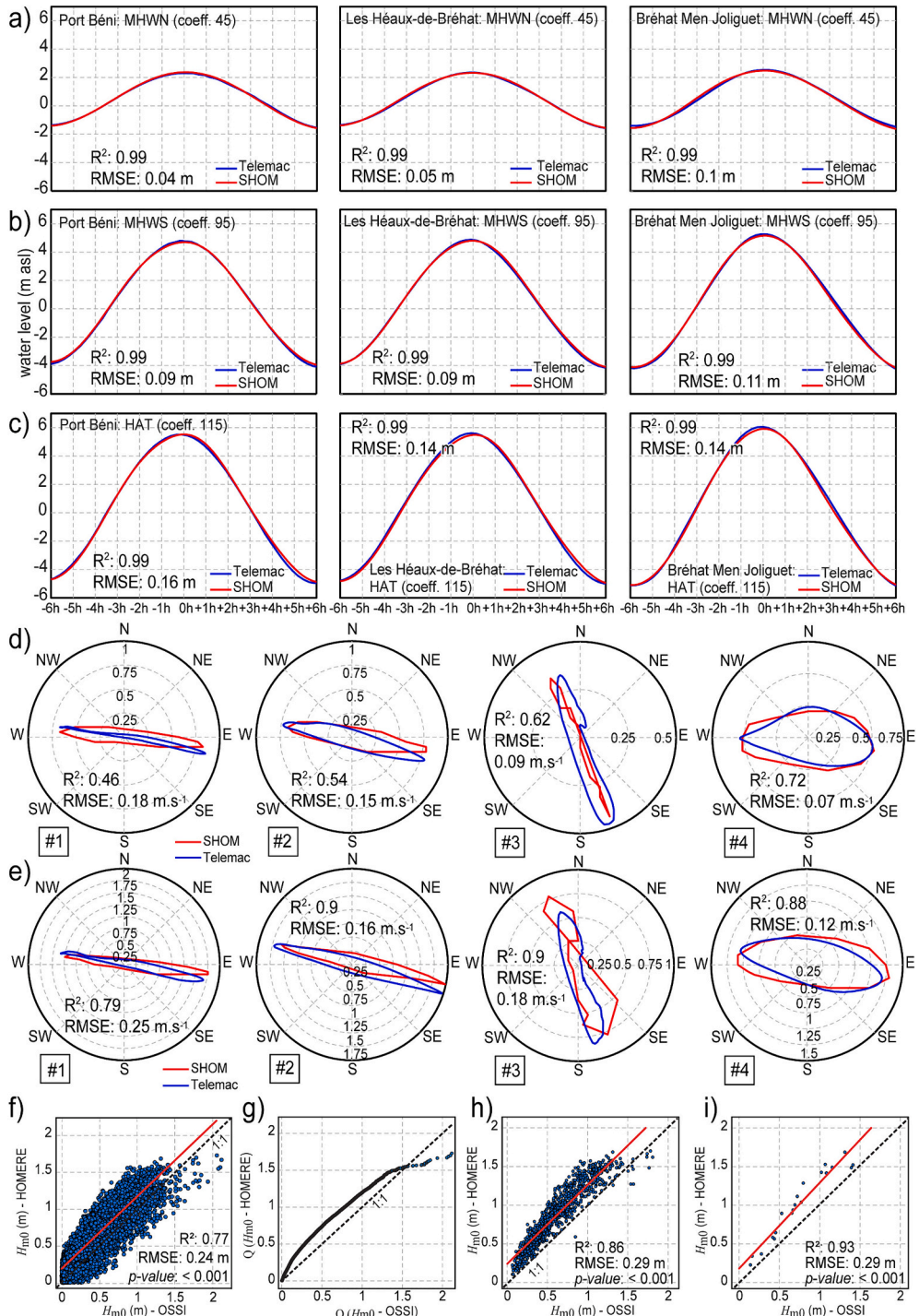


Fig. 7. Comparison of water levels (m asl) between the Telemac-2D model (curves in blue) and the SHOM predictions (curves in red), for three tide conditions: (a) mean high water neap (MHWN) corresponding to the French tide coefficient 45, (b) mean high water spring (MHWS) corresponding to the French tide coefficient 95, and (c) high astronomical tide (HAT) corresponding to the French tide coefficient 115, for the three reference ports of Port Béni, Les Héaux-de-Bréhat, and Bréhat Men Joliguet (see Fig. 6b). Comparison of tidal currents ($m.s^{-1}$) between the Telemac-2D model (curves in blue) and the SHOM tidal current predictions (curves in red) for a mean high water neap (d) and mean high water spring (e) at four different location extraction points (see Fig. 6a). Comparison of situ pressure sensor (OSSI) and WW3-simulated (HOMERE) wave heights (H_{m0}) over the period 2012–2016 (f). Q-Q graph of the entire wave dataset (g). Comparison of both wave datasets for tide levels above MHWS (h) and HAT (i).

approximatively correspond approximately with nodes of the grid boundary. Offshore, the coarser mesh resolution is about 2–3 km (see G1 in Fig. 6a). The resolution of the mesh progressively decreases from 500 m to 200 m between Île-Grande and Minard Cap (see G2 in Fig. 6b), then from 100 m between the Trieux and the Jaudy Rivers (see G3 in Fig. 6c) to ~50 m in front of the Sillon de Talbert (from Crec'h Maout Cap to Laneros Peninsula) (Fig. 6c), and from 5 m to 2 m in the tidal zone and the breach, respectively (see G4 in Fig. 6d).

The model used tidal elevation forcing data from the FES 2014 tidal database and hourly wave spectra from the WW3 HOMERE database (see Section 4.1.2). Output locations bordering the offshore boundary of the model domain were used to force the TOMAWAC model by interpolating the wave spectra along the offshore nodes of the model boundary. For the nodes forming the terrestrial boundary of the model, a “free evolution of the flow” condition was specified. In addition, CFSR atmospheric data (wind and pressure, see Section 4.1.2) were been considered for the wind-driven currents, the storm surge, and the wind-driven wave generation modelling.

Several tests were conducted and focused on the bottom friction law (Strickler, roughness length, etc.) and the associated friction coefficient. This parameterization was carried out mainly on water levels, and to a lesser extent on currents (not shown). The optimal parameterization deduced from this step led to the use of Strickler's Law with a coefficient of 25 for the friction on the bottom, and the Smagorinsky parameterization for the turbulence.

4.3. Hydrodynamic validation

4.3.1. Water level validation

Validation of the water level produced by Telemac-2D was completed by the comparison to the predicted tide levels calculated by the SHOM at three different locations (i.e. Port Béni in the west, Les Héaux-de-Bréhat to the north, and Bréhat Men Joliguet in the east) (see Fig. 6b), and for three tide conditions (i.e., mean high water neap - MHWN, mean high water spring - MHWS, and highest astronomic tide - HAT). SHOM reference data used here are neither measurements nor numerical model outputs, but result from a tidal harmonic analysis carried out over available in-situ measurements, followed by a recombination on MHWN, MHWS, HAT tide conditions (SHOM, 2005). Estimated from in-situ measurements during MHWS condition, the mean (normalized) errors on harmonic tidal prediction provided in SHOM (2005) is <15 % for the maximum current velocities, and <30 min for the average phase lag. In the three reference ports of Port Béni, Les Héaux-de-Bréhat, and Bréhat Men Joliguet (see Fig. 6b), the validation of water level also based on tidal harmonic analysis indicates the RMSE is between 10 and 12 cm, i.e. about 1 % of the total water level. These predictions and associated errors are derived from few days of in-situ observations (respectively 181, 132, and 72 days at Bréhat Men Joliguet, Les Héaux-de-Bréhat, and Port Béni). These values are in line with those given in previous studies (Giloy et al., 2023).

The validation of Telemac-2D outputs showed that the amplitude and phase of the tide were accurately reproduced for the three tide conditions with R^2 of 0.99 and RMSE increasing from 0.04 m to 0.14 m from MHWN condition to HAT condition, respectively (Fig. 7a, b, c). These margins of error are negligible in comparison with the tidal range (around 1–2 %).

4.3.2. Tidal current validation

Validation of the current velocity and orientation obtained by the Telemac-2D model was also carried out by comparing the model results with the predictions made by the SHOM (2005) at four different locations in the studied area (Fig. 6a). These data correspond to the hourly values of current velocity and orientation associated with the MHWN and MHWS conditions. The comparison we conducted showed that the Telemac-2D model is less consistent, with R^2 (ranging from 0.68 to 0.95) and RMSE tending to increase, the closer we get to the coast. Thus, at

point #1, the largest error margins are between 0.18 and 0.25 m.s⁻¹; and they decrease significantly at point #4 to reach 0.07 and 0.12 m.s⁻¹ (Fig. 7d, e). However, the maximum of velocity magnitudes in both directions are close to those from the SHOM model. The slight phase shift is mainly due to the differences in the temporal resolution of tide predictions, hourly and every 15 min for the SHOM model and Telemac-2D model, respectively. Differences could also be attributable to the different bathymetric data, bottom friction, or resolution used by the SHOM model and that of our study, especially in the shallow zone. Despite these uncertainties, the Telemac-2D model reproduces current directions and velocities satisfactorily.

4.3.3. Wave validation

Validation of the WW3 HOMERE dataset was carried out using records from a pressure sensor OSS1 010-003C (Ocean Sensor Systems Inc. ®, 1.5 cm accuracy) installed in the intertidal zone at coordinates 48°52'34.4554" N; -3°4'58.9127" W, and at a depth of -0.461 m asl depth (see Fig. 6c) (Suanez et al., 2018b). Correlation between both in-situ and WW3-simulated wave heights (H_{m0}) was achieved over the period 2012–2016, using a dataset extracted at the point #65423 (i.e., model node from WW3 HOMERE database) located at 48°52'36" N; -3°4'52" W, and at a depth of -0.56 m asl (see Fig. 7f). The choice of this extraction point was conditioned by the fact that it was the closest of the OSS1 pressure sensor location. The results show a good agreement between the two datasets, with R^2 of 0.77 and RMSE of 0.24 m, despite a slight global overestimation of H_{m0} (WW3) compared with in-situ H_{m0} (OSSI) as shown by Q-Q plot graph (Fig. 7g). Comparison of the two datasets also shows an underestimation of the highest WW3-simulated wave height. It is a systematic bias of the WW3 model, which has difficulty in reproducing the most extreme events (Mureau et al., 2022). The biases observed between the two series for extreme values are also related to in-situ recordings, as the pressure sensor is installed in the intertidal zone. Thus, when the depth of the water column is at a minimum while the tide is rising or falling, aberrant water level values are recorded. Therefore, all recordings at +1 h and -1 h before or after the sensor is submerged are removed as they are considered outliers. When the correlation is restricted to wave records associated with tide levels above MHWS (i.e., 4.83 m asl) and HAT (i.e., 5.89 m asl), the fits are significantly improved, with R^2 increasing from 0.86 to 0.93, respectively, and an RMSE of 0.29 m (Fig. 7h, i).

4.4. Modelling strategy

The approach followed in this study was to model an extreme hydrodynamic event likely to generate significant coastal flooding. The associated simulations were based on five topo-morphological configurations for the gravel spit. Three of them correspond to hypothetic scenarios for the future morphological evolution of spit.

4.4.1. Extreme event selection

The choice of the most significant hydrodynamic event to model was based on the morphological and hydrodynamic monitoring of the Sillon de Talbert over the last two decades. Based on the analysis of the morphological changes extracted from annual DEMs measurements, and the hydrodynamic conditions (wave and water level) over the period 2002–2017, Suanez et al. (2018a) identified 11 significant morphogenetic events combining extreme wave height and water levels. Wave height was thresholded using the 2 % exceedance offshore wave height of 3.15 m, and the highest water level using the 2 % exceedance water level of 5.5 m (Table 1).

As shown in Table 1, storm Anne on February 1–2, 2014 was the most energetic event recorded over these 15 years of survey data. This high-energy storm exhibited a long wave period (T_p) of up to 18.2 s combined with high H_{sig} values up to 4.2 m. This event led to major morphological changes, as the maximum landward migration of the spit barrier reached between -30 to -20 m. These observations were confirmed by the study

Table 1

Inventory of the major morphogenetic events combining extreme storm wave heights and water levels (after Suanez et al., 2018a, modified). The shaded line correspond to the simulated storm event of February 1, 2014 (storm Anne). The wave energy flux is calculated using the formulation (F) according to Barnard et al. (2017) as follow: $F = \frac{\rho g^2}{64\pi} H_{m0}^2 T$ (1) where F is expressed per unit crest length of the wave (in $\text{J.m}^{-1} \text{s}^{-1}$), $\rho = 1025 \text{ kg.m}^{-3}$ is the density of seawater, and $g = 9.81 \text{ m.s}^{-2}$ is the gravitational acceleration, H_{m0} is the significant wave height, and T is the wave period.

| Date | Storm name | H_{sig} (m) | Wave dir. | T_p (s) | Water level (m asl) | time | Wave energy ($\text{J.m}^{-1} \text{s}^{-1}$) |
|------------|---------------|---------------|-----------|-----------|---------------------|----------|---|
| 28/02/2002 | * | 3.2 | 300° | 13.5 | 5.63 | 6:00 AM | 6.784×10^7 |
| 20/03/2007 | * | 3.4 | 344° | 7.6 | 5.56 | 6:00 AM | 4.273×10^7 |
| 10/03/2008 | Johanna | 3.4 | 296° | 13.7 | 5.95 | 7:00 AM | 7.578×10^7 |
| 31/03/2010 | * | 3.8 | 302° | 11.2 | 5.7 | 6:00 AM | 7.898×10^7 |
| 01/02/2014 | Anne | 3.3 | 295° | 12.3 | 5.98 | 6:00 AM | 6.471×10^7 |
| 01/02/2014 | Anne | 4.2 | 298° | 18.2 | 5.66 | 19:00 PM | 15.750×10^7 |
| 02/02/2014 | Anne | 3.4 | 297° | 16.7 | 5.89 | 7:00 AM | 9.329×10^7 |
| 09/02/2016 | Ruzica/Imogen | 3.3 | 296° | 16.4 | 5.54 | 6:00 AM | 8.687×10^7 |
| 09/03/2016 | * | 3.2 | 302° | 9.3 | 5.54 | 6:00 AM | 4.620×10^7 |
| 03/01/2018 | Eleanor | 4.6 | 303° | 13.1 | 5.61 | 6:00 AM | 13.530×10^7 |
| 04/01/2018 | Eleanor | 3.4 | 300° | 14.7 | 5.58 | 7:00 AM | 8.344×10^7 |

of morphological changes carried out using higher-frequency monitoring, based on monthly measurements of beach profiles (Suanez et al., 2022). For this study, covering the period 2012–2019, the analysis of morphological changes was also complemented by a study of the hydrodynamic conditions (wave and water level), which showed that the February 1, 2014 event generated the highest catastrophic overwash of the barrier spit with a water flow exceeding the crest by between 0.8 and

0.5 m.

For modelling, the observed tide levels recorded for this event were increased by around 80 to 90 cm at the model boundaries. This additional height makes it possible to reach the extreme water levels for a 100-year return period (i.e. between 6.4 and 6.6 m NGF) that have been statistically calculated by SHOM for the Sillon de Talbert area (SHOM/CETMEF, 2012). These centennial water levels are used to consider the

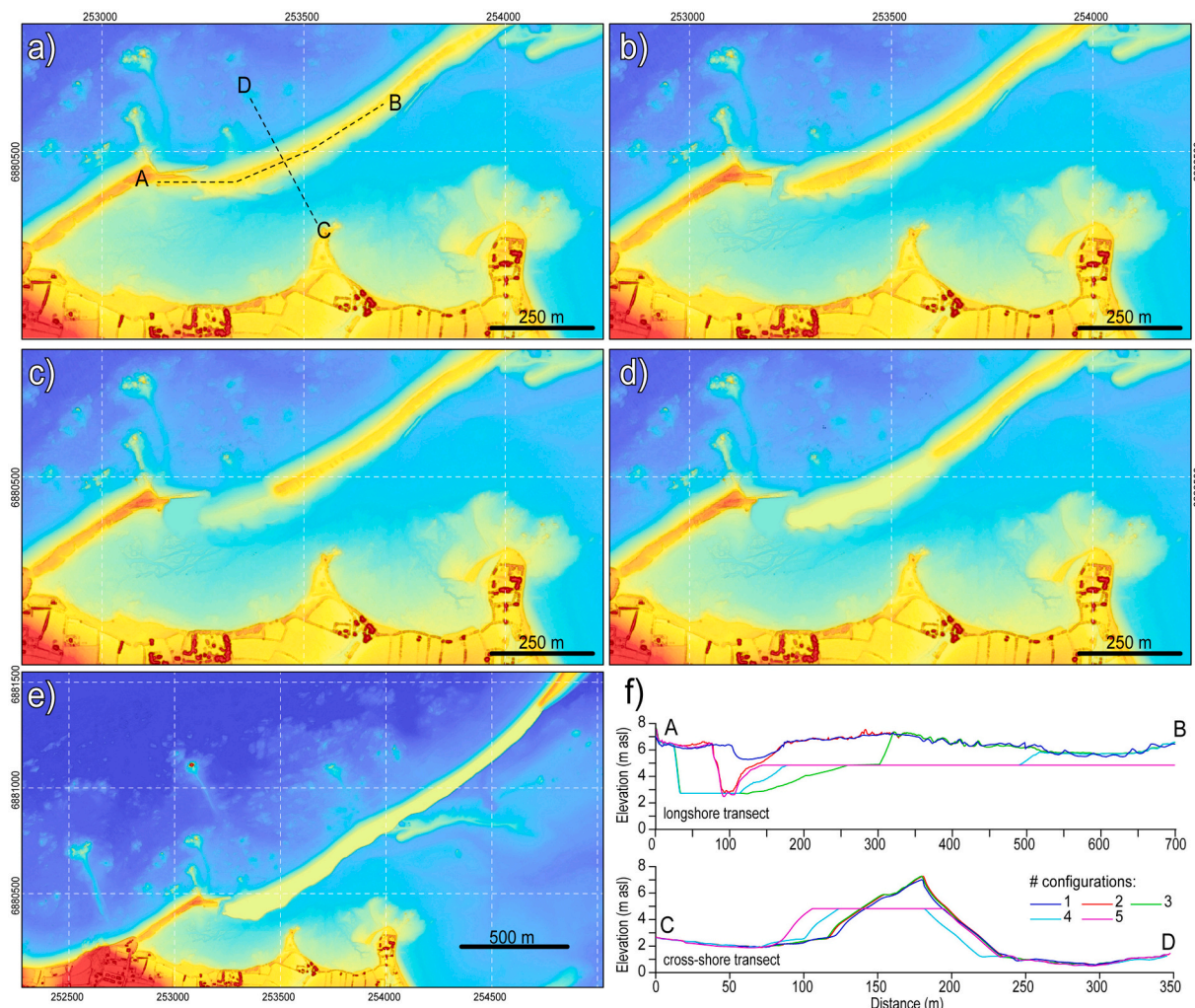


Fig. 8. Five morphological configurations used for the hydrodynamic modelling (a-e). (f) Elevation cross-shore and longshore profil.

exceptional nature of an extreme event, which constitutes the reference level in the methodological approach recommended by the French government for mapping the risk of marine flooding (Azzam et al., 2014).

4.5. Five morphological configurations for modelling

Hydrodynamic conditions (water level including tide, surge, and wave setup, and associated currents) were modeled taking into account five topo-morphological configurations (Fig. 8). Configurations #1 and #2 correspond to the ante-breach and post-breach morphological settings. They consist of the DEMs of 1×1 m resolution from September 2017 (i.e., 6 months before the barrier breaching; see Fig. 8a) and October 2019 (i.e., 18 months after the barrier breaching; see Fig. 8b), respectively. As indicated previously (i.e. Section 4.1.1), these data come from DEM measurements of the entire barrier spit carried out as part of the annual survey of morphological changes of the Sillon de Talbert (Stéphan et al., 2018b, 2023). Configurations #3, #4, and #5, are based on prospective scenarios. They take into account a barrier spit morphology based on the DEM of October 2019, which was deliberately modified.

Configuration #3 (Fig. 8c) illustrates a moderate breaching scenario, with the breach widening up to 300 m and a deepening up to 2.7 m asl over the next few years (~2025). The widening of the breach in this scenario was achieved by (i) eroding the western bank of the breach (value corresponding to this erosion was calculated by linear regression from measurements taken between March 2018 and December 2019), and (ii) by lowering the crest of the eastern bank of the breach of up to 4.20 m asl (below the MHWS tide level of 4.83 m asl) over a length of 300 m. This prospective scenario was also based on measurements taken during March 2018 to December 2019 (see Fig. 4c). The 2.7 m elevation of the deepening of the breach channel corresponds to the Pleistocene clay forming a hard non-erodible layer (see Fig. 5d). Finally, this configuration also took into account the nearly 10 m landward migration of the eastern bank of the breach, after the evolution of this section between March 2018 and December 2019 (see Fig. 4c).

Configuration #4 (Fig. 8d) illustrates the widening breaching scenario up to 500 m. The same prospective approach as the configuration #3 was used for the erosion of the western bank. For the eastern bank, we just considered the lowering of up to 4.83 m (corresponding to the MHWS tide level) of this section over a longer distance, as being the consequence of the medium term (i.e. 5 to 10 years) landward displacement of the barrier in the context of sediment depletion.

Finally, configuration #5 (crest lowering scenario) illustrates a complete lowering of the barrier after a complete removal of the crest due to catastrophic overwash events (Fig. 8e). The DEM constructed to simulate hydrodynamic conditions under this fictitious configuration corresponds to a modified version of the DEM from October 2019. The crest elevation was defined at 4.83 m asl because it corresponds to both the MHWS tide level and the lowest post-storm elevation measured along the barrier crest over the period 2002–2020. In this configuration, we also assumed a cross-shore sediment transfer from the crest to the back-barrier area, leading to a retreat by rollover and a widening of the crest. The volume of this cross-shore sediment was taken into account to estimate the corresponding retreat values of the barrier. Volumetric calculations were performed along 70 cross-sections using Surfer 10 software®. The retreat of the barrier (r) was then estimated using the following formulation:

$$r = \frac{V}{L^*H} \quad (2)$$

where V is the volume of sediment above the MHWS tide level, L is the length of the section, and H is the difference between the elevation of the back-barrier area and the MHWS tide level.

5. Results

5.1. High spring tide water levels and currents

Water levels and tidal current velocities associated with a tidal coefficient of 115 (i.e., near HAT condition) were first simulated for topo-morphological configurations #1 and #2, corresponding to the ante-breaching DEM of September 2017, and the post-breaching DEM of September 2019, respectively, without considering wave and atmospheric (wind and pressure) forcings (Fig. 9). At this stage, only tide effects were simulated in real conditions, without including the water level increase of around 80 to 90 cm corresponding to a 100-year event. The simulated water levels clearly show differences between the NW ocean side and the SE back-barrier sandflat. One hour before high tide (HT-1 h), the water level simulated on the ocean-side is only a few centimeters higher than on the back-barrier side (~5 cm), inducing tidal currents flowing north-eastwards along the spit until they reach the tip where the velocity increases as the water penetrates into the sandflat area (Fig. 10a). This tidal circulation pattern is observed under configurations #1 and #2. However, in configuration #2, southward tidal currents are flowing through the breach channel with a maximum velocity of 0.75 m.s^{-1} (Fig. 10b, c).

During high tide (HT), the water level simulated on the back-barrier side appears ~25 cm higher than on the ocean side (Fig. 9) while ebb tide currents (oriented north to north-west) increase in flow velocity at the tip of the gravel spit (Fig. 10d). The circulation pattern of the tidal currents is similar for configurations #1 and #2. However, in configuration #2, the difference in water level on either side of the barrier induces strong outflow tidal currents through the breach, where flow velocities reach about 2.2 m.s^{-1} (Fig. 10e, f).

One hour after high tide (HT + 1 h), water levels are higher, up to 37 cm in the back-barrier area (Fig. 9). In this case, the highest tidal current velocities are located at the tip of the spit for configuration #1 (Fig. 10g). For configuration #2, strong outflow tidal currents are flowing through the breach channel, again with velocities of 2.2 m.s^{-1} (Fig. 10h, i).

5.2. Extreme event simulations of 1st February 2014 storm

5.2.1. Post-breach situation: configuration #2

For configuration #2, the significant wave heights simulated at high tide reach 2.9 m at 500 m offshore the gravel barrier (Fig. 11a). Wave heights decrease to about 2.2 m as they propagate to the beach face due to wave energy dissipation on the reef platform. In the back-barrier area, simulated wave heights along the shoreline are <0.5 m from Le Québo in the west to Laneros in the east (Fig. 11b). The simulations show no significant increase in wave height in the back-barrier zone, leading to negligible wave setup (<0.02 m) (Fig. 11b).

One hour before high tide (HT-1 h), the simulated currents through the breach are oriented southwards (onshore) and reach a velocity of 1.8 m.s^{-1} (Fig. 12a). At high tide (HT) and at the beginning of the ebb tide (HT + 1 h), the currents are oriented offshore through the breach before flowing north-eastward along the spit at about 1 m.s^{-1} (Fig. 12b, c).

5.2.2. 300 m length breach enlargement: configuration #3

For configuration #3, the H_s and wave setup simulated at high tide on the back-barrier side reach 1 m and 0.08 m, respectively. The highest simulated H_s values in this area are located in front of the locality of Run Traou (Fig. 11b). Despite the enhanced wave height in the back-barrier area between configurations #2 and #3 due to the enlargement of the breach, simulated HT water levels are 5 cm lower in configuration #3 (Fig. 13a). In this case, the lower water level is linked to an increased draining of the sandflat area through a larger section of the breach. Similarly, the reduction in flood and ebb tide current velocities between configuration #3 and configuration #2 can be explained by the

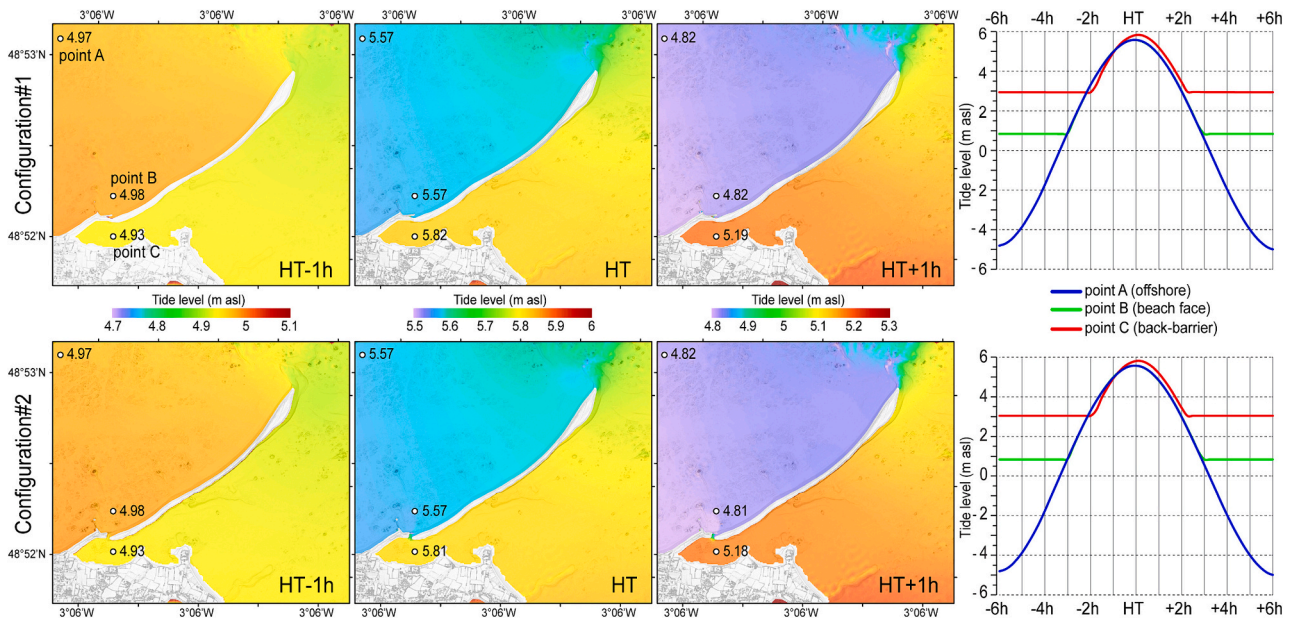


Fig. 9. Simulated spring-high water levels around the Sillon de Talbert at three different times of high tide for configuration#1 and configuration#2. Water levels values are given for the three points A, B and C (white dots) located offshore, and on both sides of the breach, respectively. Maps on the left, centre and right show simulated water levels 1 h before the high tide (HT-1 h), at high tide (HT) and 1 h after the high tide (HT + 1 h), respectively.

enlargement of the breach (Fig. 12).

5.2.3. 500 m long breach enlargement: configuration #4

The simulation for configuration #4 are quite similar to those for configuration #3. The significant wave height and wave setup along the back-barrier are <1 m and 0.1 m, respectively. The highest simulated H_s values are located along the inhabited coastline of Mer Melen (Fig. 11b). The current circulation pattern is also close to that observed in configuration #3. Simulated HT water levels in the back-barrier are 0.025 to 0.05 m lower than for configuration #2, also due to increased draining of the sandflat (Fig. 13b).

5.2.4. Crest lowering situation: configuration #5

Despite the complete overwash of the barrier, the simulated wave heights for configuration #5 do not exceed 0.8 m above the crest before decreasing on the back-barrier area, except in front of the Pen Vir promontory, where H_s values reach about 1 m (Fig. 11b). Wave setup never exceeds 0.1 m along the back-barrier area shoreline (Fig. 11a). Similarly to the results obtained for configurations #3 and #4, the simulated HT water levels are about 0.05 m lower than for configuration #2 (Fig. 13c).

The simulated currents show two main differences compared with configuration #2. Firstly, the HT currents are oriented onshore despite the difference in water levels on either side of the barrier (Fig. 12k). These currents are no longer linked to the tide, but to the predominance of waves overwashing the complete barrier. Secondly, the decrease of the flood and ebb current velocities is linked to a lower difference in water level on either side of the barrier when completely flooded.

6. Discussion

6.1. Uncertainties in the modelling approach

The model simulations were based on the extreme storm event of 1 February 2014, which is considered to be the most morphogenic event that has impacted the Sillon de Talbert over the last 20 years (Suanez et al., 2018a, 2022). The severe morphological impacts of this storm were also reported in other coastal zones of Brittany, where topomorphological monitoring has been carried out for several years, or

even decades (Blaise et al., 2015; Stéphan et al., 2018b, 2019; Suanez et al., 2022, 2023). The realistic hydrodynamic conditions for this event were numerically reproduced except for the tide level, which was increased in order to correspond to a 100-year return period water level. In this sense, the methodological approach adopted is in line with government recommendations, which state that the most extreme event should be taken into account when assessing the risk of coastal flooding (Perherin et al., 2012; Azzam et al., 2014). However, as indicated by Pirazzoli (2000) when analysing datasets from three tide gauges located on the west and north coasts of Brittany, “the highest sea surges [due to storm events] of the last decades did not occur at the time of spring high tide”. Therefore, this approach introduces a degree of uncertainty given by the fact that when we compare the wave characteristics at the peak of the storm at the time of high tide, i.e., February 1, 2014 at 7:00 pm, the simulations at the pressure sensor location indicate that H_{m0} and T_{moy} are ~2.7 m and ~10.9 s, for a centennial water depth of ~6.5 m. In comparison, in-situ recordings from the OSSI pressure sensor indicate a wave height and period of ~2.1 m and ~10.9 s, for a “real” water depth of ~5.8 m. The artificially increased water level at the model boundary contributes to explain these higher modeled H_{m0} values compared with in-situ measurements ($H_{m0-OSSI}$), but it still goes in the direction of a conservative modelling strategy regarding flooding risk.

Uncertainties in the modelling approach depend on a number of different factors including the model inputs, the accuracy of the model calibration, the boundary conditions, the bathymetric grid resolution, the forcing data, and the simulated physical processes. As indicated above, if the validation of the model simulations showed good agreement between the simulated and measured tide water levels with high correlations ($R^2 > 0.99$) and low errors (RMSE between 0.04 and 0.16 m), the errors between the simulated and measured tide currents were larger, with RMSE ranging from 0.07 to 0.25 $m.s^{-1}$ (see Fig. 7). The mentioned above, the slight phase shift is due to differences in temporal resolution between the two SHOM data sets and the Telemac-2D simulations. As it is often the case with hydrodynamic modelling, the accuracy of the bathymetric data, which affects the reliability of simulated physical processes such as currents or bottom friction, particularly in the shallow water zone, is also a determining factor (Jacob and Stanev, 2021; Alday et al., 2022; Umgieser et al., 2022).

The input wave conditions are obtained from WW3 simulations at

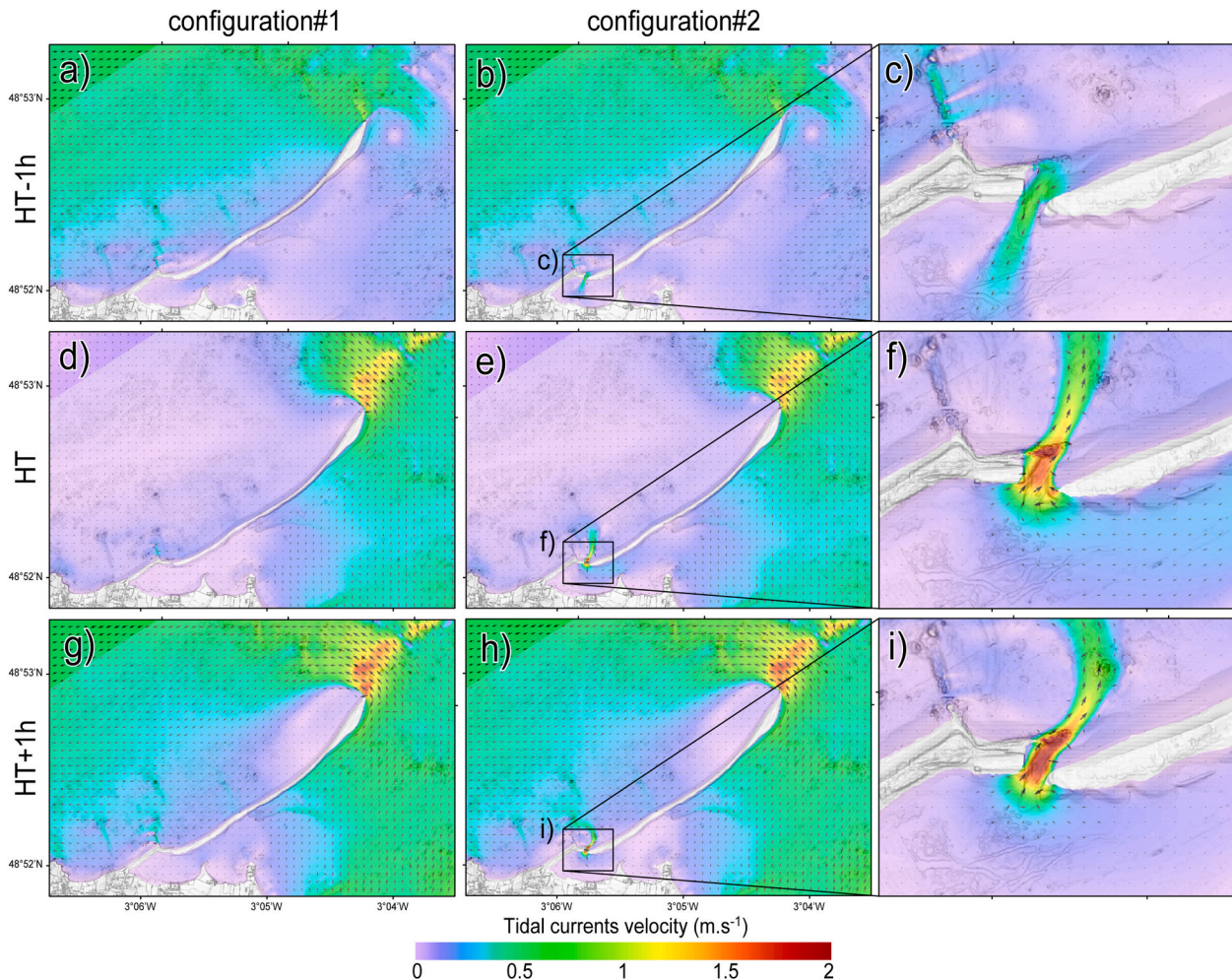


Fig. 10. Simulated tidal currents around the Sillon de Talbert at three different times of high tide for configuration#1 and configuration#2. (a), (b), and (c) show simulated tidal currents 1 h before the high tide (HT-1 h). (d), (e), and (f) represent simulated tidal currents at high tide (HT). (g), (h), and (i) show simulated tidal currents 1 h after the high tide (HT + 1 h).

grid points located at different water depths along the open boundary of the model (see Fig. 6a), without any knowledge of the errors between the in-situ wave height and the simulated wave height at these locations. However, the estimated RMSE and bias from Boudière et al. (2013) were 0.13 and 0.05 m, respectively, measured at the Pierres Noires wave buoy (situated off the west coast of Brittany) located at a depth of ~60 m. More recently, a study assessing the scales of spatial representativeness of the sea state parameters recorded by 11 buoys along the French Atlantic coastline (including a buoy located north of the study site) was carried out using retrospective simulations from the WW3 wave model hindcast (Mureau et al., 2022). The statistical errors (RMSE and bias) for wave height (H_s) computed between the model and in-situ data at each buoy location reach average of 0.25 m and 0.08 m respectively, up to 0.37 m and 0.27–0.33 m for both buoys located off the Brittany coast. The authors attribute this coastal sea state variability to several environmental factors, such as the presence of islands, shoals and rugged coastline, the amplified tidal currents and sea level variations over the shelf, and the intermediate to shallow water conditions together with the strong bathymetric gradients. The role of these environmental factors, in particular the complexity of the bathymetry of the platform, in altering the accuracy of numerical simulations is also highlighted by Dissanayake et al. (2021). As indicated by the authors, even if the unstructured grid allows to increase the spatial resolution from the offshore to the shallow zone, the bathymetric variations may not be always represented accurately.

Modelling uncertainties depend also on the topo-morphological configurations used in the different simulation scenarios that put into consideration the high mobility of the barrier of the Sillon de Talbert in time and space. As shown by Matias et al. (2012), based on wave flume experiments (Barrier Dynamics Experiment: BARDEX), the sensitivity of barriers to flooding depends essentially on wave conditions, sedimentological characteristics (including porosity, permeability and sediment size) and the morphological state of the barrier before the storm. Therefore, during a single overwash event, gravel barriers experiment successively crestral building, lowering and/or complete removal, which, through feedback, induce a change in hydrodynamic conditions (Matias et al., 2014). However, these studies are still highly experimental, and do not provide general statements on the hydro-morphosedimentary functioning that can be extrapolated to all barriers. In any case, these elements have not been taken into account in the modelling carried out as part of this study. In this paper, three configurations have considered a continuation of the erosive evolution trends measured in recent years, from the widening of the breach (configurations #3 and #4) to the complete levelling of the barrier (configuration #5). These topo-morphological configurations can have great uncertainties when considering the expected climate changes (including meteorological conditions) in the coming years. Hartley and Pontee (2008) distinguish two categories of uncertainties inherent in predicting future coastal evolution: (i) epistemic uncertainties, which relate to a lack of appropriate data or knowledge, and (ii) random uncertainties, which relate to

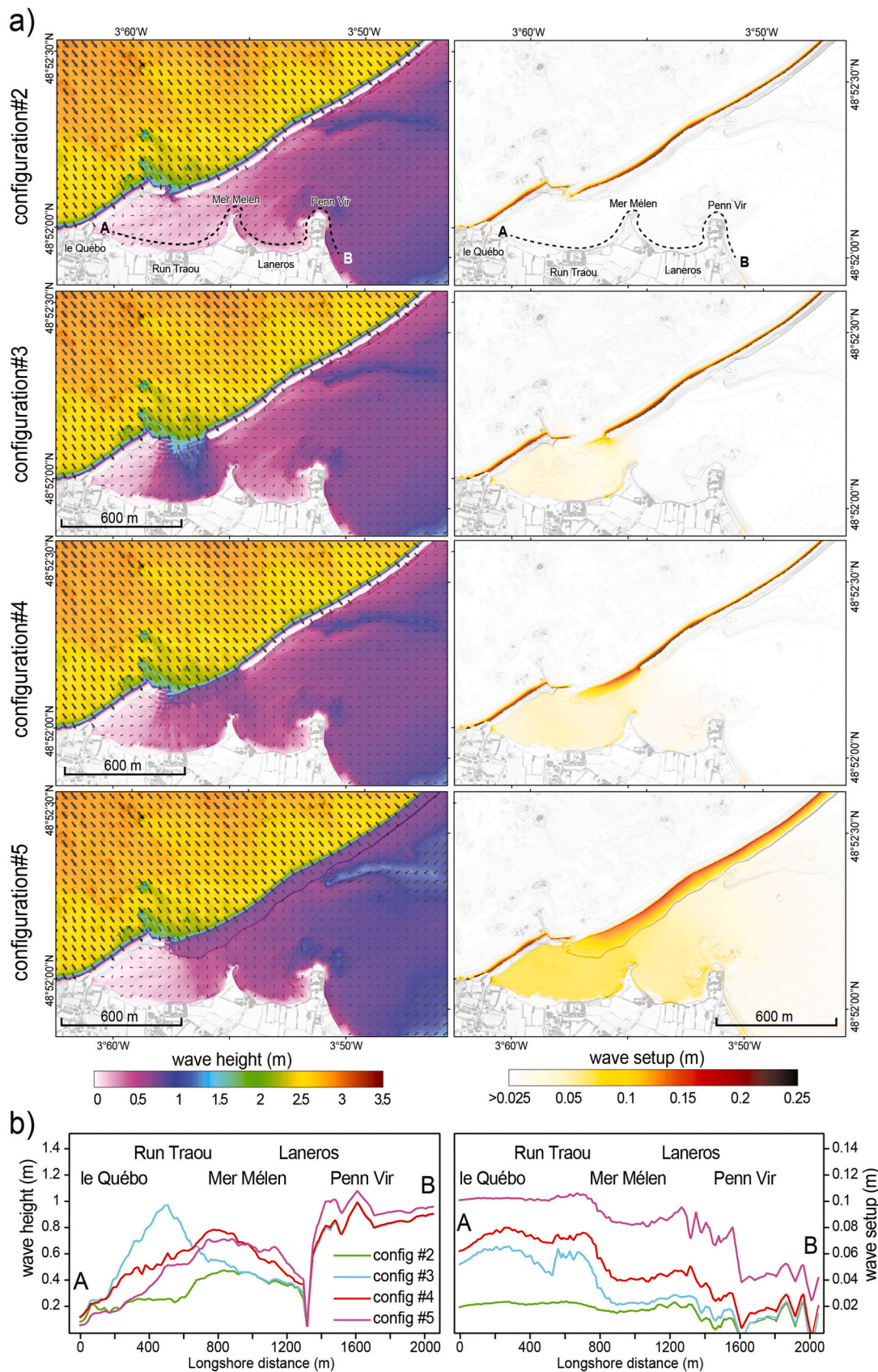


Fig. 11. Simulated significant wave height distribution and wave setup elevation at high tide for configurations #2 to #5 (a). Graphs in (b) represent the simulated wave height (left) and wave setup (right) extracted along a longshore transect located in the back-barrier area between points A and B. See (a) for the location of longshore transect.

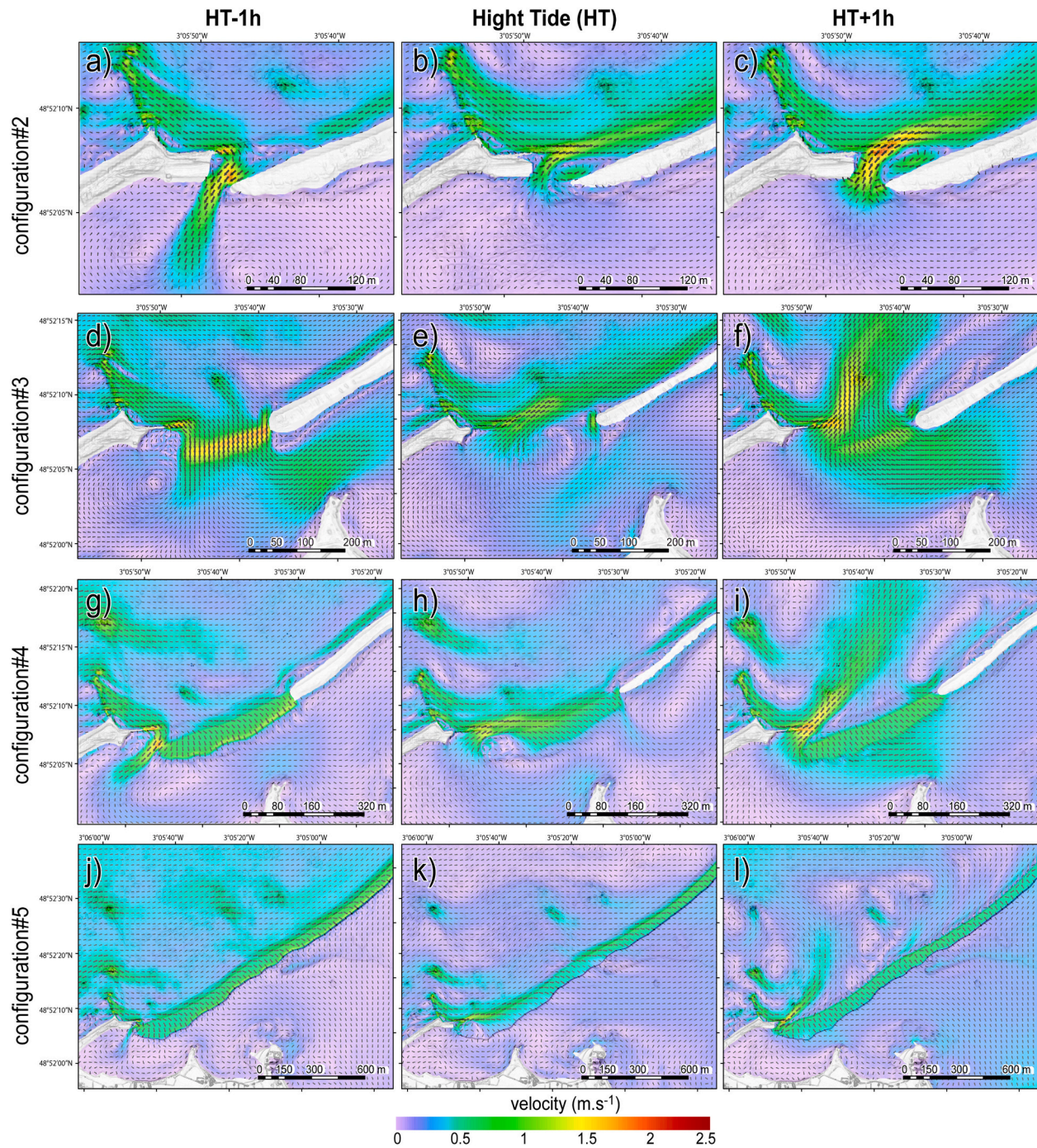


Fig. 12. Simulated currents at three different times of high tide for configuration#1 to #5. (a), (d), (g), and (i) show simulated currents 1 h before the high tide (HT-1 h). (b), (e), (h), and (k) represent simulated currents at high tide (HT). (c), (f), (i), and (l) show simulated currents 1 h after the high tide (HT + 1 h).

stochastic behaviour of coastal barriers leading to the formation and evolution of breaches. One of the greatest uncertainties associated with breaching processes is the rate of expansion of breaches once formed, which depends on the combination of forcing factors and existing beach states. Given this, the simulations presented in this paper should only be considered only as a tool for reflection and decision-making for coastal management in terms of flooding hazard.

Also, the use of a phase-averaged model in the present study did not allow us to investigate the potential effect of infragravity (IG) waves (Bertin et al., 2018) and swash dynamics at the back-barrier shoreline in the context of a breach enlargement. While the conservative approach employed in the present study (i.e., increasing by ~1 m the water level

at the open boundary for the extreme event simulations, leading to an offshore high tide level up to ~70 cm higher than the HAT level) should mostly compensate for the lack of IG waves in the model (in terms of their potential effect on high water levels reached in the back-barrier area at the IG time scale), applying a phase-resolving model to this very specific site, or at least a model accounting for the dynamics of IG waves (such as XBeach model in 'surf beat' mode), would surely be a relevant perspective for future work. In the meantime, it is worth noting that choosing the most extreme event in terms of wave forcing will not necessarily induce the highest flooding risk in all circumstances, as for instance shown by Bertin et al. (2014). That is partly why, in the present study, the selection of an extreme event is combined with the fact of

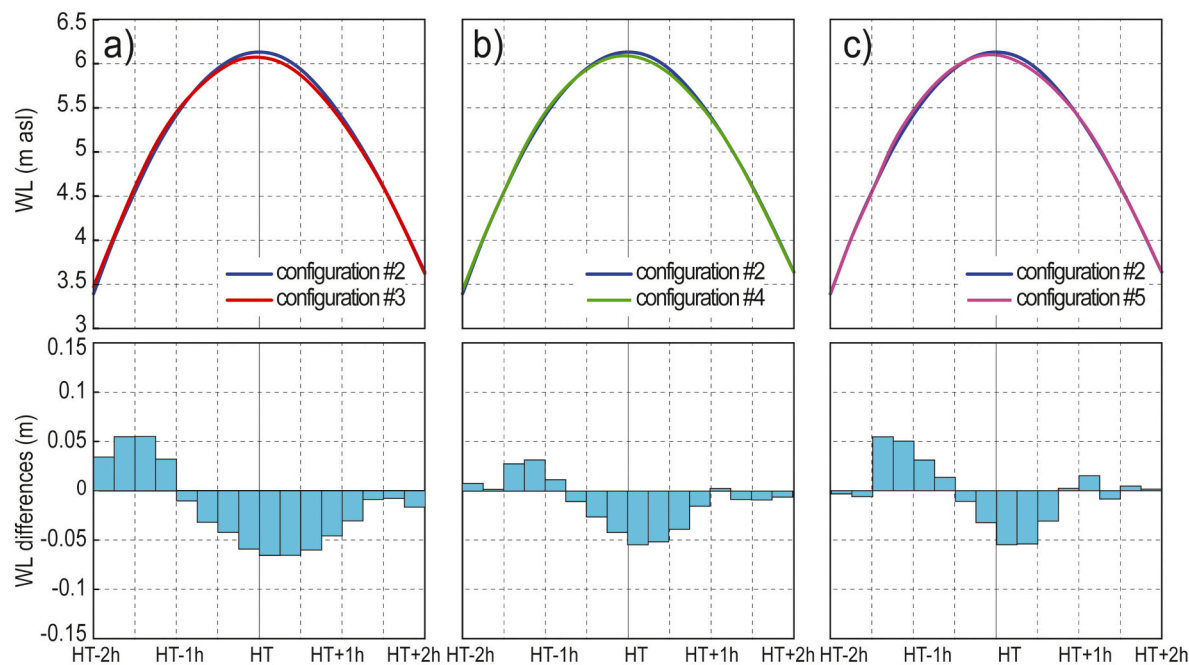


Fig. 13. Simulated water levels (WL) on the back of the Sillon de Talbert barrier for configurations #2 to #5 (see point C on Fig. 9 for location of the simulation point). Histograms represent water level differences between configurations #2 and #3 (a), #2 and #4 (b), #2 and #5 (c).

significantly increasing the water level at the open boundary to reach a conservative enough modelling strategy. It has been also shown that ‘extreme’ washover deposits can be mostly related to the presence of large IG waves but not necessarily to large storm surges (Baumann et al., 2017), which adds to the discussion about selecting an extreme event.

Finally, it should be pointed out that the methodological approach used in this study does not take into account the impact of climate change on future sea-level rise. As previously mentioned, the reference water level used in this study was indeed defined on the basis of an extreme tide water level for a 100-year return period + wave setup (centennial water level: CWL), in line with government recommendations for assessing the risk of submersion (Azzam et al., 2014). However, these recommendations indicate that the centennial water level should be raised by 0.2 m to take account of sea-level rise in 10 to 20 years’ time. The short-term hazard is therefore calculated as $RSL_{10-20\text{yrs}} = CWL + 0.2 \text{ m}$. Secondly, it is also recommended to take into account the future sea level rise for the year 2100, by raising the centennial level by 0.6 cm. The 100-year reference water level is thus calculated as follows = $RSL_{2100} = CWL + 0.6 \text{ m}$. The value of 0.6 m corresponds to the projections formulated by the IPCC in its 5th report of 2013, indicating, for the worst-case scenario, a rise in sea level of between 0.45 and 0.82 m, with an average value of 0.62 m (IPCC, 2013). Thus, using this approach for our study area, $RSL_{10-20\text{yrs}}$ equals 6.80 m asl and RSL_{2100} equals 7.2 m asl. As can be seen, these reference water levels are well above the extreme water levels simulated for the February 1, 2014 event, which do not exceed $6.38 \pm 0.14 \text{ m asl}$ on the back of the Sillon de Talbert barrier, particularly on the breach area. In any case, these reference water levels must now be reviewed, as the sixth IPCC report has revised the future rise in sea level upwards for the year 2100, giving an average value of around +1.30 m for the worst-case scenario RCE8.5 (Oppenheimer et al., 2019; IPCC, 2023).

6.2. Impact on flood hazards along the inhabited back-barrier shoreline

The model simulations clearly show that the Sillon de Talbert forms a physical boundary separating two water bodies (i.e. the ocean-side vs the back-barrier) characterized by specific tidal dynamics, with a time lag of about 15 min in the tidal peak and a difference of about 25 cm in

high tide level. The difference in tide water levels on either side of the barrier becomes more pronounced at the beginning of the ebb tide and can reach 30 cm during spring tides. This tidal characteristic is specific to the south-west coast of the English Channel, where the main semi-diurnal tidal component (M2) propagates from west to east with an increasing tidal range that is locally accentuated due to resonance phenomena (linked to the M4 tidal component) in response to the morphological configuration of the shoreface/foreshore zone (Pingree and Maddock, 1978). This specific phenomenon occurs in our study area, where a broad, gently sloping platform extends over a ~10 km offshore distance, from the shoreline to -10 m asl depth. Propagating eastwards, the tidal wave bypasses the tip of spit (including the reefs of the Olone archipelago), and progresses into the back-barrier zone where it is locally amplified due to the shallow water. Therefore, in the back-barrier sandflat, the tidal peak occurs 15 min later and the high tide water level is higher than on the ocean-side zone. As a result, ebb currents begin to flow before the high tide level is reached. The asymmetry between the ebb and flood currents is significant at the tip of the spit, where the high flow velocities have accumulated a large ebb gravel lobe in N-NW direction (Fig. 1c).

This tidal pattern is quite specific to the Sillon de Talbert, considering that for most of coastal barrier systems, back-barrier areas are affected by low amplitude tide-induced water level fluctuations due to limited hydrological connectivity between the ocean-side and the lagoon-side (Kraus and Wamsley, 2003; Kraus et al., 2008; Austin et al., 2013). However, barrier breaching enhances the water exchanges between the ocean-side and the back-barrier areas, which, in turn, may modify the hydrodynamics functioning of the tidal inlets. Velasquez Montoya et al. (2018) recently simulated the effects of sea-level rise, and subsequent tidal inlet morphodynamics, due to the surge of hurricane Sandy (October 29, 2012) on the lagoon-side at the Pea Island barrier-system (North Carolina) breaching. They showed that the rise of water level rise at the lagoon-side also increased the water level gradients between the ocean-side and the lagoon-side and strengthened the ebb currents in the tidal inlet.

The simulations carried out in the ante- and post-breaching configurations (configurations #1 and #2, respectively) indicate that the Sillon de Talbert breaching currently has no significant impact in terms of tide

water level condition changes (Fig. 9). However, in hypothetical configurations #3 to #5, the breach widening and/or the barrier crest lowering induces a decrease in the water level gradient on either side of the gravel barrier and reduces the high tide water levels (including wave setup) by a few centimeters (up to 5 cm) on the back-barrier zone. By draining part of the tidal prism, the breach acts as a communicating vessel, particularly in the back-barrier salt marsh where discharge currents directed offshore are simulated at high tide. The survey of morphological changes of the breach area undertaken from March 2018 also confirms the predominant role of ebb currents in the sediment transfers through the breach (Fig. 4). Most of the sediment eroded in the breach section was transferred northwards to the lower beach face of the spit, then remobilized by the waves. Therefore, while a flood delta has accumulated on the back-barrier salt marsh since the breach opening (see Section 3), it concerns a small volume of sediment when compared to the volume of ebb current sediment transfer.

The modelling indicates that widening the breach (i.e. configurations #3 and #4) tends to reduce the risk of coastal flooding in the low-lying areas of the Lanéros Peninsula by decreasing the water levels reached at high tide in the back-barrier area. Importantly, the lowering of high tide water level largely counterbalances the wave setup induced by wave propagation in the back-barrier zone through the breach. Thus, the total water level (i.e. tide + wave setup) simulated on the back-barrier for configurations #3 to #5 remains lower than (or almost equal to) the water level reached in the current topo-morphological configuration #2. These results therefore show that the breach has no significant effect on the coastal flooding hazards in the short term. It seems unlikely that this situation will change significantly in the next few years.

6.3. Impact on erosion hazards along the inhabited back-barrier shoreline

Hydrodynamic simulations showed that during extreme event conditions, the storm wave propagation (*i*) through the breach channel and/or (*ii*) overtop the inundated section of the barrier, is relatively limited despite breach widening or crest lowering considerations in future scenarios. For configurations #3 to #5, simulated wave heights reach a maximum height of ~1 m along a limited section of the back-barrier shoreline during the energy peak of storm event. This value decreases by 25 % to 50 % 1 h before and after high tide. Therefore, we can assume that barrier breaching should not lead to significantly more energetic hydrodynamic conditions and increased erosion hazards along the inhabited coastline in the coming years. The morphodynamic of this back-barrier zone is expected to be more controlled by local wind-generated waves, rather than energetic offshore storm waves, which remain occasional as indicated by Suanez et al. (2018a, 2022).

While the configuration #5, which considers a very low barrier profile, including a crest of 60 to 90 m wide and lowered to the MHST level, remains the worst case hypothetical scenario, it is based on the topo-morphological measurements taken after several intense morphogenic events inducing significant catastrophic overwash (Stéphan et al., 2010; Suanez et al., 2022). Therefore, this scenario might be representative of the future (decades to centuries) significant morphological changes of the Sillon de Talbert considering the long-term retreat of the spit over the last decades (Stéphan et al., 2012) and centuries (Pinot, 1994). This configuration allows us to assess whether the barrier still plays a significant role in storm wave attenuation for such a simulation. Simulations for configuration #5 show that even if the barrier crest is completely inundated at high tide, the barrier “body” still plays a major role in wave attenuation. However, the wave height at the crest, up to a maximum of 0.80 m, is still high, given that extreme water levels \geq of 0.45 m lead to sluicing-to-catastrophic overwash regimes responsible for significant landward displacements of the spit by rollover (Suanez et al., 2022). This element needs to be taken into account in the coastal management strategy, as the catastrophic flooding of single-ridge barriers (such as the Sillon de Talbert) is often a source of concern for local residents and/or elected representatives, particularly when the back-

barrier zones are urbanized. In such cases, managed realignment measures or nature-based soft management solutions can be vigorously challenged. As mentioned by Hudson and Baily (2018) in the case of Porlock beach in UK, monitoring of overwash events then appears as essential in understanding geomorphological evolution, but also to reassure the public and inform coastal managers in relation to the long-term stability of the barrier features.

6.4. A new strategy in terms of coastal risk management

As mentioned above, the refusal of the scientific council of the Sillon de Talbert nature reserve to artificially fill the breach through an engineering operation contrasts radically with the coastline management policies that have been implemented for decades on this site (Pinot, 1994; de Beaulieu, 2000; Stéphan et al., 2012).

In 1969, the management of the Sillon de Talbert, which was then a private domain of the State, was transferred to an inter-municipal syndicate to which the commune of Pleubian belonged (*syndicat mixte intercommunal pour la sauvegarde et la protection du sillon de Talbert*). From the early 1970s, the management strategy aimed to fix the shoreline in order to prevent the chronic retreat of the spit. Between 1974 and 1975, over 1,100 m of frontal rip-rap and a groin were installed on the proximal section, in the Chouck beach area (Fig. 3a). In 1982, the frontal rip-rap was extended to the median section, reaching 1,400 m, while some lowered sections of the spit were reprofiled using bulldozers until 1987 (de Beaulieu, 2000). In 1988, the local authorities even attempted to enclose the pebbles in fishing nets which were quickly destroyed by storms. For most cases, these expensive interventions (up to 1,000,000 euros in 1988, corresponding to ~2,000,000 euros in 2024) were carried out hastily, without any prior scientific study to support them.

Faced with these failures, the choice of a new nature-based management strategy was made by the Nature Reserve's newly created scientific council in the early 2000s (Houron, 2018). Most of the riprap was removed and scientific monitoring of the morphological evolution of the spit was undertaken (Stéphan et al., 2012). Thus, when the breach was opened in 2018, the choice of scientific expertise (such as that of the present study) was preferred to an engineering intervention.

The solution currently being considered for naturally filling the breach is to remove the last riprap (i.e. the Chouck groin and the two frontal riprap on either side) (see Fig. 3a). In this way, the retreat of the shoreline would deliver sediment to the longshore drift, which could naturally fill the breach (Stéphan et al., 2018a). However, this solution presupposes that the last private homes on the seafront are bought out and demolished by the *Conservatoire du Littoral*. At present, houses #3, #4 and #5 have been purchased (see Fig. 3a), and house #3 will be demolished by the end of 2024. Houses #1 and #2 have yet to be acquired by the *Conservatoire*, but they are still not for sale.

7. Conclusion

This modelling study has shown that the recent opening of the breach, which impacted the Sillon de Talbert spit barrier, has no significant or immediate consequences in terms of flooding risk in the low-lying urbanized area at the back-barrier. The results obtained for different topo-morphological configurations underline the fact that hydrodynamic changes in the area behind the barrier show no significant rise in maximal water levels, while the very flat topography of the salt marsh results in a significant decrease in wave energy conditions propagating through the breach (i.e. even for worst-case scenarios involving widening of the breach or severe erosion of the coastal barrier). This study, commissioned by local authorities and coastal managers, was instrumental in reassuring the local population living in the low-lying areas of the Laneros Peninsula. It also supports the new coastal management strategy adopted almost two decades ago by the Nature Reserve and the *Conservatoire du Littoral*. In western France, the

management of coastal erosion very often still leads to the use of hard defence structures, making the Sillon de Talbert spit one of the few coastal sites where a sustainable and adaptive management approach has been implemented. By removing the hard defence structures along the spit in 2002, coastal managers adopted an erosion management approach based on natural dynamics. However, in the coming decades (looking ahead to the 2100 s), this nature-based solution will need to be complemented by a more ambitious spatial planning strategy, particularly for built-up areas, to face future sea-level rise and mitigate the risk of marine flooding in low-lying areas at the back-barrier.

CRediT authorship contribution statement

Pierre Stéphan: Writing – original draft, Investigation, Funding acquisition, Formal analysis, Data curation. **Serge Suanez:** Writing – original draft, Supervision, Funding acquisition, Formal analysis, Data curation, Conceptualization. **Thomas Guérin:** Writing – original draft, Validation, Methodology, Data curation. **Aurélie Rivier:** Validation, Software, Formal analysis, Data curation. **Laurent Leballeur:** Validation, Software, Formal analysis, Data curation. **Benoit Waeles:** Supervision, Project administration, Methodology, Funding acquisition. **Jérôme Ammann:** Data curation. **Julien Houron:** Data curation.

Declaration of competing interest

The authors declare the following financial interests/personal relationships which may be considered as potential competing interests: Serge Suanez reports financial support was provided by the University of Brittany (UBO).

Data availability

Data will be made available on request.

Acknowledgements

The simulations were carried out using parallelized calculations on the HPC (High Performance Computing) supercomputer DATARMOR of the “*Pôle de Calcul et de Données pour la Mer – PCDM*” of IFREMER (<https://www.ifremer.fr/pcdm>). Monitoring of the Sillon de Talbert is carried out as part of the “*Service d’Observation National*” SNO-DYNALIT (<https://www.dynalit.fr/>), and is financially supported by the French “*Institut National des Sciences de l’Univers – INSU*”, the French coastal research infrastructure (IR-ILICO), and the French “*Ministère de l’Enseignement Supérieur, de la Recherche, et de l’Innovation*”. The surveys are also benefited from the Labex-Mer (ANR-10-LABX-0019) program between 2011 and 2018, and by the ISblue program, the Interdisciplinary graduate school for the blue planet (ANR-17-EURE-0015), since 2019. Both of these programs were co-funded by a grant from the French government under the program “*Investissements d’Avenir*” embedded in France 2030. This work was also supported by the Municipality of Pleubian and the Conservatoire du Littoral.

References

- Alday, M., Ardhuin, F., Dodet, G., Accensi, M., 2022. Accuracy of numerical wave model results: application to the Atlantic coasts of Europe. *Ocean Sci.* 18 (6), 1665–1689. <https://doi.org/10.5194/os-18-1665-2022>.
- Almeida, L.P., Masselink, G., Russell, P.E., Davidson, M.A., 2015. Observations of gravel beach dynamics during high energy wave conditions using a laser scanner. *Geomorphology* 228, 15–27. <https://doi.org/10.1016/j.geomorph.2014.08.019>.
- Ardhuin, F., Roland, A., Dumas, F., Bennis, A.-C., Sentchev, A., Forget, P., Wolf, J., Girard, F., Osuna, P., Benoit, M., 2012. Numerical wave modelling in conditions with strong currents: dissipation, refraction, and relative wind. *J. Phys. Oceanogr.* 42, 2101–2120. <https://doi.org/10.1175/JPO-D-11-0220.1>.
- Ata, R., 2018. TELEMAC-2D V8p0 user manual. <http://www.opentelemac.org/> (130 pp.).
- Austin, M.J., Masselink, G., McCall, R.T., Poate, T.G., 2013. Groundwater dynamics in coastal gravel barriers backed by freshwater lagoons and the potential for saline intrusion: two cases from the UK. *J. Mar. Syst.* 123–124, 19–32. <https://doi.org/10.1016/j.jmarsys.2013.04.004>.
- Azzam, C., Sabine Baillarguet, S., Bouet, A., Brodhag, E., Desire, Kavaj, A. Perherin C., Renaud, A. (Eds.), 2014. Guide méthodologique: Plan de prévention des risques littoraux. Ministère de l’Énergie, du Développement durable, et de l’Energie (MEDDE), Paris (169 pp.).
- Barnard, P., Hoover, D., Hubbard, D., Snyder, A., Ludka, B.C., Allan, J., Kaminsky, G.M., Ruggiero, P., Gallien, T.W., Gabel, L., McCandless, D., Weiner, H.M., Cohn, N., Anderson, D.L., Serafin, K.A., 2017. Extreme oceanographic forcing and coastal response due to the 2015–2016 El Niño. *Nat. Commun.* 8, 14365 <https://doi.org/10.1038/ncomms14365>.
- Baumann, J., Chaumillon, E., Bertin, X., Schneider, J.-L., Guillot, B., Schmutz, M., 2017. Importance of infragravity waves for the generation of washover deposits. *Mar. Geol.* 391, 20–35. <https://doi.org/10.1016/j.margeo.2017.07.013>.
- Bertin, X., Li, K., Roland, A., Zhang, Y.J., Breilh, J.F., Chaumillon, E., 2014. A modeling-based analysis of the flooding associated with Xynthia, central Bay of Biscay. *Coast. Eng.* 94, 80–89. <https://doi.org/10.1016/j.coastaleng.2014.08.013>.
- Bertin, X., de Bakker, A., van Dongeren, A., Coco, G., Andrée, G., Ardhuin, F., Bonneton, P., Bouchette, F., Castelle, B., Crawford, W., Davidson, M., Deen, M., Dodet, G., Guérin, T., Inch, K., Leckler, F., McCall, R., Muller, H., Olabarrieta, M., Roelvink, D., Ruessink, G., Sous, D., Stutzmann, E., Tissier, M., 2018. Infragravity waves: from driving mechanisms to impacts. *Earth Sci. Rev.* 177, 774–799. <https://doi.org/10.1016/j.earscirev.2018.01.002>.
- Billson, O., Russell, P., Davidson, M., 2019. Storm waves at the shoreline: when and where are infragravity waves important? *J. Mar. Sci. Eng.* 7 (5), 139. <https://doi.org/10.3390/jmse7050139>.
- Blaise, E., Suanez, S., Stephan, P., Fichaut, B., David, L., Cuq, V., Autret, R., Houron, J., Rouan, M., Floc'h, F., Ardhuin, F., Cancoüet, R., Davidson, R., Costa, S., Delacourt, C., 2015. Bilan des tempêtes de l’hiver 2013–2014 sur la dynamique de recul du trait de côte en Bretagne. *Géomorphol. Relief Process. Environ.* 21 (3), 267–294. <https://doi.org/10.4000/geomorphologie.11104>.
- Boersma, S.M., Hoenderkamp, K., 2003. Tregor, Final Report IFREMER (Amsterdam).
- Boudière, E., Maisondieu, C., Ardhuin, F., Accensi, M., Pineau-Guillou, L., Jérémie, L.J., 2013. A suitable metocean hindcast database for the design of marine energy converters. *Int. J. Mar. Energy* 3–4, e40–e52. <https://doi.org/10.1016/j.ijome.2013.11.010>.
- Breugem, W.A., 2020. Ongoing developments in TELEMAC and TOMAWAC at IMDC. In: Breugem, W.A., Frederickx, L., Koutrouveli, T., Chu, K., Kulkarni, R., Decrop, B. (Eds.), Online proceedings of the papers submitted to the 2020 TELEMAC-MASCARET User Conference, October 2020 (Antwerp). International Marine & Dredging Consultants (IMDC), pp. 115–121.
- Buscombe, D., Masselink, G., 2006. Concepts in gravel beach dynamics. *Earth Sci. Rev.* 70 (1–2), 33–52. <https://doi.org/10.1016/j.earscirev.2006.06.003>.
- Carrere, L., Lyard, F., Cancet, M., Guillot, A., Picot, N., 2016. FES 2014, a new tidal model - validation results and perspectives for improvements. In: Proceedings of the ESA Living Planet Symposium, (Prague, 9–13 May 2016), pp. 9–13.
- Carter, R.W.G., Orford, J.D., 1981. Overwash processes along a gravel beach. *Earth Surf. Process. Landf.* 6 (5), 413–426. <https://doi.org/10.1002/esp.3290060503>.
- Carter, R.W.G., Orford, J.D., 1984. Coarse clastic barrier beaches: a discussion of the distinctive dynamic and morphosedimentary characteristics. *Mar. Geol.* 60 (1–4), 377–389. [https://doi.org/10.1016/0025-3227\(84\)90158-0](https://doi.org/10.1016/0025-3227(84)90158-0).
- de Beaulieu, F., 2000. Le sillon de Talbert. In: Armen, vol. 112, pp. 2–9.
- Dissanayake, P., Yates, M.L., Suanez, S., Floch, F., Krämer, K., 2021. Climate change impacts on coastal wave dynamics at Vogot Beach, France. *J. Mar. Sci. Eng.* 9 (9), 1009. <https://doi.org/10.3390/jmse9091009>.
- Dornbusch, U., 2017. Design requirement for mixed sand and gravel beach defences under scenarios of sea level rise. *Coast. Eng.* 124, 12–24. <https://doi.org/10.1016/j.coastaleng.2017.03.006>.
- Durand, P., Anselme, B., Thomas, Y.-F., 2010. L’impact de l’ouverture de la brèche dans la langue de Barbarie à Saint-Louis du Sénégal en 2003: un changement de nature de l’aléa inondation? *Cybergeo* 496. <https://doi.org/10.4000/cybergeo.23017>.
- Elsayed, S.M., Oumeraci, H., 2016. Combined modelling of coastal barrier breaching and induced flood propagation using XBeach. *Hydrology* 3 (4), 32. <https://doi.org/10.3390/hydrology3040032>.
- Elsayed, S.M., Oumeraci, H., 2018. Modelling and mitigation of storm-induced saltwater intrusion: Improvement of the resilience of coastal aquifers against marine floods by subsurface drainage. *Environ. Model Softw.* 100, 252–277. <https://doi.org/10.1016/j.envsoft.2017.11.030>.
- Forbes, D.L., Orford, J.D., Carter, R.W.G., Shaw, J., Jennings, S.C., 1995. Morphodynamic evolution, selforganisation, and instability of coarse-clastic barriers on paraglacial coast. *Mar. Geol.* 126 (1–4), 63–85. [https://doi.org/10.1016/0025-3227\(95\)00066-8](https://doi.org/10.1016/0025-3227(95)00066-8).
- Fouquet, T., 2018. TOMAWAC V8p0r3 User Manual. In: TELEMAC-MASCARET System Software 2018.
- Galland, J.C., Goutal, N., Hervouet, J.M., 1991. TELEMAC: a new numerical model for solving shallow water equations. *Adv. Water Resour.* 14 (3), 138–148. [https://doi.org/10.1016/0309-1708\(91\)90006-A](https://doi.org/10.1016/0309-1708(91)90006-A).
- Giloy, N., Latapy, A., André, G., 2023. Estimation of skew surge uncertainties when predicting tides in the past. *Weather Clim. Extrem.* 41, 100597 <https://doi.org/10.1016/j.wace.2023.100597>.
- Hartley, L., Pontee, N., 2008. Assessing breaching risk in coastal gravel barriers. *Proc. Inst. Civ. Eng.–Marit. Eng.* 161 (4), 143–152. <https://doi.org/10.1680/mena.2008.161.4.143>.
- Houron, J., 2018. Le sillon de Talbert (Pleubian, Côtes d’Armor): Réserve Naturelle Régionale. In: Bulletin de la Société Géologique et Minéralogique de Bretagne, vol. 16 (série d), pp. 55–63.

- Hudson, C., Baily, B., 2018. Delivering sustainable coasts: monitoring the long-term stability of a breached barrier beach, Porlock Bay, Somerset, United Kingdom. *Ocean Coast. Manag.* 152, 88–99. <https://doi.org/10.1016/j.ocecoaman.2017.11.022>.
- IPCC, 2013. Climate change 2013: the physical science basis. In: Stocker, T.F., Qin, D., Plattner, G.-K., Tignor, M., Allen, S.K., Boschung, J., Nauels, A., Xia, Y., Bex, V., Midgley, P.M. (Eds.), Contribution of Working Group I to the Fifth Assessment Report of the Intergovernmental Panel on Climate Change. Cambridge University Press, Cambridge, United Kingdom and New York, NY, USA (1535 pp.).
- IPCC, 2023. Climate change 2023: synthesis report. In: Core Writing Team, Lee, H., Romero, J. (Eds.), Contribution of Working Groups I, II and III to the Sixth Assessment Report of the Intergovernmental Panel on Climate Change. IPCC, Geneva, Switzerland, pp. 35–115. <https://doi.org/10.59327/IPCC/AR6-989291691647>.
- Jacob, B., Staney, E.V., 2021. Understanding the impact of bathymetric changes in the German Bight on coastal hydrodynamics: one step toward realistic morphodynamic modeling. *Front. Mar. Sci.* 8, 640214. <https://doi.org/10.3389/fmars.2021.640214>.
- Jennings, R., Shulmeister, J., 2002. A field based classification scheme for gravel beaches. *Mar. Geol.* 186 (3–4), 211–228. [https://doi.org/10.1016/S0025-3227\(02\)00314-6](https://doi.org/10.1016/S0025-3227(02)00314-6).
- Kraus, N.C., Wamsley, T.V., 2003. Coastal barrier breaching, part 1: overview of breaching processes. In: Coastal and Hydraulics Engineering Technical Note ERDC/CHL CHETN-IV-56. US Army Corps of Engineers, Engineer Research and Development Center, Coastal and Hydraulics Laboratory, Vicksburg, MS, 14 pp. <https://erdc-library.erdc.dren.mil/jspui/bitstream/11681/1964/1/CHETN-IV-56.pdf>.
- Kraus, N.C., Militello, A., Todoroff, G., 2002. Barrier breaching processes and barrier spit breach, Stone Lagoon, California. *Shore Beach* 70 (4), 21–28.
- Kraus, N.C., Patsch, K., Munger, S., 2008. Barrier beach breaching from the lagoon side, with reference to Northern California. *Shore Beach* 76 (2), 33–43.
- Lazare, P., Dumas, F., 2008. An external–internal mode coupling for a 3D hydrodynamical model for applications at regional scale (MARS). *Adv. Water Resour.* 31 (2), 233–250. <https://doi.org/10.1016/j.advwatres.2007.06.010>.
- Leatherman, S.P., 1979a. Migration of Assateague Island, Maryland, by inlet and overwash processes. *Geology* 7 (2), 104–107. [https://doi.org/10.1130/0091-7613\(1979\)7<104:MOAIMB>2.0.CO;2](https://doi.org/10.1130/0091-7613(1979)7<104:MOAIMB>2.0.CO;2).
- Leatherman, S.P. (Ed.), 1979b. *Barrier Islands From the Gulf of St. Lawrence to the Gulf of Mexico*. Academic Press, New York (325 pp.).
- Li, X., Leonardi, N., Plater, A.J., 2020. Impact of barrier breaching on wetland ecosystems under the influence of storm surge, sea-level rise and freshwater discharge. *Water* 40, 771–785. <https://doi.org/10.1007/s13157-019-01219-x>.
- Matias, A., Williams, J.J., Masselink, G., Ferreira, Ó., 2012. Overwash threshold for gravel barriers. *Coast. Eng.* 63, 48–61. <https://doi.org/10.1016/j.coastaleng.2011.12.006>.
- Matias, A., Blenkinsopp, C.E., Masselink, G., 2014. Detailed investigation of overwash on a gravel barrier. *Mar. Geol.* 350, 27–38. <https://doi.org/10.1016/j.margeo.2014.01.009>.
- Mureau, G., Dodet, G., Suanez, S., 2022. Characterizing sea state variability along the French Atlantic coast. In: Levacher, D., Benoit, M., Sanchez, M., Teles, M. (Eds.), *Actes du colloque des XVIIème Journées Nationales Génie Civil – Génie Côtier*, Chatou, 11–13 Octobre 2022, pp. 129–142. <https://doi.org/10.5150/jngc.2022.015>.
- Nienhuis, J.H., Heijkers, L.G.H., Ruessink, G., 2021. Barrier breaching versus overwash deposition: predicting the morphologic impact of storms on coastal barriers. *J. Geophys. Res. Earth* 126 (6), e2021JF006066. <https://doi.org/10.1029/2021JF006066>.
- Oppenheimer, M., Glavovic, B.C., Hinkel, J., van de Wal, R., Magnan, A.K., Abd-Elgawad, A., Cai, R., Cifuentes-Jara, M., DeConto, R.M., Ghosh, T., Hay, J., Isla, F., Marzeion, B., Meyssignac, B., Sebesvari, Z., 2019. Sea level rise and implications for low-lying islands, coasts and communities. In: Pörtner, H.-O., Roberts, D.C., Masson-Delmotte, V., Zhou, P., Tignor, M., Poloczanska, E., Mintenbeck, K., Alegría, A., Nicolai, M., Okem, A., Petzold, J., Rama, B., Weyer, N.M. (Eds.), *IPCC Special Report on the Ocean and Cryosphere in a Changing Climate*. Cambridge University Press, Cambridge, UK and New York, NY, USA, pp. 321–445. <https://doi.org/10.1017/9781009157964.006>.
- Orford, J.D., Anthony, E.J., 2011. Extreme events and the morphodynamics of gravel-dominated coastal barriers: strengthening uncertain ground. *Mar. Geol.* 290 (1–4), 41–45. <https://doi.org/10.1016/j.margeo.2011.10.005>.
- Orford, J.D., Carter, R.W.G., 1982. Crestal overtop and washover sedimentation on a fringing sandy gravel barrier coast, Carnsore Point, Southeast Ireland. *J. Sediment. Res.* 52 (1), 265–278. <https://doi.org/10.1306/212F72C-2B24-11D7-8648000102C1865D>.
- Orford, J.D., Carter, R.W.G., 1995. Examination of mesoscale forcing of a swash-aligned, gravel barrier from Nova Scotia. *Mar. Geol.* 126 (1–4), 201–211. [https://doi.org/10.1016/0025-3227\(95\)00078-D](https://doi.org/10.1016/0025-3227(95)00078-D).
- Orford, J.D., Carter, R.W.G., Forbes, D.L., 1991. Gravel barrier migration and sea level rise: some observations from Story Head, Nova Scotia, Canada. *J. Coast. Res.* 7 (2), 477–488. <https://www.jstor.org/stable/4297854>.
- Orford, J.D., Carter, R.W.G., Jennings, S.C., Hinton, A.C., 1995. Processes and timescales by which a coastal gravel-dominated barrier responds geomorphologically to sea-level rise: story head barrier, Nova Scotia. *Earth Surf. Process. Landf.* 20 (1), 21–37. <https://doi.org/10.1002/esp.3290200104>.
- Orford, J.D., Carter, R.W.G., Jennings, S.C., 1996. Control domains and morphological phases in gravel-dominated coastal barriers of Nova Scotia. *J. Coast. Res.* 12 (3), 51–85. <https://www.jstor.org/stable/4298507>.
- Orford, J.D., Forbes, D.L., Jennings, S.C., 2002. Organisational controls, typologies and time scales of paraglacial gravel-dominated coastal systems. *Geomorphology* 48 (1–3), 51–85. [https://doi.org/10.1016/S0169-555X\(02\)00175-7](https://doi.org/10.1016/S0169-555X(02)00175-7).
- Perherin, C., Azzam, C., Kergadallan, X., 2012. Révision du guide méthodologique plans de prévention des risques littoraux: une meilleure prise en compte de l'ensemble des phénomènes pour la connaissance de l'aléa submersion marine (SHF, Paris, 1–2 février 2012), Actes des 34èmes journées de l'hydraulique. https://www.persee.fr/doc/jhydr_0000-0001_2012_act_34_1_1239.
- Pingree, R.D., Maddock, L., 1978. The M4 tide in the English Channel derived from a non-linear numerical model of the M2 tide. *Deep-Sea Res.* 25 (1), 53–63. [https://doi.org/10.1016/S0146-6291\(21\)00006-0](https://doi.org/10.1016/S0146-6291(21)00006-0).
- Pinot, J.-P., 1994. Fixer le plan ou gérer le profil : l'exemple du Sillon du Talberg. *Cahiers Nantais* 41–42, 307–316. <https://doi.org/10.3406/canan.1994.1609>.
- Pirazzoli, P.A., 2000. Surges, atmospheric pressure and wind change and flooding probability on the Atlantic coast of France. *Oceanol. Acta* 23 (6), 643–661. [https://doi.org/10.1016/S0399-1784\(00\)00122-5](https://doi.org/10.1016/S0399-1784(00)00122-5).
- Plant, N.G., Stockdon, H.F., 2012. Probabilistic prediction of barrier-island response to hurricanes. *J. Geophys. Res. Earth* 117, F03015. <https://doi.org/10.1029/2011JF002326>.
- Plant, N.G., Stockdon, H.F., Sallenger, A.H., Turco, M.J., East, J.W., Taylor, A.A., Shaffer, W.A., 2010. Forecasting hurricane impact on coastal topography. *Eos. Trans. AGU* 91 (7), 65–66. <https://doi.org/10.1029/2010EO070001>.
- Plomaritis, T.A., Ferreira, O., Costas, S., 2018. Regional assessment of storm related overwash and breaching hazards on coastal barriers. *Coast. Eng.* 134, 124–133. <https://doi.org/10.1016/j.coastaleng.2017.09.003>.
- Poate, T., Masselink, G., McCall, R., Russell, P., Davidson, M., Turner, I.L., 2013. High frequency in-situ field measurements of gravel beach response during storm conditions. *Mar. Geol.* 342, 1–13. <https://doi.org/10.1016/j.margeo.2013.05.009>.
- Pollard, J.A., Christie, E.K., Brooks, S.M., Spencer, T., 2021. Impact of management regime and regime change on gravel barrier response to a major storm surge. *J. Mar. Sci. Eng.* 9 (2), 147. <https://doi.org/10.3390/jmse9020147>.
- Pye, K., Blott, S.J., 2009. Progressive breakdown of a gravel-dominated coastal barrier, Dunwich-Walberswick, Suffolk, U.K.: processes and implications. *J. Coast. Res.* 25 (3), 589–602. <https://www.jstor.org/stable/27698354>.
- Roland, A., Ardhuin, F., 2014. On the developments of spectral wave models: numerics and parameterizations for the coastal ocean. *Ocean Dyn.* 64 (6), 833–846. <https://doi.org/10.1007/s10236-014-0711-z>.
- Saha, S., Moorthi, S., Pan, H.-L., Wu, X., Wang, J., Nadiga, S., Tripp, P., Kistler, R., Woollen, J., Behringer, D., Liu, H., Stokes, D., Grumbine, R., Gayno, G., Wang, J., Hou, Y.T., Chuang, H.Y., Juang, H.M.H., Sela, J., Iredell, M., Treadon, R., Kleist, D., van Delst, P., Keyser, D., Derber, J., Ek, M., Meng, J., Wei, H., Yang, R., Lord, S., van den Dool, H., Kumar, A., Wang, W., Long, C., Chelliah, M., Xue, Y., Huang, B., Schemm, J.K., Ebisuzaki, W., Lin, R., Xie, P., Chen, M., Zhou, S., Higgins, W., Zou, C., Liu, Q., Chen, Y., Han, Y., Cucurull, L., Reynolds, R.W., Rutledge, G., Goldberg, M., 2010. The NCEP Climate Forecast System reanalysis. *Bull. Am. Meteorol. Soc.* 91 (8), 1015–1057. <https://doi.org/10.1175/2010BAMS3001.1>.
- Schoonees, J.S., Lenhoff, L., Raw, A.J., 1998. Preventing natural breaching of the major sand spit protecting the port of Walvis Bay. *Coast. Eng. Proc.* 1 (26), 1475–1488. <https://doi.org/10.1061/9780784404119.109>.
- SHOM, 2005. Courants de marée des côtes de France (Manche/Atlantique). Produit numérique. <https://diffusion.shom.fr/marees/courants-de-maree/courants-2d.html>.
- SHOM, 2008. LITTO3D®. https://services.data.shom.fr/geonetwork/srv/api/records/BATHYMETRIE_L3D.xml.
- SHOM, 2016. Références altimétriques maritimes – Ports de France métropolitaine et d’outre-mer. Côtes du zéro hydrographique et niveaux caractéristiques de la marée. Service Hydrographique et Océanographique de la Marine, Brest.
- SHOM/CETMEF, 2012. Statistiques des niveaux marins extrêmes des côtes de France (Manche et Atlantique) (ISBN 978-2-11-128331-2).
- Stéphan, P., Suanez, S., Fichaut, B., 2010. Franchissement et recul des cordons de galets par rollover. Impact de la tempête du 10 mars 2008 dans l'évolution récente du Sillon de Talbert (Côtes d'Armor, Bretagne). *Norois* 215, 59–75 doi:10.400/norois.3252.
- Stéphan, P., Suanez, S., Fichaut, B., 2012. Long-term morphodynamic evolution of the Sillon de Talbert gravel barrier (Brittany, France). *Shore Beach* 80 (1), 19–36.
- Stéphan, P., Suanez, S., Fichaut, B., Autret, R., Blaise, E., Houron, J., Ammann, J., Grandjean, P., 2018a. Monitoring the medium-term retreat of a gravel spit barrier and management strategies, Sillon de Talbert (North Brittany, France). *Ocean Coast. Manag.* 158, 64–82. <https://doi.org/10.1016/j.ocecoaman.2018.03.030>.
- Stéphan, P., Suanez, S., Houron, J., Ammann, J., Fichaut, B., 2018b. Suivi pluri-décennal de la flèche de galets du Sillon de Talbert (Pleubian, Côtes d'Armor) à partir de modèles numériques de terrain (MNT). INDIGEO. <https://doi.org/10.35110/8e37c01f4cec-4edb-8c01-7047725f7dc4>.
- Stéphan, P., Blaise, E., Suanez, S., Fichaut, B., Autret, R., Floc'h, F., Cuq, V., Le Danec, N., Ammann, J., David, L., Jaud, M., Delacourt, C., 2019. Long to medium to short-term shoreline dynamics of the Brittany coast (Western France). *J. Coast. Res.* 88 (SI), 89–109. <https://doi.org/10.2112/SI88-008.1>.
- Stéphan, P., Suanez, S., Ammann, J., Houron, J., 2023. Données de suivi topomorphologique de la brèche du Sillon de Talbert (Pleubian, Bretagne nord) par photogrammétrie (SfM). INDIGEO. <https://doi.org/10.35110/e77c22c-840a-48c2-be03-ad1d3167679b>.
- Stockdon, H.F., Sallenger, A.H., Holman, R.A., Howd, P.A., 2007. A simple model for the spatially-variable coastal response to hurricanes. *Mar. Geol.* 238 (1–4), 1–20. <https://doi.org/10.1016/j.margeo.2006.11.004>.
- Stockdon, H.F., Doran, K.J., Thompson, D.M., Sopkin, K.L., Plant, N.G., Sallenger, A.H., 2012. National Assessment of Hurricane-induced Coastal Erosion Hazards: Gulf of

- Mexico, U.S. Geological Survey Open-File Report 2012-1084. <https://doi.org/10.3133/ofr20121084>.
- Stockdon, H.F., Doran, K.J., Thompson, D.M., Sopkin, K.L., Plant, N.G., 2013. National Assessment of Hurricane-induced Coastal Erosion Hazards: Southeast Atlantic Coast, U.S. Geological Survey Open-File Report 2013-1130. <https://pubs.usgs.gov/of/2013/1130/pdf/ofr2013-1130.pdf>.
- Suarez, S., Stéphan, P., Floc'h, F., Autret, R., Fichaut, B., Blaise, E., Houron, J., Ammann, J., Grandjean, P., Accensi, M., André, G., Arduin, F., 2018a. Fifteen years of hydrodynamic forcing and morphological changes leading to breaching of a gravel spit, Sillon de Talbert (Brittany). *Géomorphol. Relief Process. Environ.* 24 (4), 403–428. <https://doi.org/10.4000/geomorphologie.12677>.
- Suarez, S., Stéphan, P., Floc'h, F., 2018b. Mesures des conditions hydrodynamiques côtierres le long du Sillon de Talbert (Ploubian, Bretagne nord). INDIGEO. [10.35110/f6f2440a-4703-4352-8f3e-3f3999472b3c](https://doi.org/10.35110/f6f2440a-4703-4352-8f3e-3f3999472b3c).
- Suarez, S., Stéphan, P., Fichaut, B., Ammann, J., Accensi, M., 2020. Medium-term longshore and cross-shore dynamics of a gravel spit driving by storm events (Sillon de Talbert, Brittany, France). *J. Coast. Res.* 95 (SI), 669–673. <https://doi.org/10.2112/SI95-130.1>.
- Suarez, S., Stéphan, P., Autret, R., Houron, J., Floc'h, F., David, L., Ammann, J., Accensi, M., André, G., Le Guyader, D., Cancouët, R., 2022. Catastrophic overwash and rapid retreat of the gravel spit barrier during storm events (Sillon de Talbert, North Brittany, France). *Earth Surf. Process. Landf.* 47 (8), 2014–2043. <https://doi.org/10.1002/esp.5361>.
- Suarez, S., Yates, M.L., Floc'h, F., Accensi, M., 2023. Using 17 years of beach/dune profile monitoring to characterize morphological dynamics related to significant extreme water level events in North Brittany (France). *Geomorphology* 433, 108709. <https://doi.org/10.1016/j.geomorph.2023.108709>.
- Tolman, H.L., the WAVEWATCH III® Development Group, 2014. User Manual and System Documentation of WAVEWATCH III® version 4.18. Technical Note 316. NOAA/NWS/NCEP/MMAB.
- Ungiesser, G., Ferrarin, C., Bajo, M., Bellafiore, D., Cucco, A., De Pascalis, F., Ghezzo, M., McKiver, W., Arpaia, L., 2022. Hydrodynamic modelling in marginal and coastal seas - the case of the Adriatic Sea as a permanent laboratory for numerical approach. *Ocean Model* 179, 102123. <https://doi.org/10.1016/j.ocemod.2022.102123>.
- van der Westhuysen, A.J., van Dongeren, A.R., Groeneweg, J., van Vledder, G.P., Peters, H., Gautier, C., van Nieuwkoop, J.C.C., 2012. Improvements in spectral wave modeling in tidal inlet seas. *J. Geophys. Res.* 117, C00J28 <https://doi.org/10.1029/2011JC007837>.
- Velasquez Montoya, L., Sciaudone, E.J., Mitasova, H., Overton, M.F., 2018. Observation and modeling of the evolution of an ephemeral storm-induced inlet: Pea Island Breach, North Carolina, USA. *Cont. Shelf Res.* 156, 55–69. <https://doi.org/10.1016/j.csr.2018.02.002>.
- Villas Boas, A.B., Cornuelle, B.D., Mazloff, M.R., Gille, S.T., Arduin, F., 2020. Wave-current interactions at meso- and submesoscales: insights from idealized numerical simulations. *J. Phys. Oceanogr.* 50, 3483–3500. <https://doi.org/10.1175/JPO-D-20-0151.1>.
- Wamsley, V., Kraus, N.C., 2005. Coastal barrier island breaching, part 2: mechanical breaching and breach closure. In: *Coastal and Hydraulics Engineering Technical Note ERDC/CHL CHETN-IV-65*. U.S. Army Corps of Engineers Washington, DC 20314-1000, 21 pp. <https://apps.dtic.mil/sti/pdfs/ADA438882.pdf>.